ENHANCEMENT OF NUCLEATE BOILING HEAT TRANSFER BY SURFACE MODIFICATION IN A COLD PLATE EVAPORATOR

BY

GREGORY JOHN ALEXANDER

THESIS

Submitted in partial fulfillment of the requirements
for the degree of Master of Science in Mechanical Engineering
in the Graduate College of the
University of Illinois at Urbana-Champaign, 2015

Urbana, Illinois

Adviser:

Professor Predrag Hrnjak

ABSTRACT

Electronics cooling applications have very high local heat fluxes, which allow for significant improvement of heat transfer by different methods. This thesis focuses on improving boiling heat transfer by surface modification with R134a in a microchannel cold plate evaporator. Internal copper and brass surfaces were modified with the deposition of copper oxide nanostructures with the intention of improving nucleate boiling heat transfer. The spike-like nanostructures increase the real internal surface area and thus allow for more efficient bubble nucleation. Heat transfer coefficients were calculated with both baseline and modified cold plates for varied heat and mass flux loadings to compare how effective the nanostructures are at improving heat transfer. Longevity of the coating in a working environment and any loss of effectiveness over time were explored. To better understand the differences caused by this surface modification, flow visualization was also considered.

ACKNOWLEDGEMENTS

I would like to first and foremost thank my research adviser, Professor Pega Hrnjak, whose constant diligence and guidance has kept me focused and dedicated to my work, especially when being stuck on particularly frustrating issues. Without his constant reminders of thinking about the bigger picture, I would have more often than not gotten lost in the insignificant details. Whenever the going got tough, his words kept me going.

I would also like to thank Roger Palmer, Andrew Lehman, Abhijit Sathe, and all other representatives at Parker Hannifin who have helped to make this project a success through funding and support. As the first student to conduct research in the new cooperative Parker/ACRC laboratory on campus, it has been an honor to work with all representatives of Parker on a project that not only focuses on a specific need of the company but also one that fundamentally furthers the research goals of the ACRC group. I hope that this collaboration is only more successful in the years to come with future projects.

Thanks also go out to the rest of the members of the ACRC research group for all of their guidance and companionship. Whether it is through lessons with EES and VEE, invitations to play soccer, or tips on how to keep leaks under control, these individuals have made even the latest of nights in the second and third floors of the Mechanical Engineering Laboratory a memorable experience.

Many thanks also go out to Cliff Gulyash and the rest of the MechSE machine shop for their help in constructing supporting parts and modifying existing cold plates to help make this project a success.

Specifically I would also like to thank Professor Nenad Mijkovic for all of his help with developing the copper oxide surface structures for my application. While I used the surface structures to enhance evaporation instead of condensation, his guidance greatly accelerated my search for a proper modification.

Lastly, I would like to thank my closest friends and family for all of their support over the last two years: my roommates, Alex Halaska, Tim Garbaciak, and Alek Heilstedt, for their unquestioning support despite my sometimes questionable study habits; my cousin, Dan Heinzel, for the solid wall to bounce ideas off of (and for the thrill of the race to see who will graduate first!); and my parents, Herb and Laurel Alexander, for their unconditional love and care for me as I pursued my Master's degree.

TABLE OF CONTENTS

LIST OF SYMBOLS

a	Signal Height/Amplitude
A	Internal Surface Area
A_c	Microchannel Cross-sectional Area
AIF	Alicona Infinite Focus
COP	Coefficient of Performance
C_P	specific heat
CuO	Copper Oxide
EDM	Electric Discharge Machining
g_{CP}	mass flux
h	Generic Heat Transfer Coefficient
h_{local}	Local Heat Transfer Coefficient
$h_{overall}$	Overall Heat Transfer Coefficient
$h_{overall,base}$	Baseline Heat Transfer Coefficient Curve Fit
$h_{overall,mod}$	Modified Heat Transfer Coefficient Curve Fit
$h_{overall,P}$	Overall Heat Transfer Coefficient by Pressure
$h_{overall,T}$	Overall Heat Transfer Coefficient by Temperature
h_1	Subcooled Enthalpy
h_2	Inlet Enthalpy
h_3	Outlet Enthalpy
L	Centerline Length
$\dot{m}$	Mass Flow Rate
P_{cal}	Calibration Pressure

P_{FLUKE}	FLUKE Measurement Pressure
P_{sat}	Saturation Pressure
P_1	Subcooled Pressure
P_2	Inlet Pressure
P_3	Outlet Pressure
Q	Heater Power
Q_{CP}	Cold Plate Power
q_{CP}	Cold Plate Heat Flux
$Q_{CP,adj}$	Adjusted Cold Plate Power
$Q_{CP,losses}$	Cold Plate Heat Losses
Q_{PH}	Preheater Power
$Q_{PH,adj}$	Adjusted Preheater Power
$Q_{PH,losses}$	Preheater Heat Losses
R	Electrical Resistance
R_a	Centerline Average Roughness
R_q	Centerline Root-mean-square Roughness
SEM	Scanning Electron Microscopy
SiO_4	Silane
T_{amb}	Ambient Temperature
T_{cal}	Calibration Temperature
$T_{CP,avg}$	Average Cold Plate Wall Temperature
$T_{CP1\rightarrow 5}$	Cold Plate Wall Temperatures
T_{HAT}	High Accuracy Thermometer Temperature
T_{in}	Inlet Temperature
T_{incp}	External Cold Plate Temperature

T_{inph}	External Preheater Temperature
T_{out}	Outlet Temperature
T_{sat}	Saturation Temperature
$T_{sat,2}$	Saturation Temperature by P_2
$T_{sat,avg}$	Average Saturation Temperature
T_{sub}	Subcooled Temperature
T_{win}	Inlet Water Temperature
T_{wout}	Outlet Water Temperature
UA_{CP}	Cold Plate Heat Loss Coefficient
UA_{PH}	Preheater Heat Loss Coefficient
V	Voltage
X_{avg}	Average Cold Plate Quality
X_2	Inlet Quality
X_3	Outlet Quality
z	Surface Height Function
Δh	Enthalpy Difference Across the Cold Plate
ΔT	Temperature Difference
$\Delta T_{TC,cal}$	Recalibrated Temperature Difference
ΔP	Cold Plate Pressure Drop
ΔX	Quality Difference
σ_A	Internal Surface Area Error
$\sigma_{hoverall}$	Overall Heat Transfer Coefficient Error
σ_i	Individual Component Error
$\sigma_{\dot{m}}$	Mass Flow Rate Error
σ_P	Pressure Transducer Error

$\sigma_{QPH,adj}$	Adjusted Preheater Power Error
$\sigma_{QCP,adj}$	Adjusted Cold Plate Power Error
$\sigma_{Tsat,avg}$	Average Saturation Temperature Error
σ_{TC}	Thermocouple Error
σ_{Z}	Arbitrary Function Error

CHAPTER 1: INTRODUCTION

1.1: Motivation

In typical electronics cooling applications, heat loads are quite dense, yielding very high and local heat fluxes at the microchip locations. This has led to the use of metal heat sinks with high thermal conductivity in order to spread out this local heat load and absorb it into a fluid for heat removal, whether that fluid is air, water, or a refrigerant. For most purposes, a heat transfer coefficient is a useful measure to determine how well heat is dispersed from one body to another, defined by the following equation:

$$h = \frac{Q}{A\,\Delta T} \tag{1.1}$$

Here h is the heat transfer coefficient [W/m^2K], Q [W] is a given heat load, A [m^2] is the surface area over which the heat is transferred, and ΔT [K] is the temperature difference between the two bodies. If h is relatively constant, one of the easiest ways to better dissipate an increasing heat load would be to simply increase the surface area over which heat is transferred accordingly. However, this solution can often be too bulky to realistically implement, as evaporators and condensers would have to increase in size dramatically, making the electronics units themselves larger. One could simply absorb the higher heat load by letting the temperature difference increase, but this can lead to dangerously high temperatures that can lead to chip failure. Therefore, the ideal way to deal with an increasing heat load would be to increase h without changing the area or temperature difference.

To increase h in this way, one has to look to the physical basis of heat transfer to see what can be changed. It is widely known that introducing a boiling fluid as the method of heat removal greatly increases h since the latent heat of vaporization of the fluid allows for large heat loads with much smaller temperature differences than single phase applications. However, improving the boiling heat transfer coefficient for a given application requires more ingenuity. Fundamentally, boiling from a liquid to a gas within a closed loop system occurs by two processes: nucleate and convective boiling. In nucleate boiling—occurring when the fluid is predominantly liquid—vapor bubbles form on a surface as heat is added through that surface. Here heat transfer is greatly increased as the rising bubbles constantly refresh the surface with turbulent liquid, since the primary mode of heat transfer is at the solid-liquid interface. In convective flow boiling, a large enough temperature difference causes a thin vapor film to form on the solid surface which consistently sheds vapor bubbles into the fluid flow. Here, the primary mode of heat transfer is at a solid-vapor interface, and thus the heat transfer coefficient is less compared to nucleate boiling due to the less desirable thermal properties of the vapor over the liquid.

1.2: Objectives

To increase the boiling heat transfer coefficient, one must try to improve either the solid-liquid interface of nucleate boiling or the solid-vapor interface of convective boiling. Since it already has a naturally higher heat transfer coefficient, it makes

more sense to look into how to improve h for nucleate boiling, as the solid-liquid interface shows more potential for improvement.

One way to increase heat transfer in nucleate boiling is to increase the number of nucleation sites. More sites allow for more bubble formation which in turn allows for more phase change to occur, a higher critical heat flux and greater overall heat transfer. Logistically, the best way to do this is to increase the surface's roughness. This increases the true area of the surface which increases the number of nucleation sites. In this thesis, a copper oxide surface modification—one which is predominantly used on copper surfaces—will be explored with further applications on brass. The effect of this surface modification on the heat transfer across a cold plate evaporator with boiling R134a will be studied. With the surface modification's spike-like structures, it is theorized that the increased nano-roughness of the internal surface of the cold plate will allow for a greater overall heat transfer coefficient due to more nucleation sites and greater heat transfer at the solid-liquid interface.

1.3: Thesis Structure and Summary

This thesis is structured with two main sections which exist as chapters 2 and 3. It begins with an exploration of using copper oxide surface structures on brass surfaces (Chapter 2); this chapter focuses on the motivation behind choosing this

specific surface modification and how it behaves when applied to not only copper but also brass surfaces. Chapter 3—the main focus of this thesis—applies this surface modification to a cold plate evaporator and discusses the differences seen in both heat transfer coefficient and pressure drop. Finally, Chapter 4 serves as a final conclusion to tie together the objectives of the main sections and summarize the results found therein.

CHAPTER 2: MODIFYING COPPER AND BRASS WITH COPPER OXIDE SURFACE STRUCTURES

2.1: Motivation

In order to effectively transfer heat away from transistor electronics, metal heat sinks must be designed with careful attention to their application. In some cases, one must deal with increasing heat loads without changing the surface area of the heat sink due to size or cost limitations of the heat sink. Roughening or changing the surface structure of the internal area of the heat sink effectively increases the heat transfer by increasing the effective area without increasing the bulk geometry. This change can also significantly increase the pressure drop due to an increased roughness factor. Therefore, one should seek to increase heat transfer with increased surface roughness in such a way that the improvements seen outweigh the cost of any increase pressure drop. In this chapter, a specific surface modification of copper surfaces consisting of a thin layer of copper oxide (CuO) is explored for further applications with brass. If the surface modification is effectively constructed on a brass surface, then the scope of its application can be widened.

2.2: Choosing a Surface Modification

A number of surface modifications were considered. Whether it is by surface etching, sand blasting, or a chemical process, the surface should be changed in a

way that changes the roughness to increase the number of nucleation sites by increased area. Copper oxide nanostructures were chosen as a highly attractive and novel way to changes the surface structure. Previous work by N. Miljkovic et al. describes that these CuO surfaces—as seen in Figure 2.1a—are very simple to create and, when silanized, demonstrate a 30% increase in the condensation heat transfer coefficient compared to other hydrophobic surfaces [1]. In their experiments, a hydrophobic surface was desired for condensation, so that when water droplets condensed on the surface they would coalesce and bounce away at smaller sizes. With faster coalescence and droplet removal, the solid-gas interface—where condensing heat transfer is greater—dominates the solid-liquid interface between a droplet and the surface due to the more hydrophobic surface.

In these condensation experiments, the copper oxide structures were made to be hydrophobic by silanizing the surface—a process using SiO_4, silane, to produce a hydrophobic silicone-enriched coating over top of the nanostructures [1]. Inherently, the copper oxide nanostructures are actually hydrophilic. The spike-like structures seen in Figure 2.1a make for a very wettable surface as surface tension draws liquid into the cavities among the spikes. This makes the surface desirable for boiling applications, where the heat transfer is highest at a liquid-solid interface where bubble nucleation occurs.

2.3: Building Copper Oxide Nanostructures

As previously stated, these copper oxide surface structures are quite simple to produce. N. Dou outlines the manufacturing process to create the copper oxide structures [2]. In essence, a well-mixed solution of deionized water, sodium chlorite, sodium hydroxide, and trisodium phosphate dodecahydrate is first heated up to near boiling. Then, cleaned copper samples are inserted into the bath for approximately five minutes, after which the surface structures have been formed. This chemical bath forms the structures by a two-step oxidation process. The copper surface oxidizes to form a very thin layer (<200 nm) of less stable Cu_2O, which then reoxidizes into CuO in a way which grows the spike-like structures [2]. After this, the surface structures are fully formed, with scales going from ~400 nm to 1,000 nm in height [2]. Please refer to Appendix A for a more detailed process of structure formation.

2.4: Surface Visualization and Validation

Figure 2.1b shows the reproduced surface structures on thin ½" by ½" samples as shown at the same magnification of Figure 2.1a. As compared to Figure 2.1a, Figure 2.1b shows that the synthesis process described by Dou was successfully replicated for the copper sample. Note that visually the two images look slightly different shades due to different settings being used when focusing SEM images.

It was theorized that the chemical oxidation process may not be effective on a brass surface; due to the presence of Zinc in the brass—a metal with a higher oxidation potential than copper—the oxidation of copper into the nanostructures may have been inhibited to the point that effective structures are not formed. To test the chemical oxidation process on brass, similar thin ½" by ½" samples of 363 brass were produced. One sample of each metal was left untreated for a baseline surface to visualize, while another sample of each metal was modified with the copper oxide structures. All four samples—copper and brass, baseline and modified—were cleaned and imaged under an SEM to further inspect the formation of the surface structures.

Figures 2.2 and 2.3 show SEM images of the copper and brass samples—further images with different magnifications can be found in Appendix A. The CuO nanostructures grew quite well on the copper samples. While it is difficult to see at the 5,000x magnification, at 30,000x magnification one can clearly see the spike-like structures that have covered the surface of the copper.

Figure 2.3 promises that the synthesis process for the copper oxide nanostructures on 363 brass is still effective at creating nano-roughness. The structures are noticeably smaller for the brass sample than the copper sample, yet they are still of the same order of magnitude in size. This size difference could be due to the presence of zinc in the brass sample. However, the only known chemical reaction to

take place is between the chemical bath and the copper to form CuO [2]. While some of the zinc has likely oxidized, the smaller structures on the brass sample in Figure 2.3 as compared to the structures in Figure 2.2 can most likely be attributed to there simply being less copper to react with.

2.5: Surface Roughness

Surface roughness can be defined through a number of different parameters. Two of the more common roughness measurements are centerline average roughness, R_a, and centerline root-mean-square roughness, R_q, which are defined by the following two equations [3].

$$R_a = \frac{1}{L}\int_0^L |z|\, dx \tag{2.1}$$

$$R_q = \sqrt{\frac{1}{L}\int_0^L z^2\, dx} \tag{2.2}$$

Here L is the total length of the centerline studied and z is the height function of the surface along the centerline defined from 0 to L. R_a is the average of the absolute value of the surface height while R_q takes the root-mean-square of this average. Both surface roughness measurements are in units of length, typically in micrometers for most surfaces. For many applications, R_q is superior to R_a because it accounts for sensitivity to high peaks and valleys [3].

To illustrate this, Figure 2.4 shows two theoretical surfaces that have the same value for R_a but different values for R_q [4]. The surface on the right has a lower R_q value because it has plateaus instead of tall peaks above the average surface height, even though both the peaks and the plateaus contribute equivalently to R_a. So between two surfaces, the surface with a smaller R_q value will have in general a smoother surface with less variation in the surface height.

To quantify changes in roughness, the ½" by ½" samples of baseline and modified brass and copper were observed using an Alicona Infinite Focus (AIF) machine [5]. AIF is an optical technique for computational surface reconstruction that can be used to determine a number of surface parameters, including surface roughness. It takes still images of a surface with each image having its own fixed focal length. Each successive image has the focal length raised incrementally by raising the z axis—in steps as small as 20 nm—perpendicular to the surface. A computer then determines which sections of each image are in focus and which are not; those sections that are in focus directly correspond to the parts of the surface that exist at the depth as determined by the focal length. When all images are then stitched together, a three-dimensional representation surface is reconstructed.

Figure 2.5 shows the reconstructed three-dimensional surface maps of all samples studied using AIF, where each map was taken from a different 50x50 μm^2 area of the sample surface. Table 2.1 gives the corresponding surface roughness—R_a and

R_q—for all samples for these maps. All eight surface roughness measurements are considerably low; since only a 50x50 μm^2 section was mapped for each sample, larger scale features are few and far between and are practically unseen in many of the maps from Figure 2.5. For instance, only one small corner of the copper surface with CuO structures in Figure 2.5 has larger scale roughness features, while the rest of the map appears relatively flat. Future tests should expand the test to multiple 50x50 μm^2 sections to further enhance the resolution of the roughness results to have a more even distribution of larger scale roughness features.

Interestingly, as per Table 2.1, all surface roughness measurements slightly decrease with the addition of the CuO surface structures for both copper and brass samples despite the small sample area. If a larger sample area were taken, large scale features—those an order of magnitude larger than the 200-500 nm size surface structures that tend to dominate surface roughness measurements—would prevail and we would see lesser and lesser differences between the baseline and modified surfaces as the sample area is increased.

The small differences seen in R_a and R_q when the CuO surface structures are added is counterintuitive to the observations of the structures as seen in Figures 2.2 and 2.3. It is clear from these images that the surfaces become more visually rough with the addition of the oxide layer. One explanation for this discrepancy is that the surface structures add nano-roughness to the surface without altering the R_a and R_q

measurements globally. Figures 2.6 and 2.7 shows an example of two theoretical surfaces with very close R_a and R_q values as calculated by equations (2.1) and (2.2); the equations to represent the surface heights are described below.

$$z_1(x) = a \left|\sin(\tfrac{2\pi x}{L})\right| \tag{2.3}$$

$$z_1(x) = a\,|\sin(2\pi x/L)| + \tfrac{a}{100}\sin(\tfrac{200\pi x}{L}) \tag{2.4}$$

Equation (2.3) represents a simple sine wave normalized to a centerline average length L and peak height/amplitude of a. Equation (2.4) represents a very similar sine wave with a slight perturbation of noise with amplitude two orders of magnitude smaller than the original signal and frequency two orders of magnitude larger. This noise is representative of the nano-roughness that is added by the CuO surface structures in comparison to a surface's bulk roughness. These two surfaces have equivalent R_a and R_q values as computed by MATLAB software, despite the slight noise added. By this simple simulation, R_a and R_q prove to be insufficient at fully capturing all changes in surface roughness, since some changes are too small to be effectively captured. Therefore, the addition of copper oxide surface structures may add enough nano-roughness to significantly increase the true surface area of a surface without significantly changing bulk roughness measurements.

2.6: Conclusion

The fabrication of copper oxide surface structures was validated to be effective on pure copper surfaces; CuO structures were also successfully grown on brass samples

to comparable sizes. Through the use of AIF, surface roughness measurements were taken of each sample, where it was found that the addition of CuO structures does not significantly increase the R_a or R_q roughness but does increase the nanoscale roughness that is not captured by these two roughness parameters.

2.7: Figures and Tables

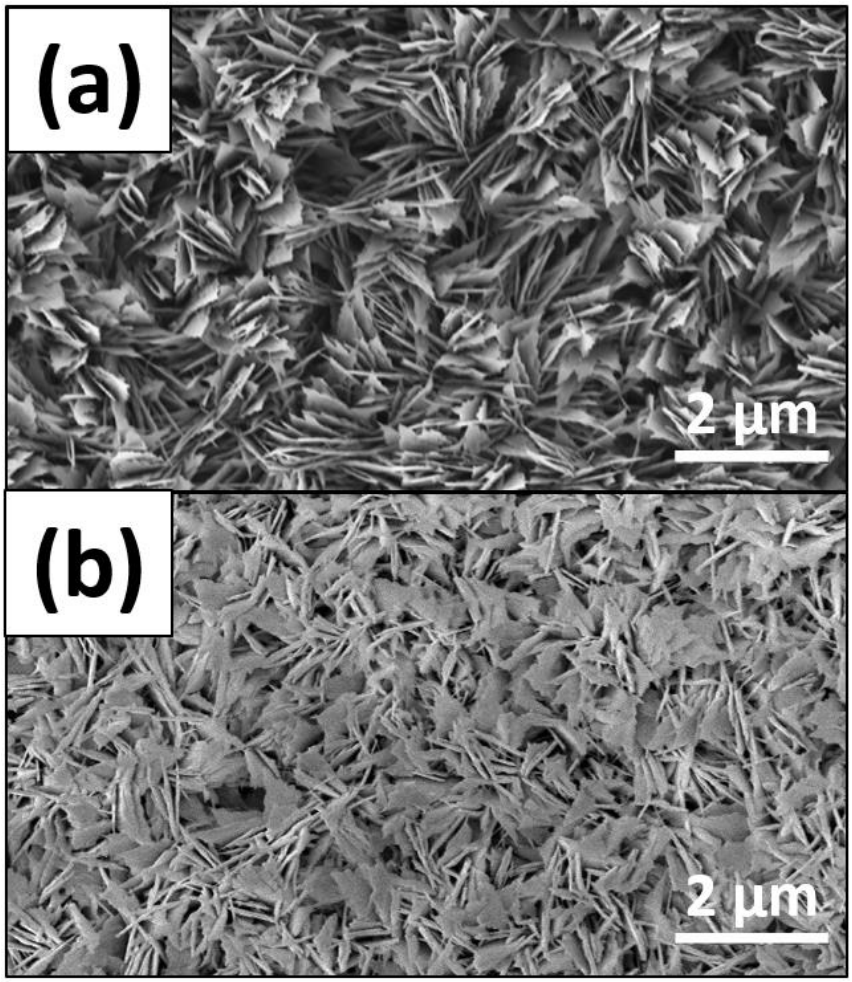

Figure 2.1: (a) Sample SEM image of CuO nanostructures on a copper substrate before being silanized [1] and (b) a copper sample reproduced by same methods.

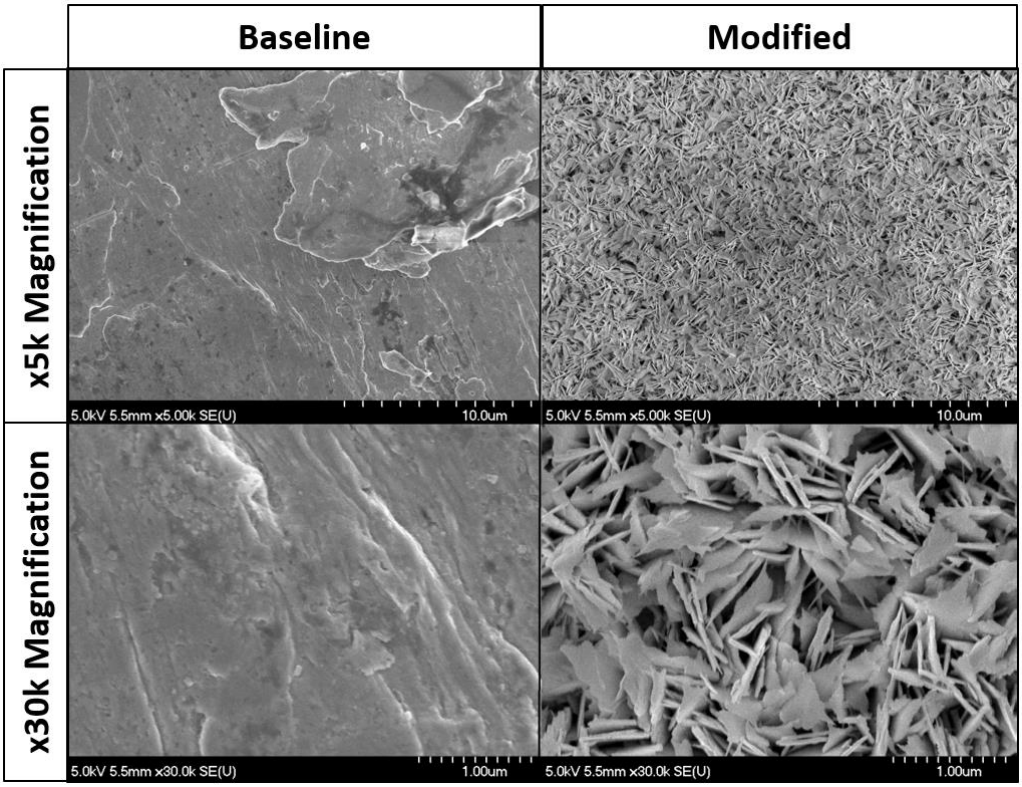

Figure 2.2: Copper sample visualized with SEM.

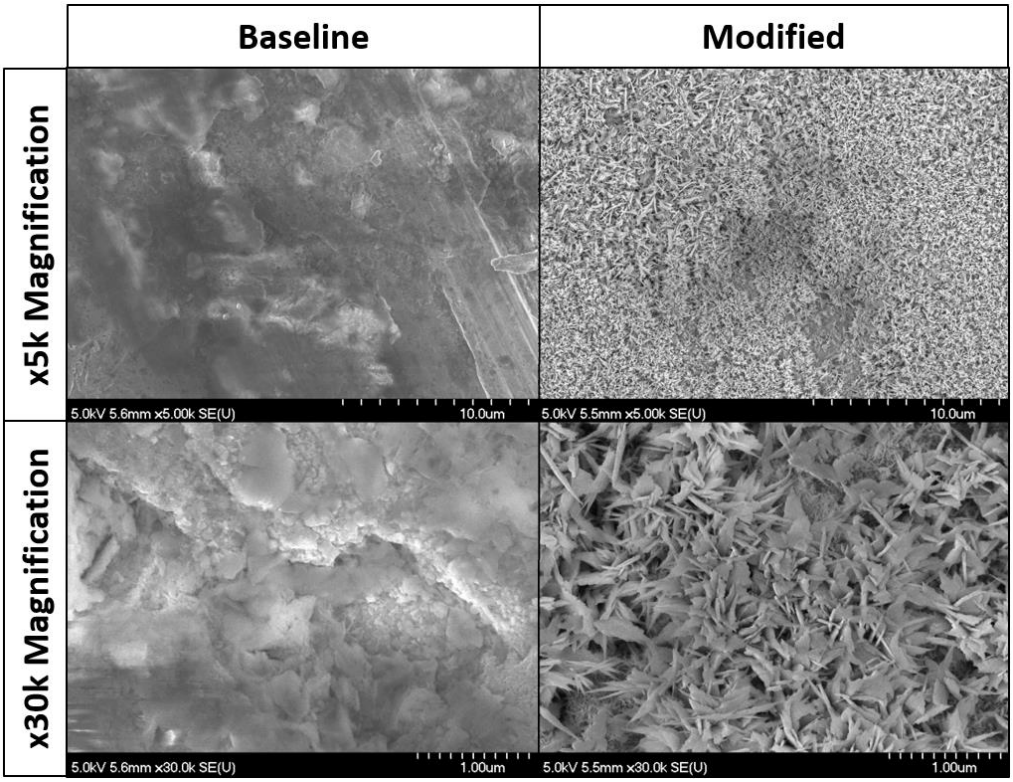

Figure 2.3: 363 Brass sample visualized with SEM.

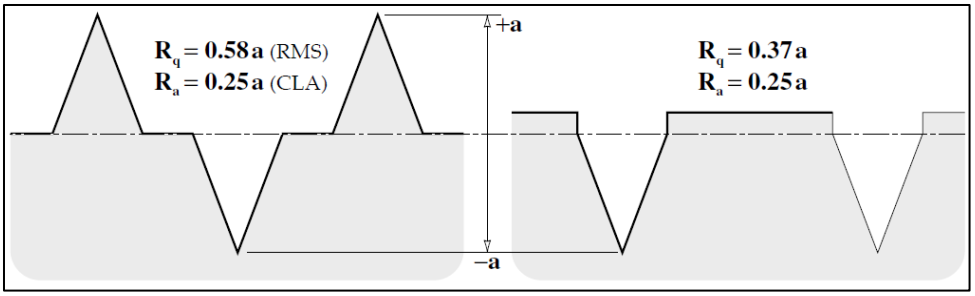

Figure 2.4: Two theoretical surfaces with equal R_a values and different R_q values [4].

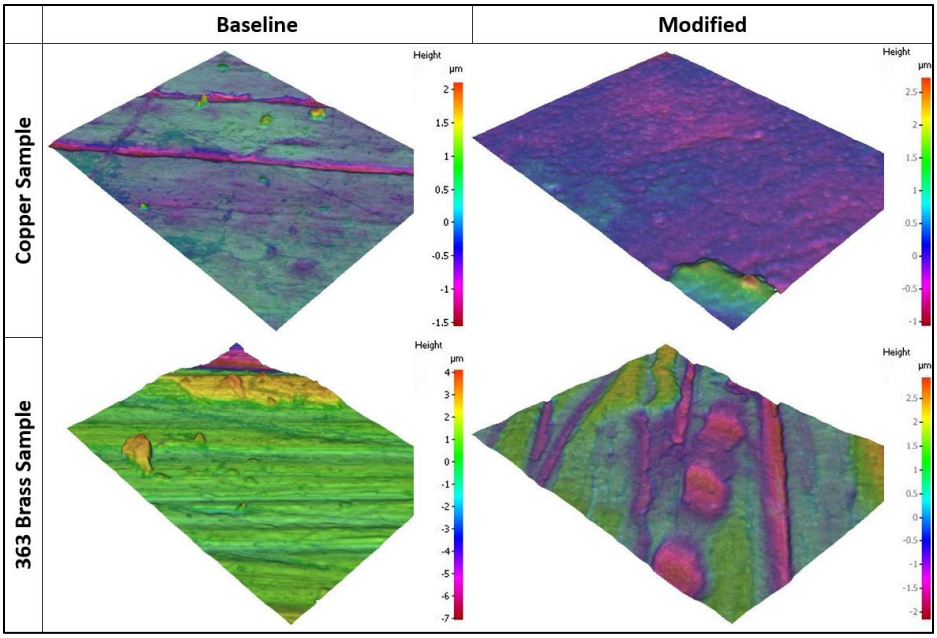

Figure 2.5: AIF sample surface reconstruction for surface roughness measurements.

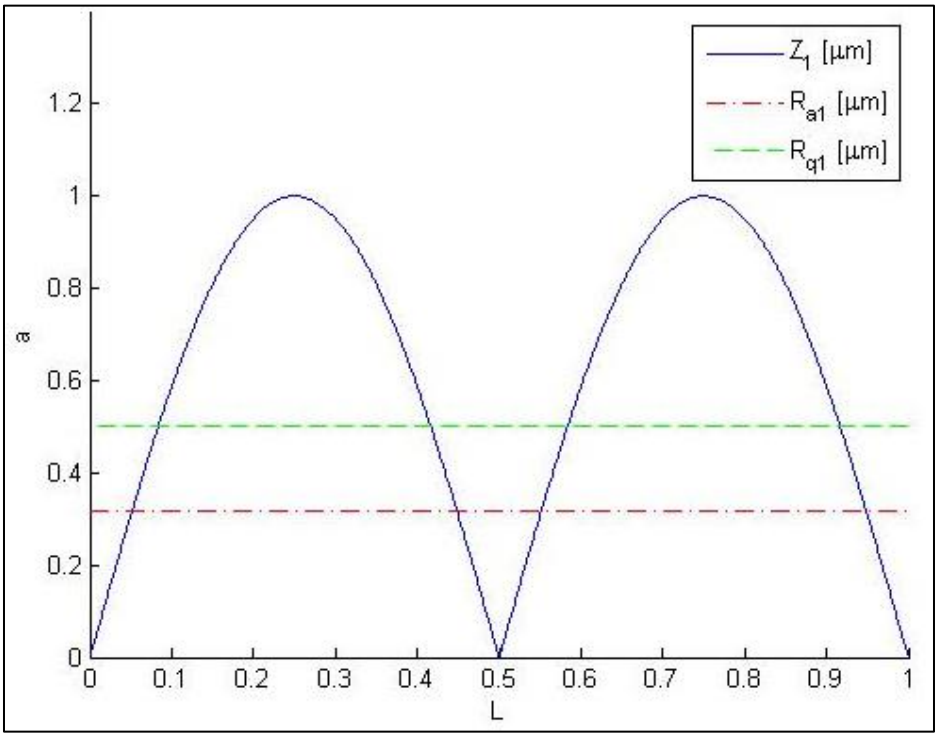

Figure 2.6: Simple theoretical surface without nano-roughness as per equation (2.3).

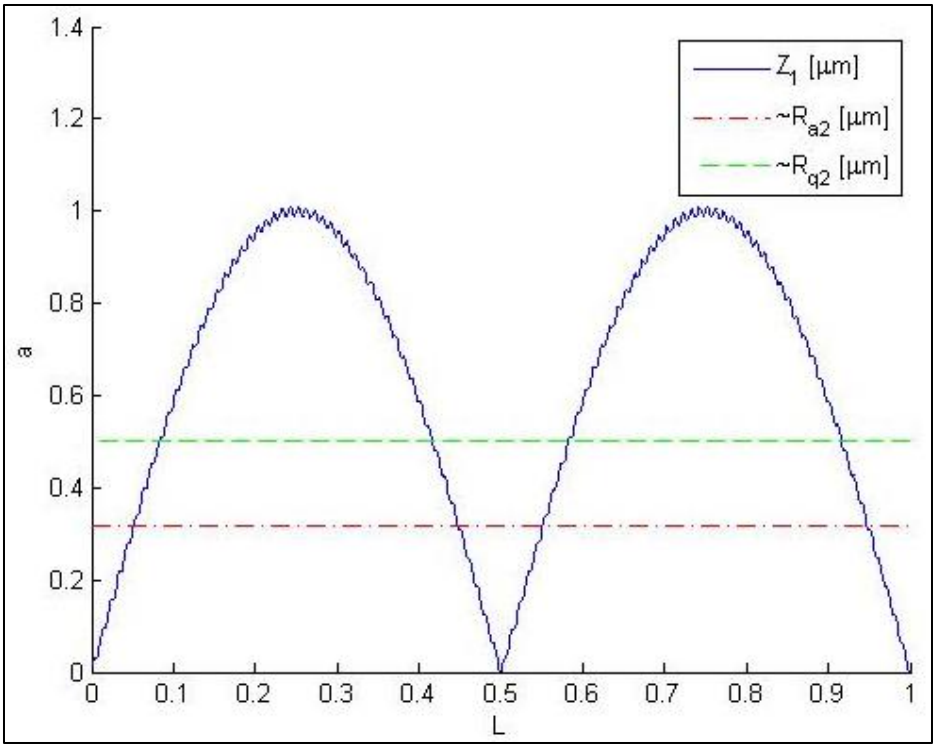

Figure 2.7: Theoretical surface with nano-roughness as per equation (2.4).

Table 2.1: Surface Roughness Measurements by AIF				
Metal	Copper		363 Brass	
Surface Treatment	Baseline	CuO Structures	Baseline	CuO Structures
R_a [μm]	0.153	0.117	0.489	0.434
R_q [μm]	0.248	0.191	0.713	0.550

CHAPTER 3: IMPROVING BOILING HEAT TRANSFER WITH COPPER OXIDE SURFACE STRUCTURES

3.1: Motivation

As microchips get smaller with ever increasing power densities, methods of electronics cooling must continue to adapt to handle the increasing loads. Any and all minor improvements that can increase the heat transfer coefficient should be explored for practicality and cost effectiveness, as even the smallest increase in the COP of a system can save valuable time and money. Microchanneled heat sinks utilize boiling refrigerants to remove heat from these systems. Because the heat flux is so high and local, atypical techniques can be used to improve the heat transfer that would not be as practical in traditional HVAC applications.

As shown in the previous chapter, modifying both copper and brass surfaces by adding a layer of copper oxide surface structures effectively increases the true area of the surface through nanoroughness while not affecting the bulk roughness measurements. In this chapter, CuO surface structures will be applied to a cold plate evaporator with single pass microchannels; boiling heat transfer coefficients will then be calculated for both the uncoated baseline condition and the modified condition with R134a as the refrigerant. If the addition of the surface structures truly increases the wetted area of the refrigerant and allows for greater bubble

nucleation, then the heat transfer coefficient should noticeably increase from the baseline to modified conditions. If the surface modifications do not alter the bulk roughness as suggested, then there should be no significant increase in the pressure drop.

3.2: Test Specimen

Figures 3.1 and 3.2 respectively display the cold plate evaporator with internal and external views. This cold plate was designed to remove heat from power electronics. It has multiple, single-pass parallel microchannels leading from a single entrance to a single exit. The louvered entrance and exit in Figure 2.1 allow for even flow distribution among the microchannels. Multiple plates can be combined in series or parallel configurations so that any specific heat load can be managed efficiently.

The cold plate's body consists of two main parts: a brass cavity (Figure 3.1) containing the microchannels and a copper plate for higher thermal conductivity on the heated side. These two parts are then brazed together to form the evaporator, along with additional inlet and exit to allow for easy connection to piping systems. In terms of scale, it is approximately five inches long, three inches wide, and one inch thick. Then, with all internal surfaces provided by the microchannels, the cold plate has an internal area of approximately 34 cm^2.

3.3: Testing Facility

The test facility was built from the ground up specifically for this experiment. All components were thus chosen in order to cover the necessary ranges in pressure, mass flow rate, and heat flux required for the experiment.

3.3.1: Facility Diagram

Figure 3.3 shows the overall experimental diagram for the facility and refrigerant loop. The loop starts with the micropump which provides the necessary pressure jump to drive refrigerant flow. In parallel to the micropump is a bypass valve to assist in flow control and charging the system with R134a. Next, a flow meter measures the mass flow rate while the refrigerant is a subcooled liquid. Next, P_1 and T_{sub} are, respectively, a pressure transducer and insertion thermocouple pair which measure the pressure and temperature at the outlet of the micropump; these two measurements define the subcooled state of the refrigerant at point 1. Next, a Watlow insertion heater acts as the preheater for the system. When the subcooled state is known and a known amount of heat, Q_{PH}, is added to the system, the quality of the two-phase fluid at the exit of the preheater, X_2, can be determined. After the preheater, P_2 and T_{in} measure the pressure and temperature at the exit of the preheater to determine saturated conditions.

Next in the loop is the cold plate test section of interest. Figure 3.4 shows the cold plate as it is installed in the system. This installation consists of a number of components, all encompassed in black foam insulation to reduce heat losses. First, ΔP as shown in Figure 3.3 indicates a differential pressure transducer measurement used to measure the pressure drop across the cold plate. Next, the cold plate is seen with both its brass and copper sections. Wall temperature by five wired T-type thermocouples—T_{CP1} through T_{CP5}—embedded in the cold plate as seen in Figure 3.5. These thermocouples are sandwiched between the cold plate and a ½" thick copper spreader plate, which is included to better spread out the heat provided by the two resistive heaters. Initial testing showed that the temperature distribution across the cold plate was too non-uniform, indicating that the heaters do not heat 100% evenly; thus, the spreader plate provides a more even heat flux. At the exit of the cold plate, one final insertion thermocouple, T_{out}, is included to measure the temperature at the outlet of the cold plate. This measurement, in combination with the pressure drop and cold plate power input, allows for the exit quality of the cold plate, X_3, being determined.

The refrigerant loop finishes with components used to bring the system back to a subcooled state; since they are past the test section of interest, no further measurements are taken. The refrigerant is condensed in a brazed plate heat exchanger; after a receiver—used to visualize the fluid and store extra refrigerant—

it is subcooled in another brazed plate heat exchanger to ensure good operation of the micropump.

As previously mentioned, the facility also has an open-loop water system to provide cooling to the condenser and subcooler. Water is pulled directly from the sink in the lab through a nylon hose. Water temperature control ranges from approximately 15 °C to approximately 55 °C. T_{win} is an insertion thermocouple which measures the inlet water temperature before any heat has been exchanged with the refrigerant, while T_{wout} is another insertion thermocouple which measures the outlet water temperature after heat has been transferred between the refrigerant and the water.

Through a system of four different needle valves, the water flows through the subcooler and then through the condenser. Based on which valves in this system are open, the water can be directed through the open-loop in multiple configurations. Water can be directed through only the condenser, only the subcooler, both heat exchangers in different ratios, or through neither heat exchanger; this system allows for great flexibility as the refrigerant is cooled to subcooled conditions.

Figure 3.6 shows the full test facility. As compared to Figure 3.3, one can see that most of the system has been insulated with ½" black foam insulation to ensure that

the facility had minimal heat loss in the regions of interest—in the refrigerant loop, from the micropump to the outlet of the cold plate. Some sections of the test facility, such as the water side and in between the condenser, receiver, and subcooler, were not insulated as they were not part of the relevant test section.

3.3.2: Copper Oxide Surface Structure Application

Previous work has verified that the CuO structures can be effectively grown on copper and brass by immersion. Coating the internal area of a brazed cold plate proved to be a more difficult challenge. To do this, a chemical bath was prepared at the proper temperature. The cold plate was partially removed from the system so that only the brass tubing was disconnected while all heaters, thermocouples, and insulation were left untouched. After inclining the plate, a funnel was attached to one end and a draining spigot to the other as seen in Figure 3.7. The chemical bath was then poured through the evaporator at a low flow rate with the heaters on to maintain the oxidation temperature as prepared in the bath. After multiple passes, the evaporator's internal area was effectively coated.

To verify that this process worked effectively, it was also completed on a spare cold plate not installed in the system. After modification, this cold plate was sliced open by wire EDM to visualize the internal surfaces. For reference, Figure 3.8 shows how the ½" by ½" samples appear before and after modification. The oxide layer causes

copper surfaces to turn jet black, while the brass surfaces turn to a much darker brown but not quite fully black color. Figure 3.9 compares the baseline internal brass cavity to the cold plate that had been coated and then cut by EDM. Visually, this confirms that this coating process effectively grows the CuO surface structures onto the internal surface area of the cold plate. For a more extensive look at how the cold plate was modified, please refer to Appendix A.

3.4: Experimental Methods

This section overviews all methods used to obtain the relevant experimental data for this experiment, including all of the measurements made for each test and each of the relevant testing regimes. For component calibration, please refer to Appendix C.

3.4.1: Obtained Measurements

All measurements were obtained using an HP 75000 Series B data logger using VEE with Microsoft Excel and REFPROP software. The VEE software pulled all measurements as simple voltage signals in two second intervals from the data logger. These data were then converted from raw voltages to temperature, pressure, power, and mass flow rate measurements based on calibration data. These data were then output into an open Excel file to later be saved. All data were transferred to the Excel file both as raw voltage signals and as converted signals in

proper units of °C, kPa, W, and g/s for temperature, pressure, power, and mass flow rate, respectively. For more details on the data logging equipment and code development please refer to Appendix B.

Throughout the experimental facility, thirteen temperature measurements are obtained for each point in a data set; Table 3.1 shows all of these temperature measurements, further specifying what type of thermocouple was used, a description of the measurement obtained, and what the measurement is used for. Similar to Table 3.1, Table 3.2 shows how each of the pressure, power, and mass flow rate measurements were obtained and what each was used for.

3.4.2: System Control

For all experiments, the system was controlled manually. While different testing conditions have different control points and different measurements of interest, all experiments roughly follow the same pattern for how to control the system, which is reviewed in this section.

All experiments start by initiating the VEE and Excel programs for visual feedback of all measurements. Figures 3.10 and 3.11 show the visual output provided by the Excel and VEE code for a typical test. In Figure 3.10, a number of real time data are calculated from the measurements in Excel, including the inlet and exit qualities of

the cold plate, power losses to the environment, a P-h diagram with current enthalpies, and more. Figure 3.11 provides real time visualization of the measurements taken, such as temperature, mass flow rate, pressure, and power.

Next, the water supply from the building is turned on. Setting this water temperature indirectly sets the saturation temperature of the boiling R134a. Due to the water supply running through the steam room in the basement of the building, it can take up to an hour—often less—for the water temperature to reach steady state. If testing started before the water temperature reaches a steady temperature, the saturation temperature would fluctuate and make it virtually impossible for the system to reach steady state. The water side valves seen in Figure 3.3 were utilized here to prevent water from interacting with the refrigerant before reaching a steady temperature by closing off the condenser and subcooler. Steady state water temperature is verified by the inlet and outlet water temperature readout in VEE (Figure 3.11.A). After achieving the desired water temperature, the micropump is turned on and adjusted to the desired refrigerant mass flow rate for the test condition being explored. Visual feedback from the VEE program (Figure 3.11.B) allows for very tight control of this mass flow rate—with achievable increments as small as 0.2 g/s.

After this, the preheater and cold plate heaters are switched on using the two variable voltage power supplies. Initially, they are set to very rough values to ensure

that the flow is two-phase at both the inlet and the exit of the cold plate without any control of the actual qualities; this is verified by the real time P-h diagram provided by the Excel feedback (Figure 3.10.A). The system is allowed to reach steady state with this rough control, which is verified by the steadiness over time of the temperature (Figure 3.11.A, Figure 3.11.C, Figure 3.11.D), pressure (Figure 3.11.E), power (Figure 3.11.F), and mass flow (Figure 3.11.G) plots in the VEE program.

Once the system is roughly steady state with the desired saturation temperature, cold plate power, preheater power, and mass flow rate, these set points can all be slowly tweaked to match the desired testing conditions. The mass flow rate should be the first control point changed in small increments depending on the required testing conditions. Then, to set specific inlet and exit qualities, heater powers are adjusted. The inlet condition is first set by adjusting the preheater power. As Q_{PH} is raised or lowered, the enthalpy of point 2 on the P-h diagram in the Excel output (Figure 3.10.A) adjusts within the vapor dome, and X_2 as calculated by enthalpy and saturation temperature can be monitored visually (Figure 3.10.B). Once mass flow rate and inlet quality are set, X_3 can similarly be set by adjusting the cold plate power Q_{CP} while monitoring X_3 (Figure 3.10.C) and point 3 on the P-h diagram (Figure 3.10.A) until the desired outlet quality is achieved.

Once all test parameters are set—mainly T_{sat}, Q_{PH}, Q_{CP}, and $\dot{m}$—the system is allowed to reach true steady state and a data point is collected. Each data point includes all measured parameters, all raw voltages output by the measurement devices (in case recalibration is needed after testing), and all calculated quantities. These values are all recorded over time for the experiment; the steady state portion can then be isolated and averaged to provide the final data point for all measured and calculated. After this is completed, testing continues by readjusting power and mass flow rates as needed to collect the next data set.

Once all data sets are collected for the baseline cold plate in this manner, all tests are repeated with the exact same testing conditions and the same cold plate. It is important to note that the only thing that changed in the testing setup from the baseline to modified cold plate is the addition of the surface structures. All insulation, thermal grease, heater attachments, and heat loss calibrations were kept identical from baseline to modified testing, with the same cold plate being used for both rounds of testing. This provides a sound argument that any error propagation in the baseline testing will carry over to the modified testing; even if error bars overlap, there is an argument that the surface structures provide improvement.

3.4.3: Test 1: T_{sat} Dependence

The purpose of this test is to determine the dependence of the heat transfer coefficient across the cold plate on saturation temperature. These tests were performed with constant mass flow $\dot{m}$, constant inlet quality X_2, and constant outlet quality X_3. Figure 3.12 shows a P-h diagram of a typical test for condition 1. The target for X_2 was 0.1 to guarantee two phase flow at the entrance to the cold plate so that nucleate boiling occurs. The target for X_3 was 0.7 to guarantee that the full nucleate boiling regime is captured with the outlet condition being past the critical heat flux. The target for the mass flow rate was 3.9 g/s. With X_2, X_3, and $\dot{m}$ conditions, the resulting Q_{CP} values are representative of a true loading of the cold plate in industry. As seen in the representative P-h diagram in Figure 3.12, a data set is first collected at a low saturation temperature; this minimum temperature (~23 °C) relates to the coldest water temperature available from the lab faucet. Saturation temperature was then increased by increasing T_{win}. Tests continued until the T_{win} reached a maximum as determined by the hottest water temperature from the lab faucet.

3.4.4: Test 2: h with Varying Mass Flux and Heat Flux

This purpose of this test is to determine how the addition of CuO surface structures changes the heat transfer coefficient across the cold plate when mass flux and heat flux are varied simultaneously. All tests were performed with constant X_2, constant X_3, and constant T_{sat}. Figure 3.13 shows an example P-h diagram of a typical data set

for test 2. Note that with constant inlet and exit qualities with constant saturation temperature, all data sets for this test will occupy the same space on the P-h diagram. The target for X_2 was again 0.1, while the target for X_3 was increased to 0.75 to allow for the system to reach its maximum possible heat flux in the cold plate with the available mass flow rates. The target for T_{sat} was 55 °C: the hottest temperature available to provide the best match to typical testing conditions in industry. Mass flow rate $\dot{m}$, cold plate power Q_{CP}, and preheater power Q_{PH} were all varied to maximize the testing range.

A data set was first collected with the lowest achievable and consistent $\dot{m}$ from the micropump. Then, $\dot{m}$ was slowly increased for each data set with Q_{PH} and Q_{CP} being increased accordingly to keep the target qualities consistent for each test. These three values were increased together in steady increments until the maximum allowable Q_{CP} for the variable voltage supply was reached.

3.4.5: Test 3: h at Local Qualities

The purpose of this test is to determine if the heat transfer coefficient changes at different local qualities for both the baseline and modified parameters. Where previous tests held X_2 and X_3 constant, here the difference between the inlet and exit qualities, ΔX, was kept constant at 0.1. This was achieved by holding $\dot{m}$ and Q_{CP} constant at 5.0 g/s and 75 W, respectively. This combination allows for higher heat

flux so that any difference in heat transfer from the baseline to modified cold plate can be better seen. T_{sat} was kept constant with the same target as Test 2 at 55 °C. Figure 3.14 shows an example P-h diagram of the data sets for this test. The starting value for X_2 was 0.1. After steady state was reached, Q_{PH} was increased incrementally to push the X_2 and X_3 further into the vapor dome in the direction of the arrow. With ΔX being small, the average quality, X_{avg}, can be found by averaging X_2 and X_3; then, each heat transfer coefficient h_{local} can be found. Tests continued until Q_{PH} reached its maximum value as allowed by the variable voltage supply.

3.5: Data Reduction

All relevant quantities can be determined from the measurements taken as summarized in Tables 3.1 and 3.2 for all tests. This section serves as a guide to how all of these data were processed to form logical conclusions about the effectiveness of the CuO surface structures on the heat transfer within the cold plate.

3.5.1: Heat Loss Calculation

Even though the cold plate and surrounding parts of the system were well insulated, the large temperature difference between the saturation temperature and ambient temperature led to some power losses to the environment in both the preheater and the cold plate heater. To calibrate these losses, an overall UA heat transfer coefficient was determined for each heater by the following equations.

$$Q_{PH,losses} = UA_{PH} * \left(\frac{T_{sub}+T_{in}}{2} - T_{amb}\right) \quad (3.1)$$

$$Q_{CP,losses} = UA_{CP} * \left(T_{incp} - T_{amb}\right) \quad (3.2)$$

Here $Q_{PH,\ losses}$ is the calculated heat losses for the preheater [W] and UA_{PH} is the overall heat loss coefficient for the preheater [W/°C]; $Q_{CP,\ losses}$ is the calculated cold plate losses [W] and UA_{CP} is the overall heat loss coefficient for the cold plate heater [W/°C]. For both equations, a temperature difference is multiplied by a loss coefficient to calculate the heat losses. In equation (3.1), an average fluid temperature within the preheater was used as the reference internal temperature—$(T_{sub}+T_{in})/2$—while equation (3.2) uses the outer surface temperature—T_{incp}—of the cold plate as the reference internal temperature. Either method is acceptable, as the UA coefficient can be calibrated to either temperature. Table 3.3 shows the calculated heat loss coefficient values for all tests; for more details on how these loss coefficients were calculated, refer to Appendix C. With these UA values, corrected values for the preheater and cold plate power were calculated based on the following relations.

$$Q_{PH,adj} = Q_{PH} - Q_{PH,losses} \quad (3.3)$$

$$Q_{CP,adj} = Q_{CP} - Q_{CP,losses} \quad (3.4)$$

3.5.2: Saturation Temperature

Saturation temperature can be measured by two different ways. First, the thermocouples within the two-phase fluid—in this case, T_{in} and T_{out}—can be assumed to be T_{sat}. However, the saturation pressure and saturation temperature are always paired in a two-phase fluid; therefore, a saturation pressure measurement can also be an effective way to measure saturation temperature from either fluid property tables or fluid property software such as REFPROP.

3.5.3: Enthalpy and Quality Determination

Three different enthalpies are determined within the system: h_1 refers to the enthalpy at the subcooled state before the preheater; h_2 refers to the enthalpy at the inlet to the cold plate after the preheater has added its heat to the refrigerant; h_3 refers to the final enthalpy after the outlet of the cold plate. Once the two enthalpies h_2 and h_3 are determined within the two-phase dome, inlet and outlet qualities X_2 and X_3 can be easily determined from REFPROP fluid property software based on saturation pressure and enthalpy.

h_1 is the most straightforward enthalpy to determine; since the fluid is a subcooled liquid at this state, this enthalpy was simply determined by T_{sub} and P_1 within REFPROP. For h_2 and h_3, calorimetry must be used since the fluid is two-phase and

temperature and pressure alone are not enough to uniquely determine the enthalpy. For h_2, the enthalpy was determined by the following equation.

$$h_2 = h_1 + \frac{Q_{PH,adj}}{\dot{m}} \tag{3.5}$$

Here h_2 is the enthalpy after the preheater [kJ/kg], h_1 is the enthalpy before the preheater as determined by subcooled conditions [kJ/kg], $Q_{PH,adj}$ is the adjusted preheater power [W], and $\dot{m}$ is the mass flow rate [g/s]. This method determines the enthalpy at the inlet of the cold plate even though it is a two-phase fluid since enthalpy and saturation temperature are independent of each other unlike T_{sat} and P_{sat}. By extension, X_2 can be determined with P_2 and h_2 within REFPROP. The final enthalpy—h_3 at the outlet of the cold plate—is determined by a similar process to h_2, as described by this equation.

$$h_3 = h_2 + \frac{Q_{CP,adj}}{\dot{m}} \tag{3.6}$$

Assuming that equation (3.5) correctly calculates the enthalpy at the cold plate inlet, the same process can be extended to calculate the enthalpy at the cold plate outlet by adding the additional enthalpy provided to the fluid by the adjusted cold plate power, $Q_{CP,\,adj}$ [W]. With h_3 and P_3 known, X_3 can be determined with REFPROP.

3.5.4: Heat Transfer Coefficient Calculation

Two methods were used to calculate a heat transfer coefficient across the cold plate; they each relate to the two different methods mentioned for determining the

saturation temperature in section 3.5.2. This heat transfer coefficient, $h_{overall}$, is an average heat transfer coefficient across the cold plate for inlet and exit qualities of X_2 and X_3. For tests 1 and 2, this encompasses both the nucleate boiling and convective boiling regimes; for test 3, X_2 and X_3 are so close that the average heat transfer coefficient can be treated as a local heat transfer coefficient instead at a quality half way between X_2 and X_3.

For both methods, the following equation was used to calculate $h_{overall}$.

$$h_{overall} = \frac{Q_{CP,adj}}{A*\Delta T} \tag{3.7}$$

Here, $Q_{CP,adj}$ is the adjusted cold plate power [W], A is the internal surface area of the cold plate microchannels [m^2], and ΔT is a temperature difference between the saturation temperature T_{sat} [°C] and the average wall temperature, $T_{CP,avg}$ [°C] ($T_{CP,avg}$ is the average of temperatures T_{CP1} through T_{CP5}). Thus, $h_{overall,P}$ and $h_{overall,T}$ below are defined as the same heat transfer coefficient across the cold plate but with T_{sat} either determined by a thermocouple or a pressure transducer, respectively.

$$h_{overall,P} = \frac{Q_{CP,adj}}{A*(T_{CP,avg} - T_{sat,2})} \tag{3.8}$$

$$h_{overall,T} = \frac{Q_{CP,adj}}{A*\left(T_{CP,avg} - \frac{T_{in}+T_{out}}{2}\right)} \tag{3.9}$$

Here $T_{sat,2}$ is the saturation temperature as determined by the pressure transducer P_2 [°C] and (T_{in} + T_{out})/2 provides an average saturation temperature as determined by all thermocouples that are immersed in the two-phase fluid. Ideally, $h_{overall,P}$ will

exactly equal $h_{overall,T}$ if the system is perfectly calibrated; however, this is an unrealistic scenario. In reality, there were slight differences in the measurements for $T_{sat,2}$, T_{in}, and T_{out} even though they should be measuring the same value. Because it is difficult to tell which is more accurate at determining the saturation temperature—thermocouple or pressure transducer—the overall heat transfer coefficient averages the two saturation temperatures to merge the error.

$$h_{overall} = \frac{Q_{CP,adj}}{A*(T_{CP,avg} - T_{sat,avg})} \tag{3.10}$$

$$T_{sat,avg} = \frac{T_{sat,2} + \frac{T_{in}+T_{out}}{2}}{2} \tag{3.11}$$

3.5.5: Error Propagation

By the nature of any measurement, there will be uncertainty in that quantity that carries through to any values that are calculated using it. The base measurements in this experiment—as outlined in Tables 3.1 and 3.2—all have their own specific errors associated with them. These errors are determined in Appendix C and are summarized in Table 3.4.

To determine the relative error of calculated heat transfer coefficients, a simplified form of the Law of Propagation of Uncertainty is utilized, provided as equation (3.12) below [6].

$$\sigma_Z = \sqrt{\sum_{i=1}^{N} \frac{\partial Z}{\partial i} * {\sigma_i}^2} \tag{3.12}$$

In this equation, σ_Z is the error for an arbitrary calculated measure, Z. Each value i from 1 to N are the N different variables that compromise the function $Z(i_1, i_2, \ldots i_N)$. Each σ_i is thus the error of each of the individual components that make up the function Z. For this experiment, the most relevant measure is $h_{overall}$, which is a function of $Q_{CP,adj}$, A, $T_{sat,avg}$, and $T_{CP,avg}$. Equation (3.12) can then be rewritten with Z being substituted with $h_{overall}$ and the four variables mentioned can be substituted in for i = 1 through 6.

$$\sigma_{h_{overall}} = \left(\frac{\partial h_{overall}}{\partial Q_{CP,adj}} * {\sigma_{Q_{CP,adj}}}^2 + \frac{\partial h_{overall}}{\partial A} * {\sigma_A}^2 + \frac{\partial h_{overall}}{\partial T_{sat,avg}} * {\sigma_{T_{sat,avg}}}^2 + \frac{\partial h_{overall}}{\partial T_{CP,adj}} * {\sigma_{T_{CP,adj}}}^2\right)^{0.5} \tag{3.13}$$

This equation expands equation (3.12) for the variables of $h_{overall}$. To get an expression for the error of $h_{overall}$, the differentials must be strictly defined. Equations (3.14) through (3.17) define the differential terms in equation (3.13) for each variable by expanding the partial derivatives.

$$\frac{\partial h_{overall}}{\partial Q_{CP,adj}} = \frac{1}{A*(T_{CP,avg} - T_{sat,avg})} \tag{3.14}$$

$$\frac{\partial h_{overall}}{\partial A} = \frac{-Q_{CP,adj}}{A^2*(T_{CP,avg} - T_{sat,avg})} \tag{3.15}$$

$$\frac{\partial h_{overall}}{\partial T_{CP,avg}} = \frac{-Q_{CP,adj}}{A*(T_{CP,avg} - T_{sat,avg})^2} \tag{3.16}$$

$$\frac{\partial h_{overall}}{\partial T_{sat,avg}} = \frac{Q_{CP,adj}}{A*(T_{CP,avg} - T_{sat,avg})^2} \tag{3.17}$$

Lastly, Since $T_{sat,avg}$ is a function of both thermocouple and pressure transducer measurements, equation (3.18) defines a combined error $\sigma_{Tsat,avg}$ that compounds the error of σ_{TC} and σ_P from Table 3.4 by applying equation (3.12) with $T_{sat,avg}$ from equation (3.11) in place of Z.

$$\sigma_{T_{sat,avg}} = \left(\frac{T_{in}+T_{out}}{4} * {\sigma_{TC}}^2 + \frac{T_{sat,2}}{2} * {\sigma_{Tsat(P)}}^2 \right)^{0.5} \quad (3.18)$$

Here $\sigma_{Tsat(P)}$ is the error of the pressure transducers σ_P transformed into units of °C when considering saturation temperature as a function of pressure. For simplicity, $\sigma_{Tsat,avg}$ will be assumed to be ±0.2 °C, as this is the temperature difference seen when the pressure transducer error σ_P is converted from kPa to °C at the typical saturation pressure seen in all tests, 1400 kPa (i.e. 1400±5 kPa translates to 52.4±0.2 °C at saturated conditions). Therefore, with equations (3.13) through (3.18) and the measurement errors from Table 3.4, error bars can be calculated for the heat transfer coefficient $h_{overall}$.

3.5.6: Mass Flux

As a note, while the mass flow rate $\dot{m}$ [g/s] was useful during testing, a more appropriate measure to compare heat transfer coefficients is the mass flux through the cold plate, g_{CP} [kg/m^{2}s], which can be found directly from $\dot{m}$ and the cross sectional area of the microchannels, A_C.

$$g_{CP} = \frac{\dot{m}}{A_C} * \frac{1kg}{1000g} \quad (3.19)$$

Here $\dot{m}$ is in units of [g/s] and A_C is in units of [m^2]. A_C was pulled from the model geometry and was calculated as 17.3 mm^2, or $1.73*10^{-5}$ m^2.

3.6: Results and Discussion

For the sake of consistency, all presented results will have all baseline tests presented with diamonds and modified tests presented with squares for data points. All background data, calculations, and values required to produce these results are included as tables in Appendix D.

3.6.1: Test 1 Results

Figures 3.15 shows the P-h diagram for the data taken to determine the dependence of $h_{overall}$ on T_{sat} for both the baseline and modified tests. Each data set was taken at four different values for T_{sat}. Mixing hot and cold water to get T_{sat} in the middle of the testing range proved to be very unstable; the two middle temperatures were the only ratios of cold to hot water that could reasonably reach steady state. For all tests, the target entrance quality of $X_2 = 0.1$ was reached successfully with the outlet quality target of $X_3 = 0.7$ holding well.

Figure 3.16 displays the calculated $h_{overall}$ as a function of T_{sat} for both the baseline and modified tests. Overall, the modified cold plate performed better with a heat

transfer coefficient approximately by 2 kW/m^{2}K. This is a good first indication that the heat transfer coefficient improves with the addition of the surface structures. The main takeaway is that $h_{overall}$ has approximately the same linear dependence on the T_{sat} regardless of the surface condition. The baseline tests exhibit a slope of 0.0851 kW/m^{2}K/°C while the modified tests exhibit a slope of 0.108 kW/m^{2}K/°C. This is significant, because it indicates that small fluctuations in saturation temperature do not significantly alter the heat transfer coefficients. For instance, if within the same data set $T_{sat,avg}$ fluctuates from 53 to 57 °C (55±2 °C), one can expect these fluctuations to cause a maximum error in the heat transfer coefficient of ±0.216 kW/m^{2}K. This error is of the same order of the calculated error, $\sigma_{hoverall}$—which, from equation 3.13, was calculated to be ±0.12 kW/m^{2}K. Therefore, even if a data set has saturation temperatures that fluctuate slightly—due to the slight inconsistencies in the supplied water temperature from the building—the associated error with these fluctuations is still very small. To account for this fluctuation, the two errors will be compounded to produce the final $h_{overall}$ error.

3.6.2: Test 2

Figure 3.17 provides a P-h diagram with all test data used to determine how $h_{overall}$ changes for the baseline and modified cold plate tests as $\dot{m}$ and Q_{CP} are increased. The targets for X_2 and X_3—0.1 and 0.75—were held steady over all tests, with maximum fluctuations of ±0.01 and ±0.02, respectively. T_{sat} fluctuated mildly (55±2.3 °C) throughout the data set, which corresponded to the slight fluctuations

seen in Figure 3.17 with the saturation pressure. This is accounted for in the error bars of $h_{overall}$.

Since inlet and outlet qualities were held constant as a control point, the data vary as both $\dot{m}$ and Q_{CP} are increased simultaneously. This method was chosen to better match operating conditions, though it has the drawback of not isolating the effect of $\dot{m}$ and Q_{CP}. Figure 3.18 plots the overall heat transfer coefficient vs. the mass flux, g_{CP}, while Figure 3.19 plots $h_{overall}$ vs. Q_{CP}. Keep in mind that the two plots are so similar because g_{CP} and Q_{CP} were varied simultaneously to keep X_2 and X_3 at 0.1 and 0.75.

At all operating conditions tested, the plate had a higher $h_{overall}$ after applying the CuO surface structures. At higher heat/mass flux—representative of higher operating loads—the effect is stronger than at lower heat/mass flux. Despite covering the same range, the baseline and modified data points do not lie on the exact same values for g_{CP} and Q_{CP}, as this is quite difficult since the system is controlled manually. To quantify how much of an increase is seen in $h_{overall}$, logarithmic curve fits were calculated for each data set to get approximate values for $h_{overall}$ at any value of g_{CP} and Q_{CP} so that the baseline and modified curves can be directly compared. Equations (3.20) and (3.21) show the baseline and modified logarithmic fits for $h_{overall}$ vs. Q_{CP}, and Equation (3.22) shows how to calculate the percent difference between these two curves.

$$h_{overall,base} = 6.3524 * \ln(Q_{CP}) - 19.916 \ [\frac{kW}{m^s K}] \quad (3.20)$$

$$h_{overall,mod} = 8.2937 * \ln(Q_{CP}) - 28.321 \ [\frac{kW}{m^s K}] \quad (3.20)$$

$$\% \ Increase = \frac{h_{overall,mod} - h_{overall,base}}{h_{overall,mod}} * 100\% \quad (3.22)$$

Figure 3.20 shows the percent increase from the baseline and modified data sets over the total range of Q_{CP} with upper and lower limits for the best and worst case scenarios of error propagation. The copper oxide surface structures provide a nominal percent increase of 19.4% in $h_{overall}$ at the highest tested values for Q_{CP}—~600 W—while only providing a nominal 5.7% increase of in $h_{overall}$ at the lower end of Q_{CP}—~100 W. Therefore, the surface structures are not uniformly effective at increasing the heat transfer coefficient across the cold plate for all $\dot{m}$ and Q_{CP}.

It is important to note that even though there are sources of error in the measurements, all of the errors that were inherent to the system setup with the baseline cold plate should be nearly identical to the errors after the surface structures were applied. All settings and components were left completely unchanged between tests, so when comparing the difference between the baseline and modified data, any difference in $h_{overall}$ can directly be attributed to the CuO structures.

3.6.3: Test 3

Figure 3.21 shows all data for test 3 represented on a P-h diagram. The data cover a range of values for the inlet quality X_2 and outlet quality X_3 that encompasses the nucleate boiling regime; the minimum value for X_2 was 0.063, while the maximum value for X_3 was 0.525. This quality range maximized the preheater power Q_{PH} at the target value of $\dot{m}$. The target for $\dot{m}$ (5.0 g/s) for both the baseline and modified tests was reached for all data, with maximum fluctuations of ±0.05 g/s. $T_{sat,avg}$ stayed on target of 55 °C with maximum fluctuations of ±2.2 °C for both the baseline and modified tests. Note that the baseline data stayed at a much steadier saturation pressure/temperature than the modified data; $T_{sat,avg}$ fluctuated by only ±0.5 °C. This was due to steadier water temperatures on the day of baseline testing. This fluctuation is accounted for in the error propagation. Q_{CP} was targeted at 75 W; this in conjunction with the target mass flow rate provided a quality difference from X_2 to X_3 of $\Delta X = 0.1$. Fluctuations in Q_{CP} were relatively small at ±1 W maximum.

The heat transfer coefficient at each data point provides a nominally local value that can be placed at X_{avg} as defined by this equation.

$$X_{avg} = \frac{X_2 + X_3}{2} \tag{3.23}$$

For test 3, $h_{overall}$ and h_{local} are synonymous; h_{local} is calculated in exactly the same fashion as equation (3.10), but it is plotted against quality instead of mass flow rate or heater power. Figure 3.22 shows h_{local} plotted vs. X_{avg} for the baseline and

modified tests, with Figure 3.23 showing the same data on a zoomed axis. Both the baseline and modified curves completely overlap; both margins of error are far larger than any difference between two data points. Initially, this may indicate that the surface structures do not improve heat transfer. However, the power dissipated across the cold plate—Q_{CP} = 75 W—in these tests was very low in order to get ΔX = 0.1. Looking at Figure 3.20, that low of a cold plate power would start to approach a nominal percent increase of 0%, with error bars extending below 0%.

To truly capture the effect of the CuO surface structures at the local level, a stronger system would be necessary. While the heaters are sufficient, if Q_{CP} were increased significantly to better show a significant percent increase from the baseline to modified tests, a much larger mass flow rate would be required to keep ΔX at 0.1 to provide local information. As defined in equation (3.6), the enthalpy h_3 is a function of h_2, $Q_{CP,adj}$, and $\dot{m}$. ΔX is then directly related to Δh.

$$\Delta h = h_3 - h_2 = \frac{Q_{CP,adj}}{\dot{m}} \tag{3.24}$$

So if $Q_{CP,adj}$ is increased to see a higher percent difference, $\dot{m}$ must equally be increased to keep the same ΔX to capture local values, and the micropump installed cannot handle mass flow rates much higher than 8 g/s with consistency. Appendix D provides a full table of all data taken for test 3.

3.6.4: Pressure Drop

While Figure 3.20 shows that $h_{overall}$ shows significant improvement at high heat flux/mass flux, any improvement can be invalidated by a larger pressure drop. In terms of industry, a small increase in the heat transfer coefficient with a large increase in pressure drop will end up costing more to run due to the higher pumping costs, completely negating the benefit of the heat transfer improvement. Therefore, a process is only efficient if it can increase the heat transfer coefficient without significantly increasing the pressure drop.

Figure 3.24 shows the pressure drop for the data in test 2 plotted against the mass flux. The baseline and modified data completely overlap within the margin of error, indicating that the addition of CuO surface structures to the cold plate's internal area has no significant effect on the pressure drop.

This result was expected purely because of the scale of the surface structures. As shown in chapter 2, the roughness values do not significantly change after the oxide layer is deposited since the structures are on a nano-roughness scale that is not detected by traditional R_a and R_q roughness measurements. When adding structures with heights less than 1 μm, the friction factor within the microchannels does not significantly increase enough to significantly affect the pressure drop. Note that part of what keeps ΔP so low and constant across these tests is that the mass

flux is fairly low, always being less than 400 kg/m^{2}s. If the structures were subjected to higher mass fluxes, the friction factor may be strong enough to increase ΔP.

3.6.5: Coating Longevity

Even if this surface modification is both effective at increasing the heat transfer coefficient without increasing the pressure drop, it has to last over time for it to be cost effective in industry. To explore this, two additional data sets were taken for test 2 for the modified cold plate. The first data set as presented in Figures 3.18 and 3.19 was completed immediately after applying the surface structures on May 3rd, 2015. Then, the system was kept charged for a number of weeks, after which test 2 was repeated on June 4th, 2015. After another couple of weeks, one final repetition of test 2 was completed on June 26th, 2015.

Figure 3.25 shows the results of all three modified tests on one plot in comparison to the baseline data. Over the first four weeks from 5/3/15 to 6/4/15, the curve drops slightly. For a reference point, at 250 kg/m^{2}s the predicted nominal percent increase dropped from 18.8% on 5/3/15 to 15.1% on 6/4/15. This percent increase dropped slightly more to 13.7% for the data set taken on 6/26/15, even though the two data curves taken in June appear to overlap each other. Despite this, the later tests still show significant improvement over the baseline data.

To truly understand how time exposed to R134a affects the oxide layer, a more extensive test should be conducted that exposes the surface structures to R134a for longer periods of time until the percent increase drops to 0%, indicating full surface deterioration. To visually observe the change in performance over time, Figure 3.26 plots the nominal percent increase in $h_{overall}$ over time for the reference point of 250 kg/m^2s. This curve was extrapolated linearly to obtain a very rough approximation of the lifetime of the surface's effectiveness on $h_{overall}$. By this linear approximation, the surface should reach a 10% increase after 85 days, a 5% increase 135 days after initial modification, and 0% increase—indicative of total surface deterioration—after 185 days. However, this rough approximation assumes that the deterioration is linear over time which may not be correct. The three data points in Figure 3.26 appear to be concave up, which could indicate that the nominal percent increase may level off and reach some steady value after the top layer of the surface structures have initially worn away. Further, it could simply mean that the surface will still continue to deteriorate, but at a slower rate than the rough linear approximation predicts.

3.7: Conclusions

Copper oxide surface structures were applied to the internal surfaces of a microchanneled cold plate evaporator with the intention of improving the overall heat transfer coefficient. Baseline tests were first completed to find the heat transfer coefficient across the cold plate for a number of loading conditions; the

plate was then modified with the surface structures and tested over the same conditions. It was found that the surface structures improved $h_{overall}$ the most at the maximum load of $Q_{CP,adj}$ = 560 W and $\dot{m}$ = 5.88 g/s with $T_{sat,avg}$ = 54 °C; the structures at this loading provided a maximum percent increase of 19.4%, with lower but still significant improvement seen at lower loading conditions. The improvements made did not significantly change the ΔP, and while the surface structures slightly deteriorated after a month of exposure to R134a, they still proved to increase $h_{overall}$.

3.8: Figures and Tables

Figure 3.1: Parker cold plate brass cavity.

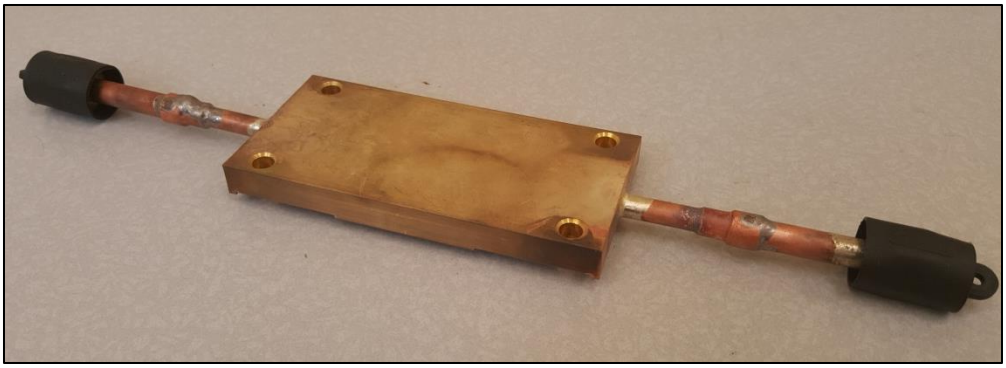

Figure 3.2: Cold plate evaporator after brazing.

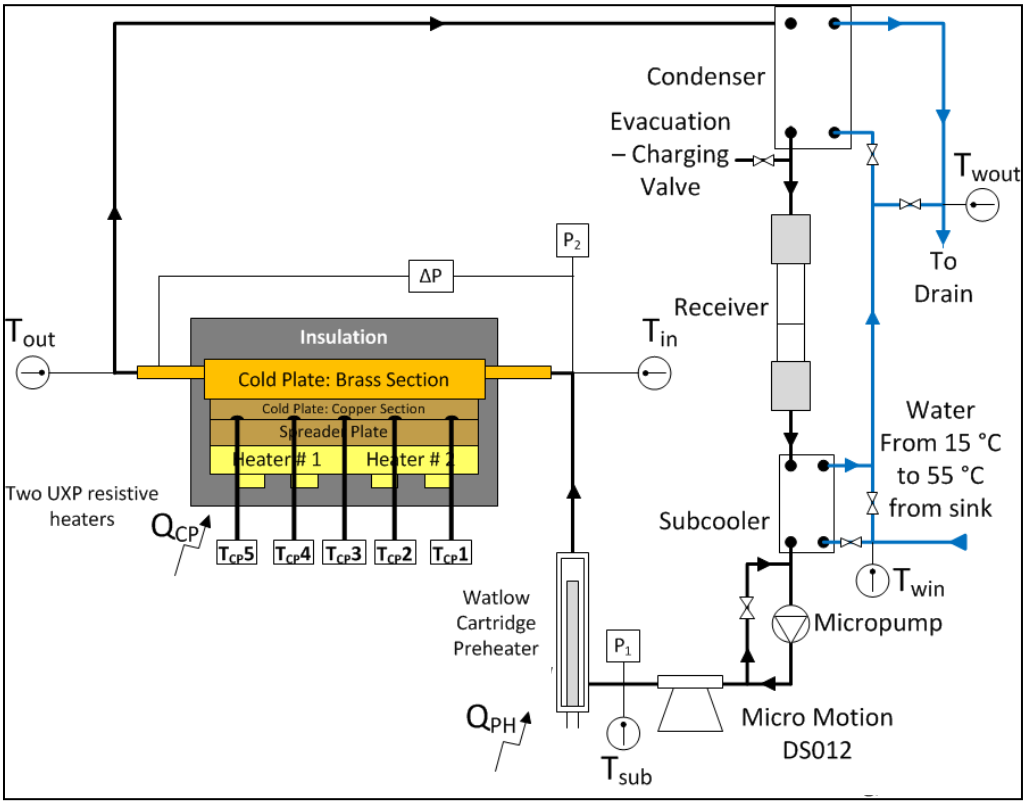

Figure 3.3: Facility diagram displaying all used components and measurements.

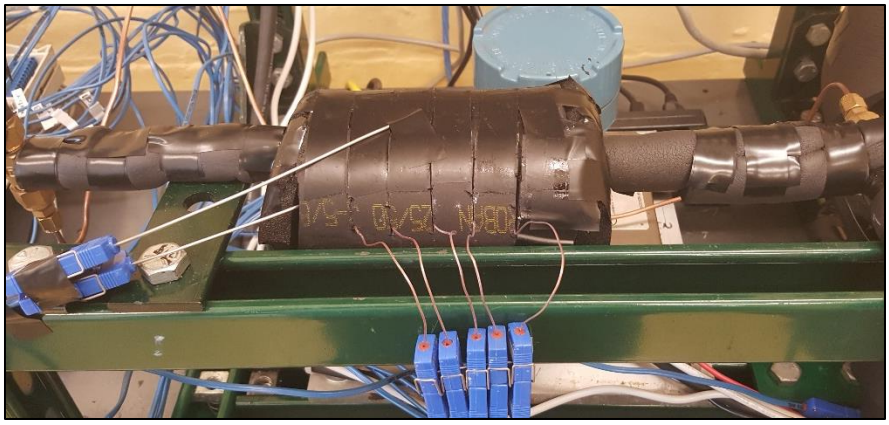

Figure 3.4: Cold plate as installed in the facility for testing.

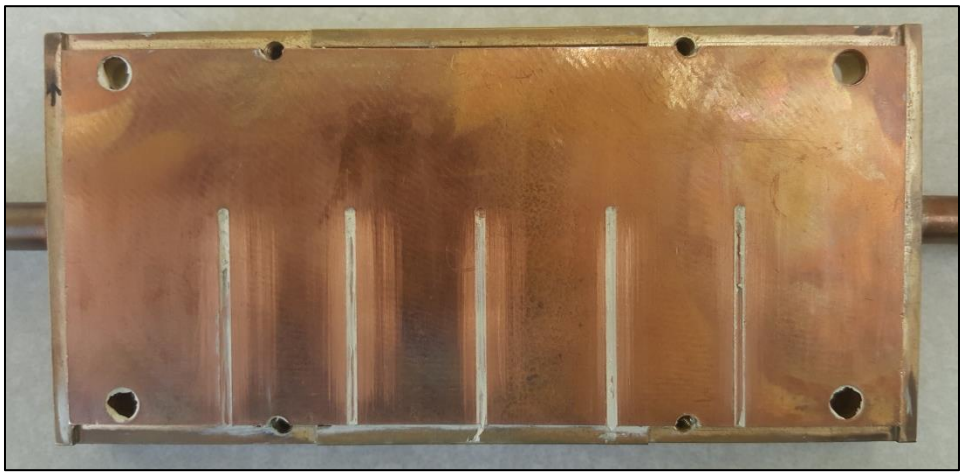

Figure 3.5: Machined channels for thermocouple installation.

Figure 3.6: Fully constructed facility with all insulation.

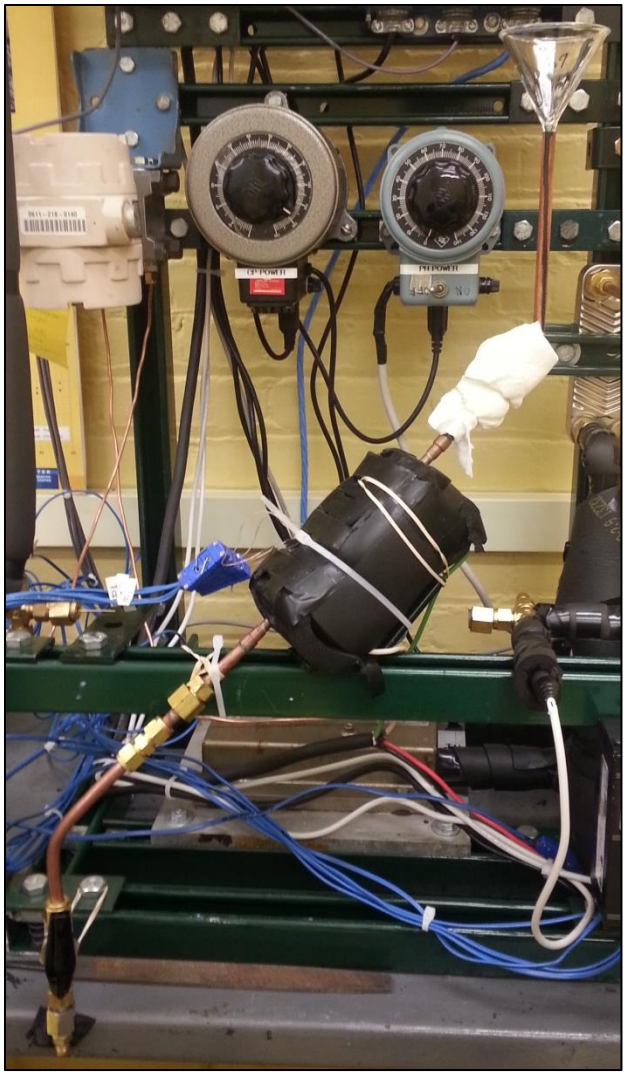

Figure 3.7: Cold plate coating rig.

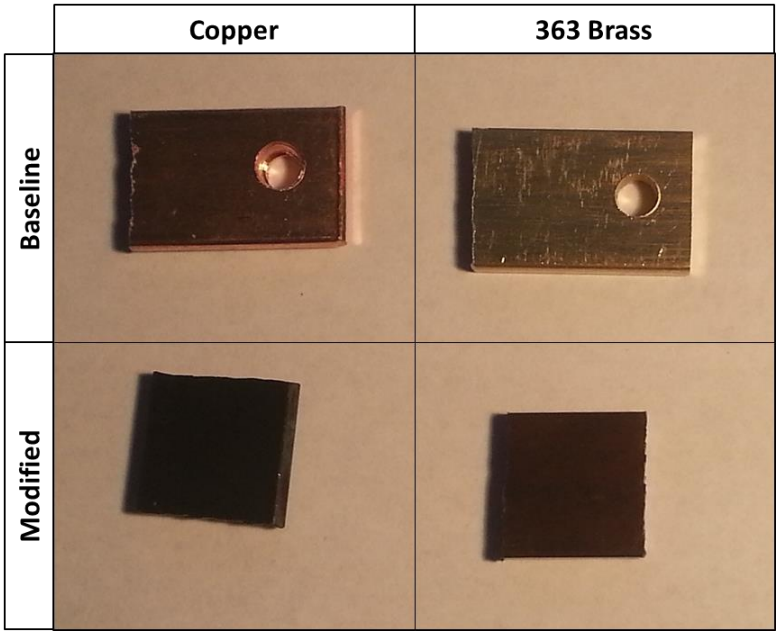

Figure 3.8: Copper and brass samples at true scale.

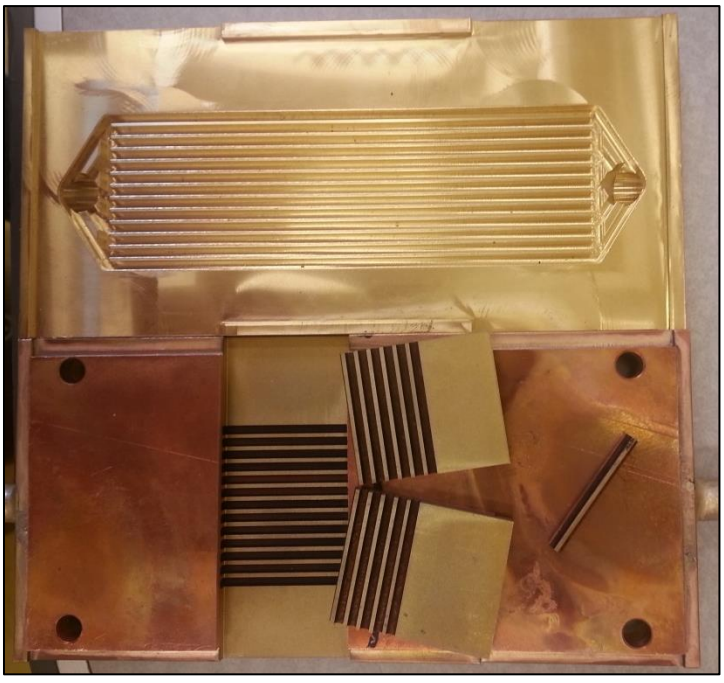

Figure 3.9: Baseline (top) and modified (bottom) internal surface area.

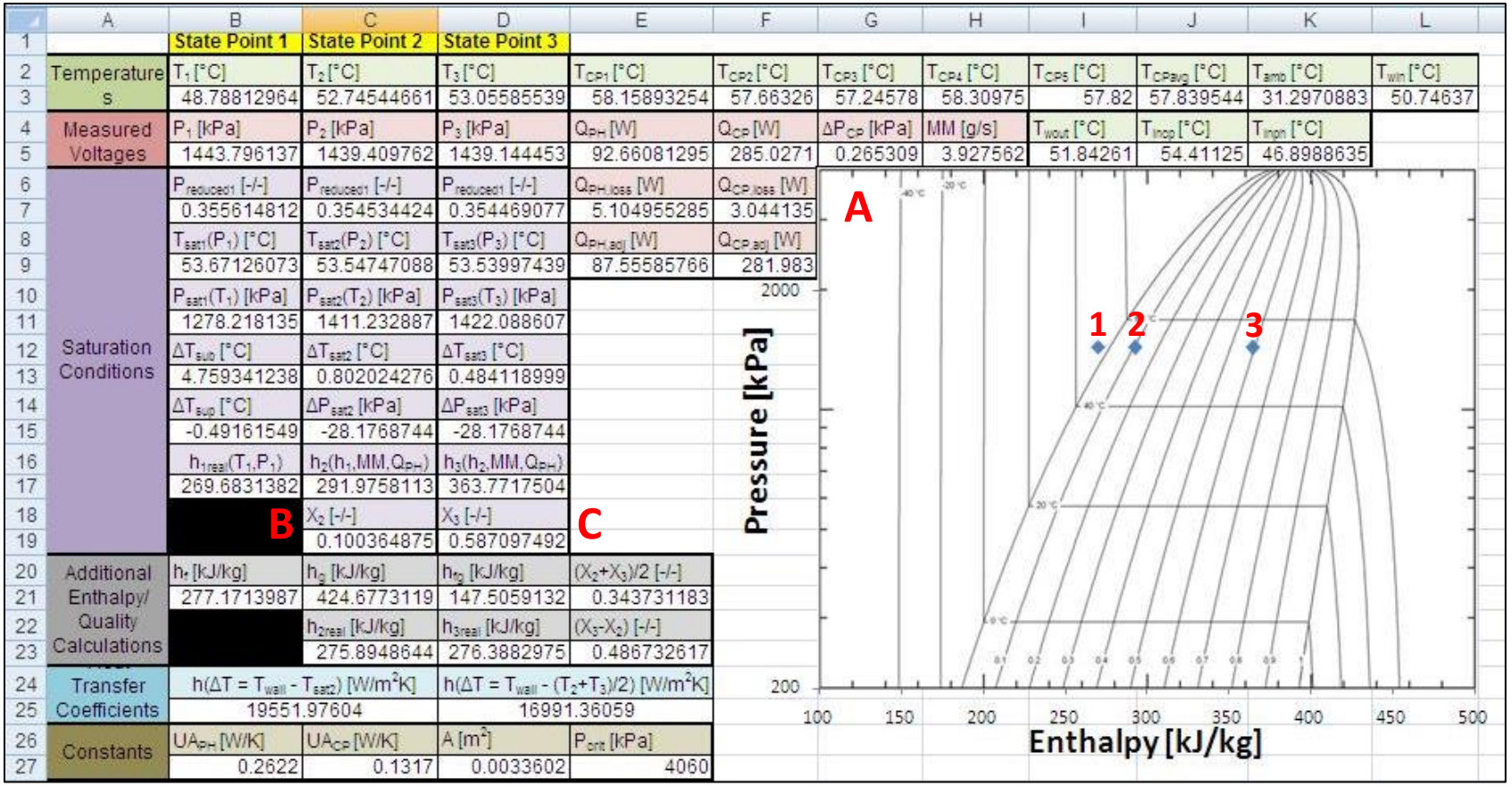

Figure 3.10: Excel feedback for system control.

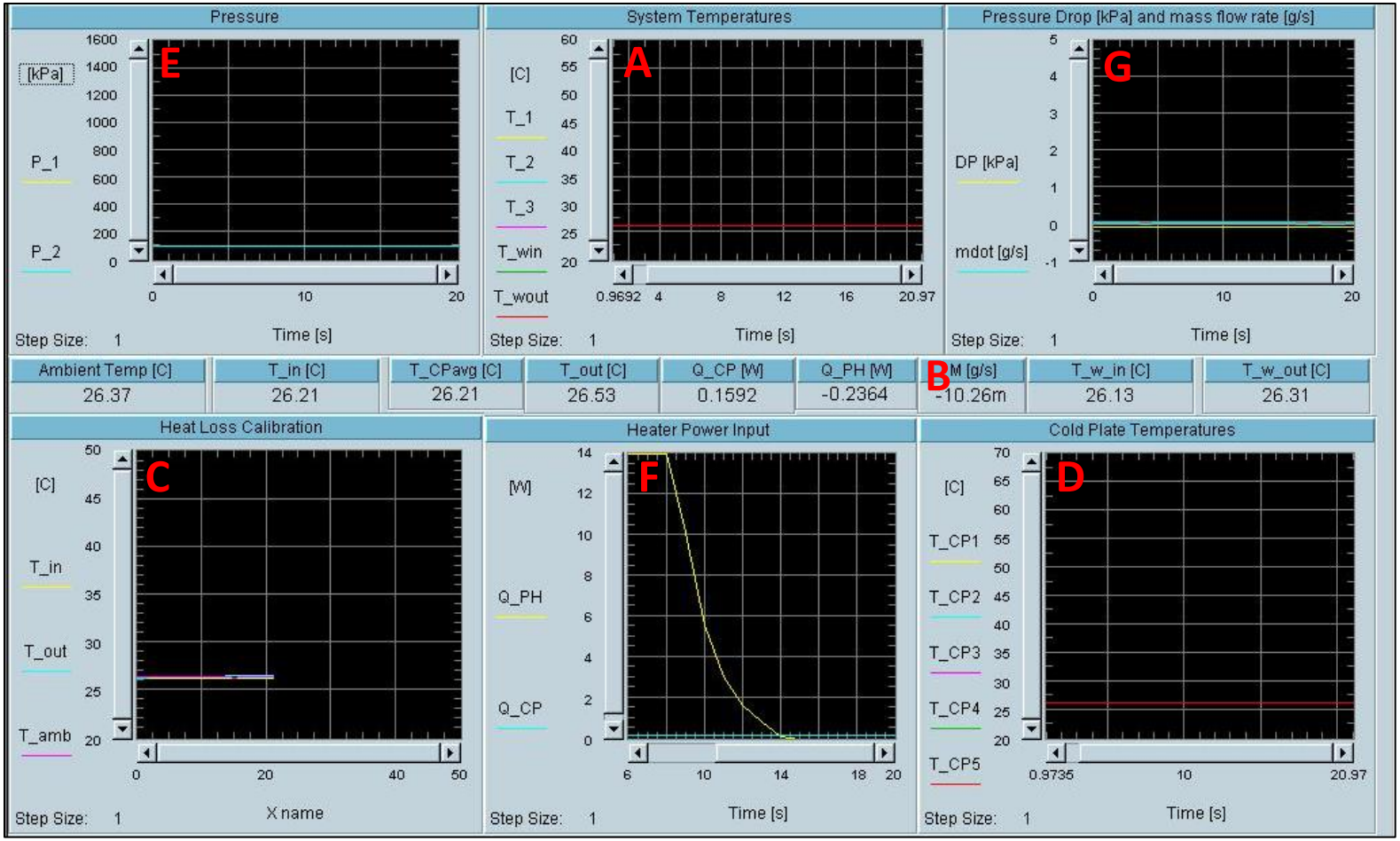

Figure 3.11: VEE feedback for system control.

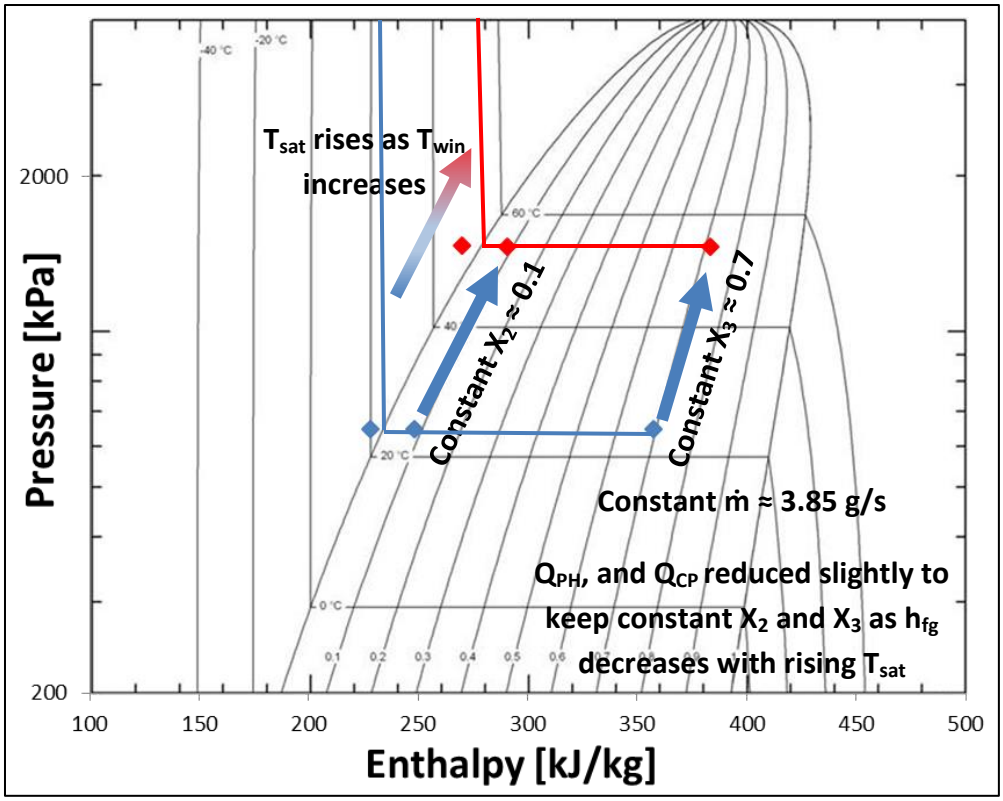

Figure 3.12: P-h diagram example for test 1.

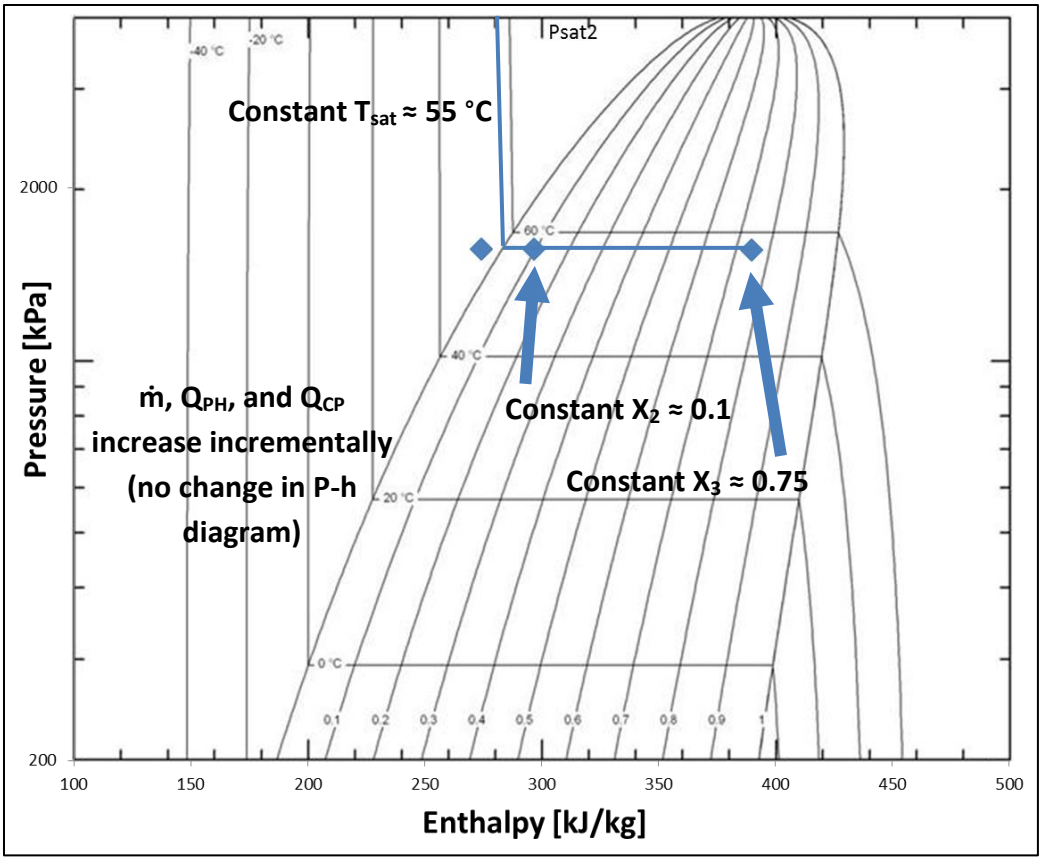

Figure 3.13: P-h diagram example for test 2.

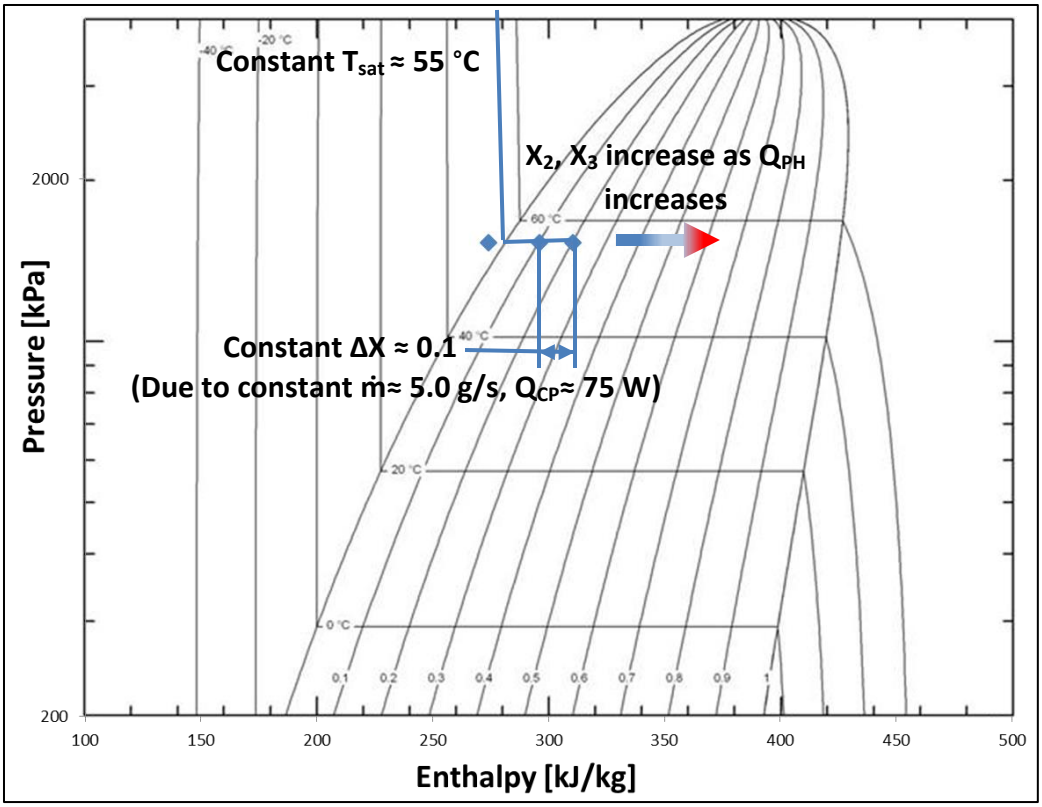

Figure 3.14: P-h diagram example for test 3.

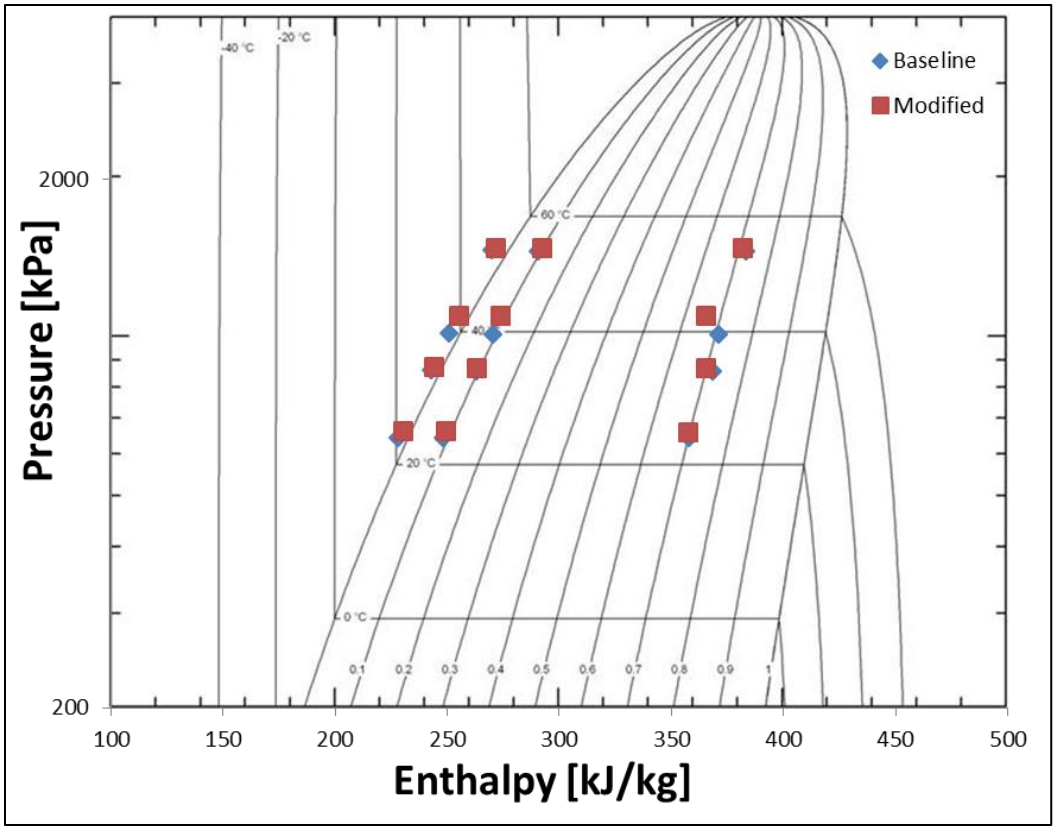

Figure 3.15: Test 1 P-h diagram.

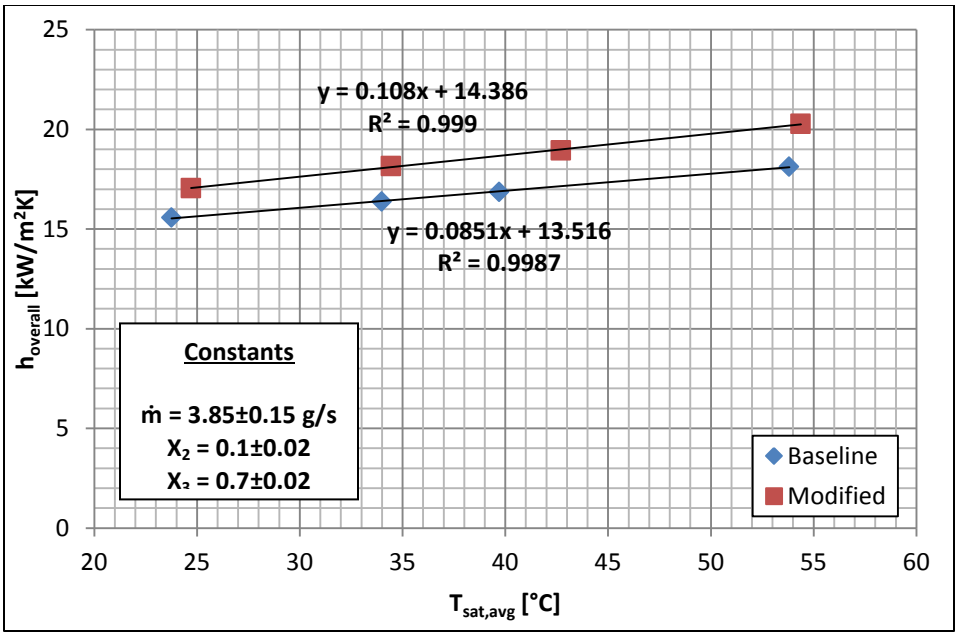

Figure 3.16: $h_{overall}$ as a function of $T_{sat,avg}$ for test 1.

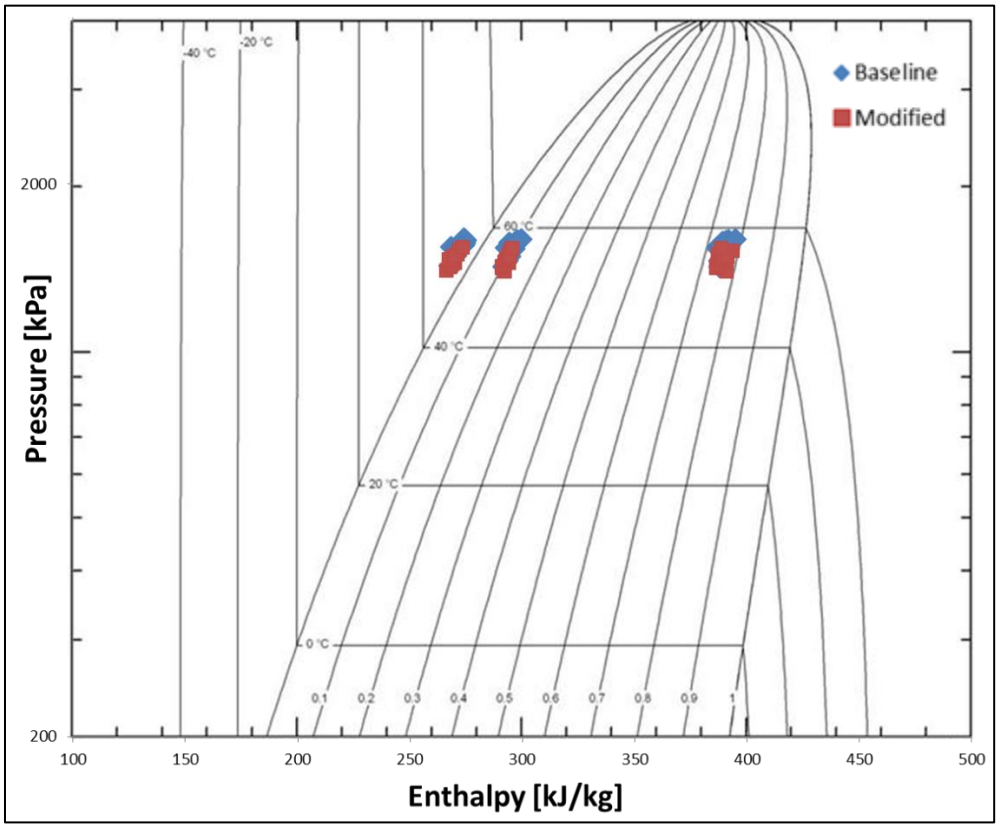

Figure 3.17: Test 2 P-h diagram.

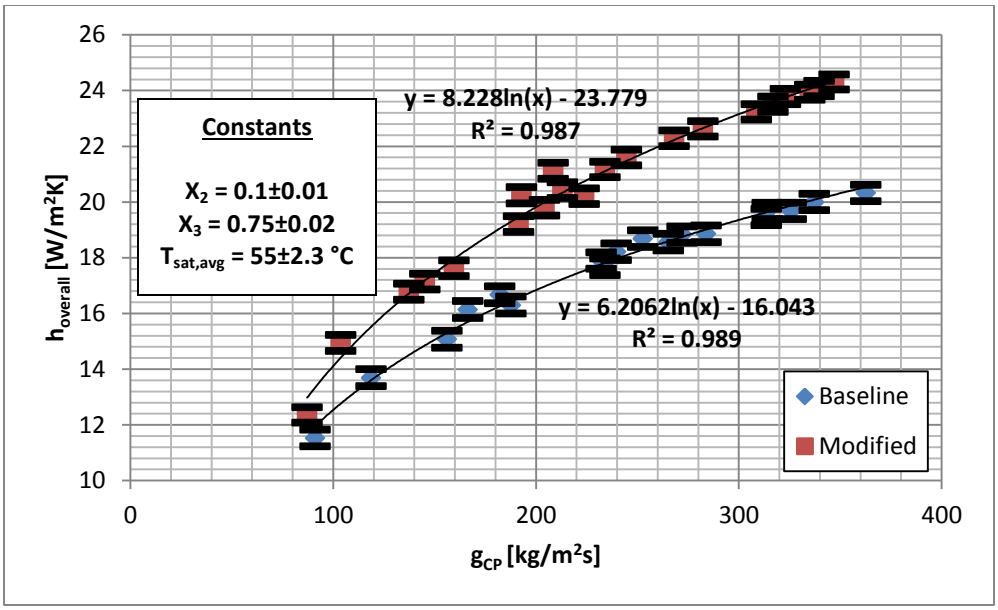

Figure 3.18: Overall heat transfer coefficient vs. mass flux.

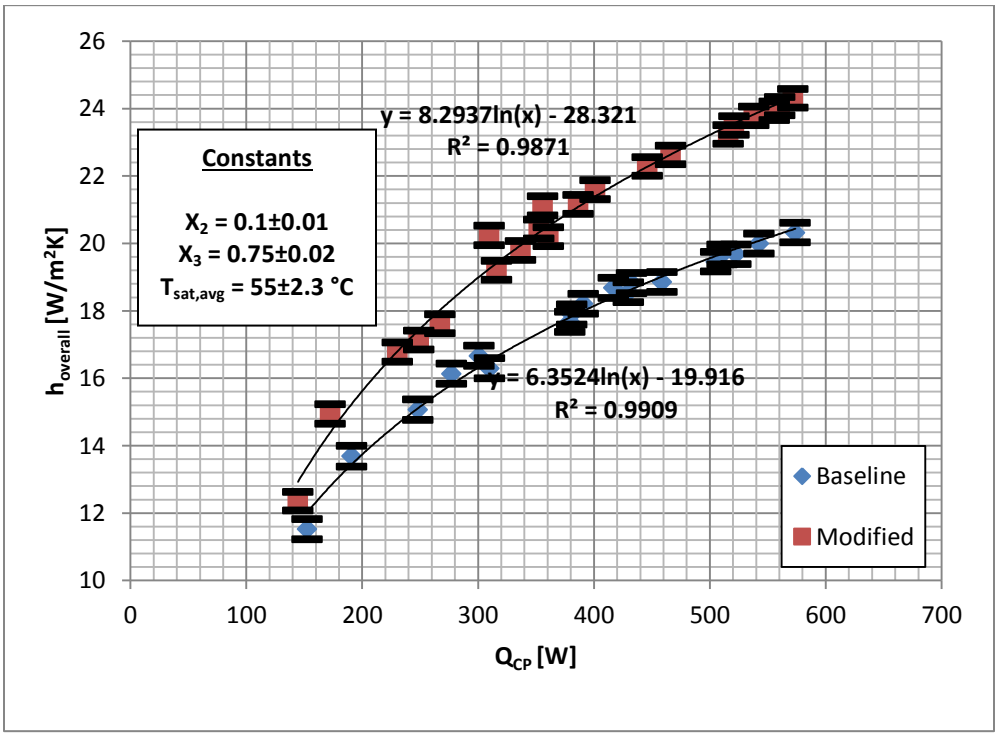

Figure 3.19: Overall heat transfer coefficient vs. cold plate power.

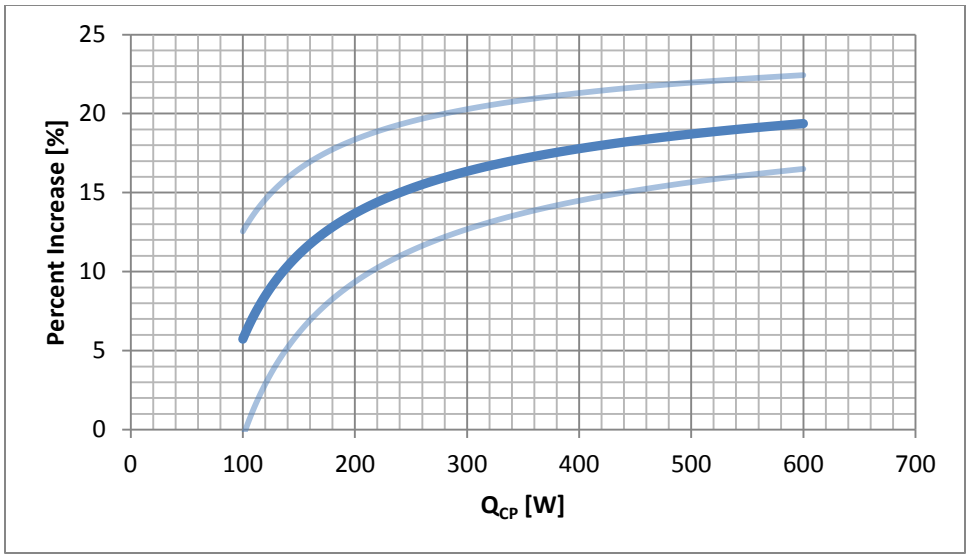

Figure 3.20: Percent increase in $h_{overall}$ with the addition of CuO surface structures.

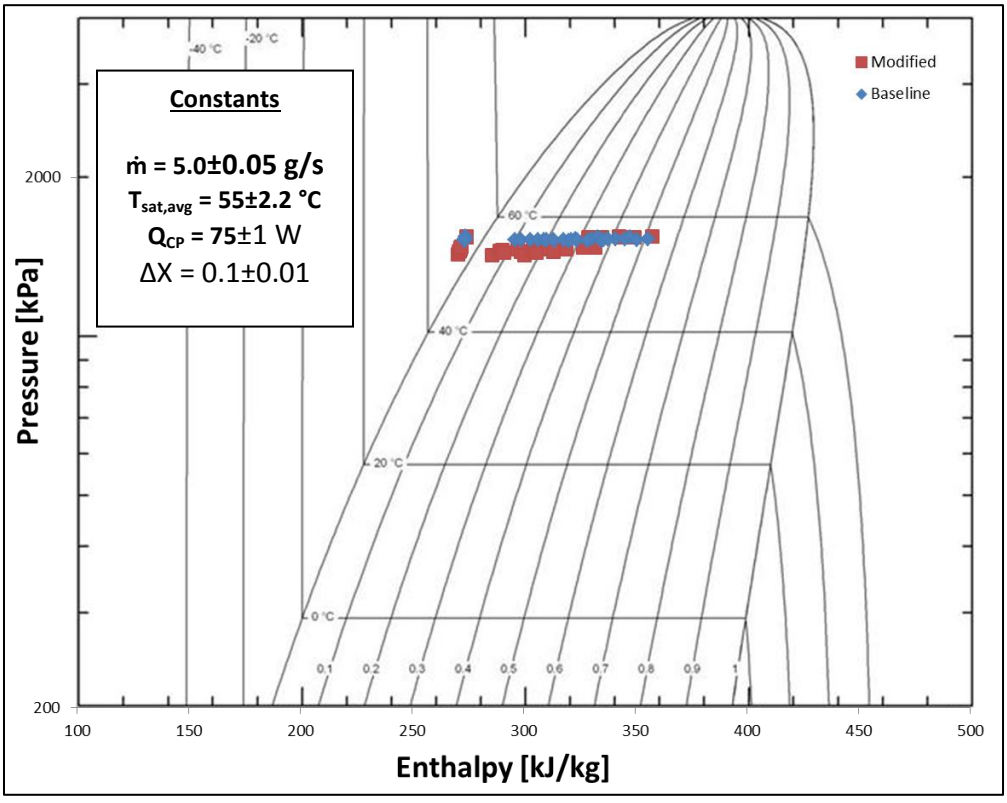

Figure 3.21: Test 3 P-h diagram.

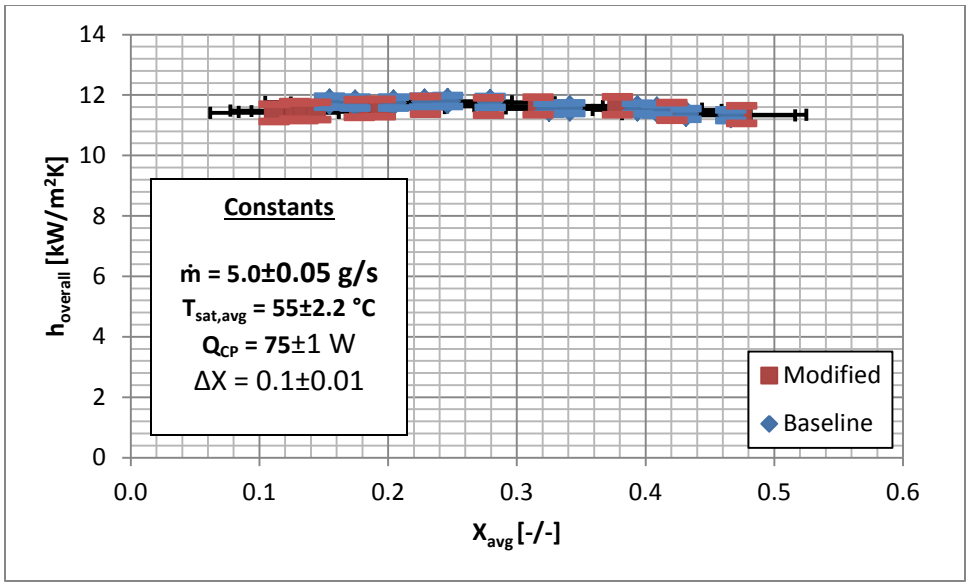

Figure 3.22: h_{local} as a function of X_{avg} for baseline and modified tests.

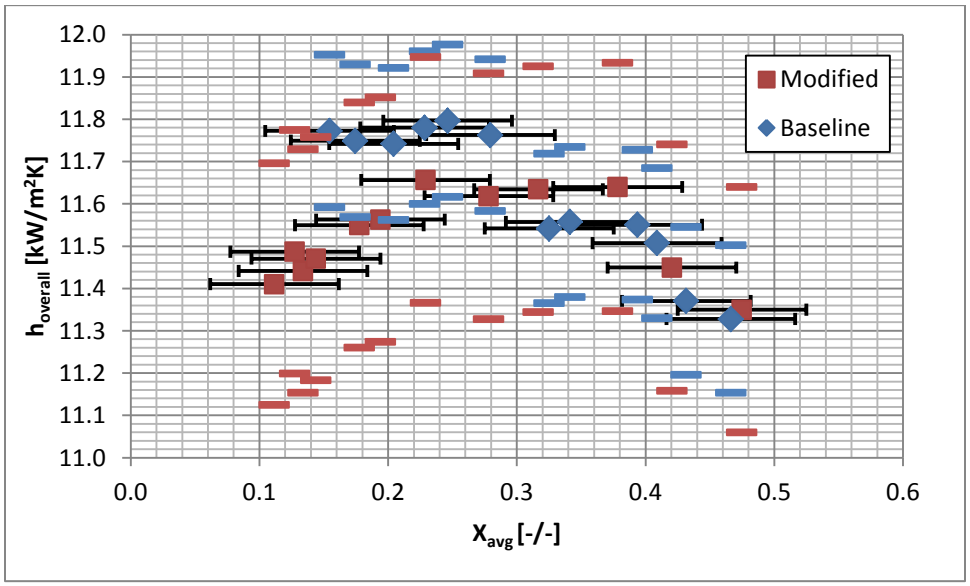

Figure 3.23: Detailed view of h_{local} vs. X_{avg}.

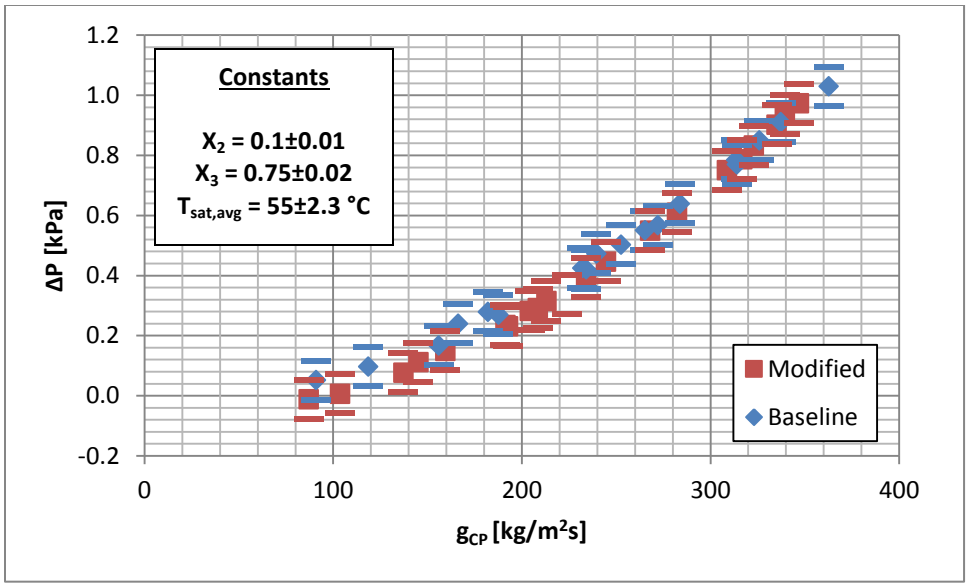

Figure 3.24: Pressure drop ΔP vs. mass flux g_{CP} for test 2.

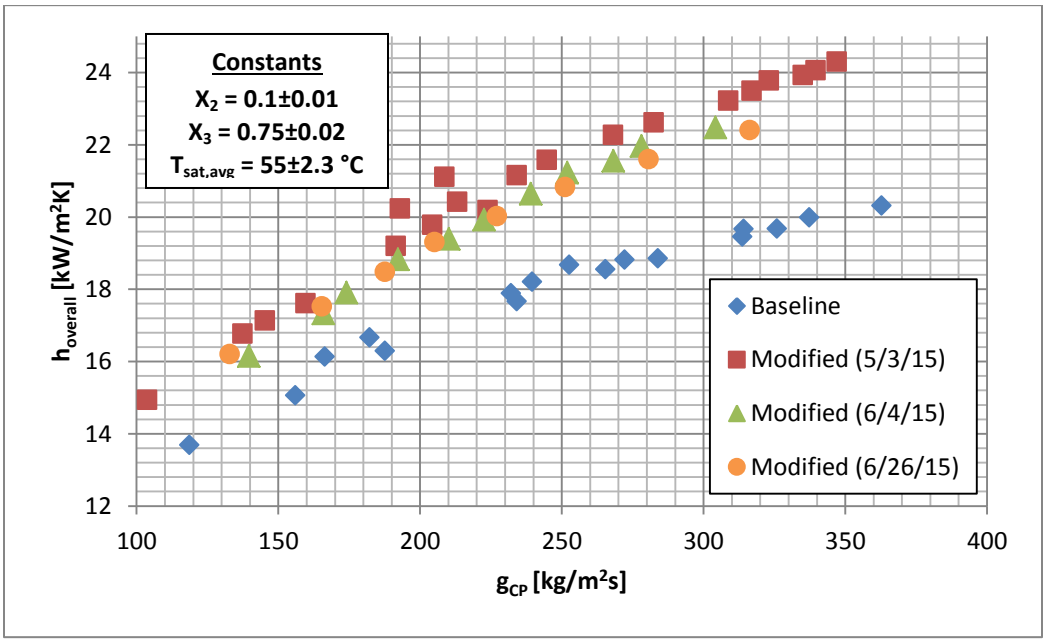

Figure 3.25: $h_{overall}$ for the modified internal surface over time.

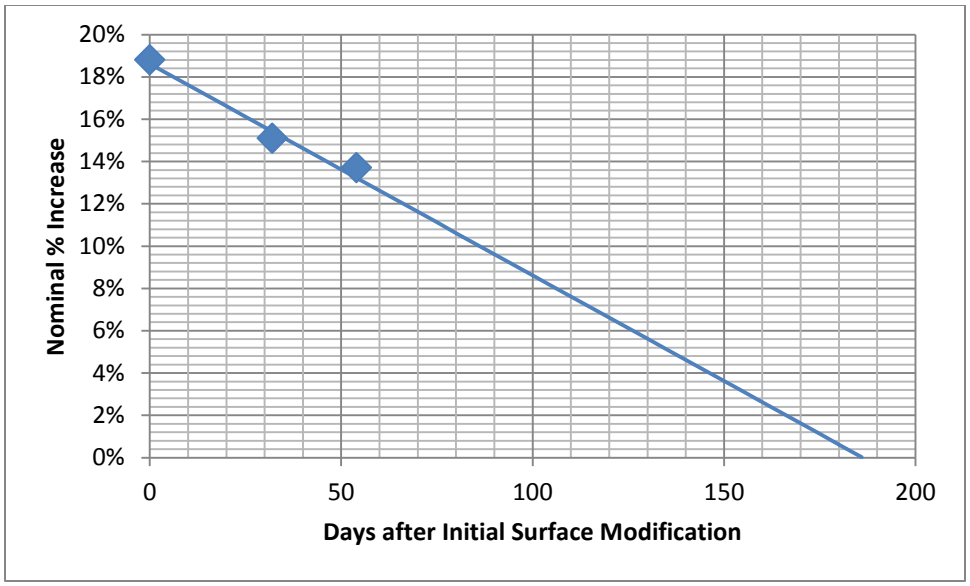

Figure 3.26: Nominal % increase over time extrapolation.

Table 3.1: Temperature Measurement List			
Symbol	TC Type	Measurement Description	Measurement Use
T_{sub}	Insertion, T-type	Measures the temperature at the subcooled condition before the preheater.	Used in conjunction with P_1 to strictly define the subcooled state.
T_{in}	Insertion, T-type	Measures the temperature at the inlet of the cold plate test section.	Used in conjunction with P_2, $\dot{m}$, and Q_{PH} to strictly define the saturated state (Temperature pressure, enthalpy, and quality) at the inlet of the cold plate test section.
T_{out}	Insertion, T-type	Measures the temperature at the outlet of the cold plate test section.	Used in conjunction with P_2, ΔP, $\dot{m}$, and Q_{CP} to strictly define the saturated state (Temperature pressure, enthalpy, and quality) at the outlet of the cold plate test section.
T_{CP1}	Wire, T-type	Each of these five thermocouples measures the centerline wall temperature of the cold plate microchannel cavities at various points along the length of the cold plate.	The wall temperature, when averaged across the cold plate, is essential for finding the average heat transfer coefficient across the cold plate.
T_{CP2}	Wire, T-type		
T_{CP3}	Wire, T-type		
T_{CP4}	Wire, T-type		
T_{CP5}	Wire, T-type		
T_{amb}	Insertion, T-type	Measures the ambient air temperature around the test facility.	Used in the calculation of thermal losses from the system to the environment.
T_{win}	Insertion, T-type	Measures the inlet water temperature on the water side of the facility.	Used in determining the saturation temperature that the system will reach at steady state; as water temperature is increased, the saturation temperature also increases.
T_{wout}	Insertion, T-type	Measures the outlet water temperature on the water side of the facility.	Used in determining if heat is flowing to or from the refrigerant in the condenser and subcooler heat exchangers.
T_{incp}	Insertion, T-type	Measures the surface temperature on the outside of the cold plate inside of the insulation.	Used in the calculation of thermal losses from the system to the environment.
T_{inph}	Wire, T-type	Measures the surface temperature on the outside of the preheater inside of the insulation.	Initially used in the calculation of thermal losses from the system to the environment.

Table 3.2: Non-temperature Measurement List				
Symbol	Device Type	Measurement Description	Measurement Use	Units
P_1	gage pressure transducer	Measures the pressure at the subcooled condition before the preheater.	Used in conjunction with T_{sub} to strictly define the subcooled state.	[kPa]
P_2	gage pressure transducer	Measures the pressure at the inlet of the cold plate test section.	Used in conjunction with T_{in}, $\dot{m}$, and Q_{PH} to strictly define the saturated state (temperature, pressure, enthalpy, and quality) at the inlet of the cold plate test section.	[kPa]
ΔP	differential pressure transducer	Measures the pressure drop across the cold plate	Used in conjunction with P_2 to define the pressure at the outlet of the cold plate, P_3. Also, it is used as a performance metric to determine the differences between the baseline and modified cold plate tests.	[kPa]
$\dot{m}$	mass flow meter	Measures the liquid mass flow rate at the exit of the micropump.	Used for all measurements to determine relative enthalpies and qualities at different points within the system.	[g/s]
Q_{PH}	insertion heater with corresponding watt transducer	Measures the power provided to the refrigerant to bring it from a subcooled liquid to two phase flow.	Used in conjunction with P_2 and T_{in} to both set and determine the inlet quality to the cold plate, X_2.	[W]
Q_{CP}	resistive heater with corresponding watt transducer	Measures the power provided to the refrigerant across the cold plate evaporator.	Used in conjunction with wall temperatures, fluid temperatures, mass flow rates, and fluid pressures to determine both the outlet quality X_3 and the combined heat transfer coefficient across the cold plate, h_{comb}.	[W]

Table 3.3: UA coefficients	
UA_{PH} [W/°C]	0.2622
UA_{CP} [W/°C]	0.1317

Table 3.4: Measurement Error		
Measurement	Error	Units
σ_{TC}	± 0.5	[°C]
σ_{P1}, σ_{P2}	± 5.0	[kPa]
$\sigma_{\Delta P}$	±0.065	[kPa]
σ_{A}	± 0.002	[cm^2]
σ_{PH}	$\pm[(1.1283*Q_{PH}^{-0.5})^2 + 0.001567]^{0.5}$	[W]
σ_{CP}	$\pm[(1.6490*Q_{CP}^{-0.5})^2 + 0.084559]^{0.5}$	[W]
$\sigma_{\dot{m}}$	± 0.05	[g/s]

CHAPTER 4: CONCLUSION

This thesis aims to explore how to improve the boiling heat transfer in a cold plate microchanneled evaporator with a surface modification. Specifically, the copper oxide surface structures used had previously only been explored for use on pure copper surfaces; not only this, but they were covered with a silicon-rich coating to create a hydrophobic surface in order to enhance condensation. This surface modification was first grown on pure copper and then characterized by SEM to verify the fabrication process. The structures were then grown on 363 brass surfaces and characterized with SEM. It was found that the same spike-like structures grew on the brass surfaces even with the presence of zinc. After being verified to grow on brass, the surface structures were then applied to the internal surface area of a brass and copper cold plate evaporator. Through extensive testing, the overall boiling heat transfer coefficient across the cold plate was characterized for the cold plate both as is for a baseline data set and with the surface modification for comparison with R134a as the refrigerant. It was found that for the range of mass flow rates and heater powers tested the heat transfer coefficient showed significant improvement, having a nominal percent increase of as high as 19.4% at the highest load condition tested. This improvement came with no significant change to the pressure drop. However, it was found that over time this improvement started to drop slightly as the surface was constantly in contact with the refrigerant, possibly causing some surface deterioration.

4.1: Future Work

Deterioration over time is of utmost importance to industry, as the improvements seen to heat transfer must have a long enough lifetime to justify the cost of applying the surface structures. With this in mind, more extensive testing over time should be explored. The percent increase in $h_{overall}$ should be considered over a longer period of time to determine the true lifetime of the surface structures when in contact with R134a. Also, to better understand the mechanisms behind the improvement in the heat transfer coefficient, visualization of the flow should be conducted in future studies. Observation of how bubbles nucleate and grow on both the baseline cold plate surface and the copper oxide surface would provide better justification for the percent increase seen in $h_{overall}$ over only making statistical observations. This can be achieved by installing a modified cold plate with a polymer cover so that the microchannels are visually exposed for observation during testing.

REFERENCES

[1] Miljkovic, N,, R. Enright, Y. Nam, K. Lopez, N. Dou, J. Sack, and E. N. Wang, "Jumping-Droplet-Enhanced Condensation on Scalable Superhydrophobic Nanostructured Surfaces," *Nano Letters Nano Lett.* 13.1 (2013): 179-87, Web.

[2] Dou, N., Condensation on Superhydrophobic Copper Oxide Nanostructures, Thesis, Massachusetts Institute of Technology, Dept. of Mechanical Engineering, 2012, PDF.

[3] Stachowiak, G. W., and A. W. Batchelor, "Chapter 10: Fundamentals of Contact between Solids," *Engineering Tribology*, 4th ed, Amsterdam: Elsevier Butterworth-Heinemann, 2014, PDF.

[4] T.R. Thomas (editor), Rough Surfaces, Longman Group Limited, 1982.

[5] "All Alicona Products for Roughness and Form Measurement," *Alicona Metrology – Surface Roughness Measurement, Form Measurement and Cutting Edge Measurement in 3D,* Web, 30 June 2015.

[6] Taylor, B. N. "Guidelines for Evaluating and Expressing the Uncertainty of NIST Measurement Results." (1994): Web. 10 July 2015.

[7] FLUKE, 2015, 717 Pressure Calibrator manual, retrieved from http://media.fluke.com/documents/717 iseng0200.pdf.

[8] Validyne, 2015, DR 800 Draft Range Transmitter manual, retrieved from http://validyne.com/ProductCatalog/8.pdf.

[9] FLUKE, 2015, 15b & 17b Multimeter manual, retrieved from http://assets.fluke.com/manuals/15b17b__umeng0400.pdf.

APPENDIX A: COPPER OXIDE SURFACE MODIFICATION DETAILS

A.1: Sample Application Process

This section serves as an overview of the work by N. Dou and Y. Nam [2] which describes the procedure used to create the copper oxide surface structures. First, a solution of deionized water, sodium chlorite ($NaClO_2$), sodium hydroxide (NaOH), and trisodium phosphate dodecahydrate ($Na_3PO_4 \cdot 12H_2O$) is prepared. The proportions should be that for every 100 mL of DI water, 3.75 g of $NaClO_2$, 5 g of NaOH, and 10 g of $Na_3PO_4 \cdot 12H_2O$ should be mixed into the solution. Any higher volume ratio of the water to chemicals can be used as needed to produce more of the solution. Then, this solution should be heated to 95 °C on a hot plate with a stirring rod to help mix the solution.

Once the solution is mixing and heating, the copper and brass samples are cleaned. First, a sonicator is used with acetone as a solvent to remove any organic compounds from the surface, after which the sample is rinsed with methanol, isopropyl alcohol, and water in that order. After drying with nitrogen, the samples are immersed in HCl for 30 seconds to remove any initial oxide layer, after which they should be rinsed with water and again dried with nitrogen. At this point, the samples are ready for the surface structure application process.

Once the prepared solution reaches 95 °C, the samples are immersed in the solution. After at least 5 minutes have passed (the longer the better), the samples visibly darken in color, indicating that the oxide layer has formed. The samples are then removed, rinsed with water, and dried with nitrogen.

A.2: Cold Plate Application Process

Since the cold plate has internal features, the process described in section A.1 must be modified since the cold plate cannot feasibly be completely immersed in the prepared solution. To coat the internal area, first the solution is prepared just as it was for the small samples. Then, the cold plate is oriented at an angle as seen in Figure 3.7. With a funnel attachment at the inlet and a spigot with a valve to control flow at the outlet, fluids can be passed through the cold plate using gravity as the driving force into the funnel and out of the spigot into a collection beaker. The same process for cleaning the surface of organic compounds and existing oxides is done but modified slightly. Instead of immersing small samples in the cleaning fluids, the fluids are passed through the internal geometry of the cold plate and collected at the outlet. Multiple passes of each fluid were used to ensure that the internal surfaces were well prepared.

Once cleaned, the internal surfaces are ready to be coated with the oxide layer. Unfortunately, there is no hot plate to keep the surface at the required 95 °C for 5

minutes to ensure proper oxide formation. However, the coating process is expected to work at lower temperatures; it simply will take longer for the layer to form at the lower temperatures. Therefore, the prepared 95 °C solution was passed through the cold plate multiple times at low flow rates for 15 minutes to ensure that the oxide layer still properly forms. To make sure that the solution does not cool too much, the cold plate heaters were kept on with Q_{CP} at approximately 25 W. This ensured that the surface was hot enough for oxides to form.

A.3: Figures

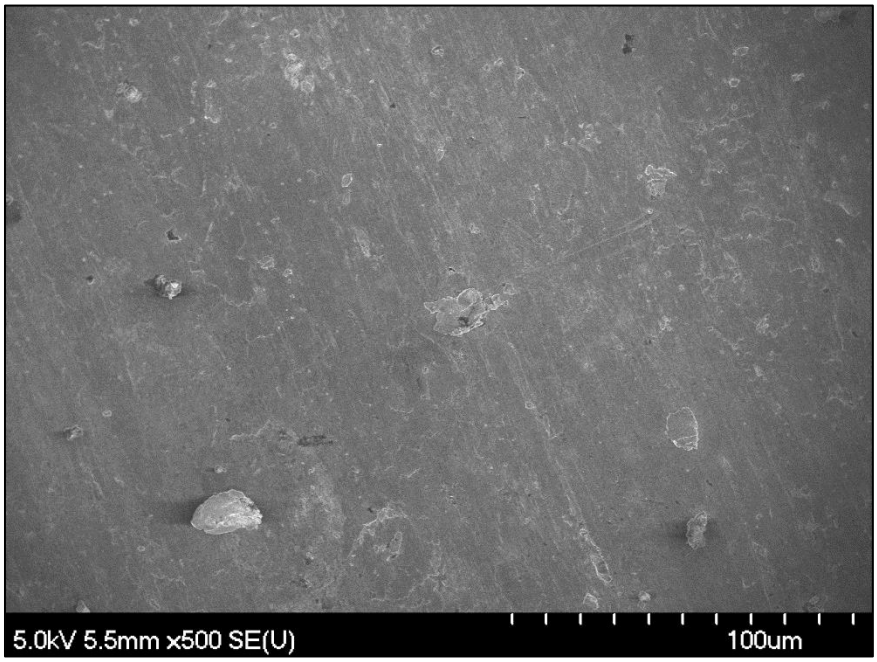

Figure A.1: Baseline copper at 500x magnification.

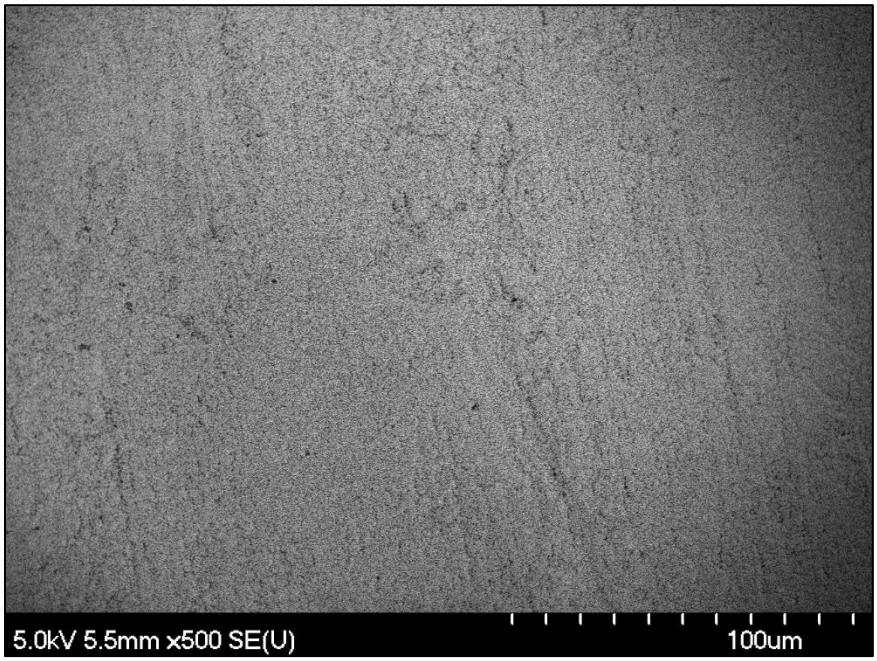

Figure A.2: Modified copper at 500x magnification.

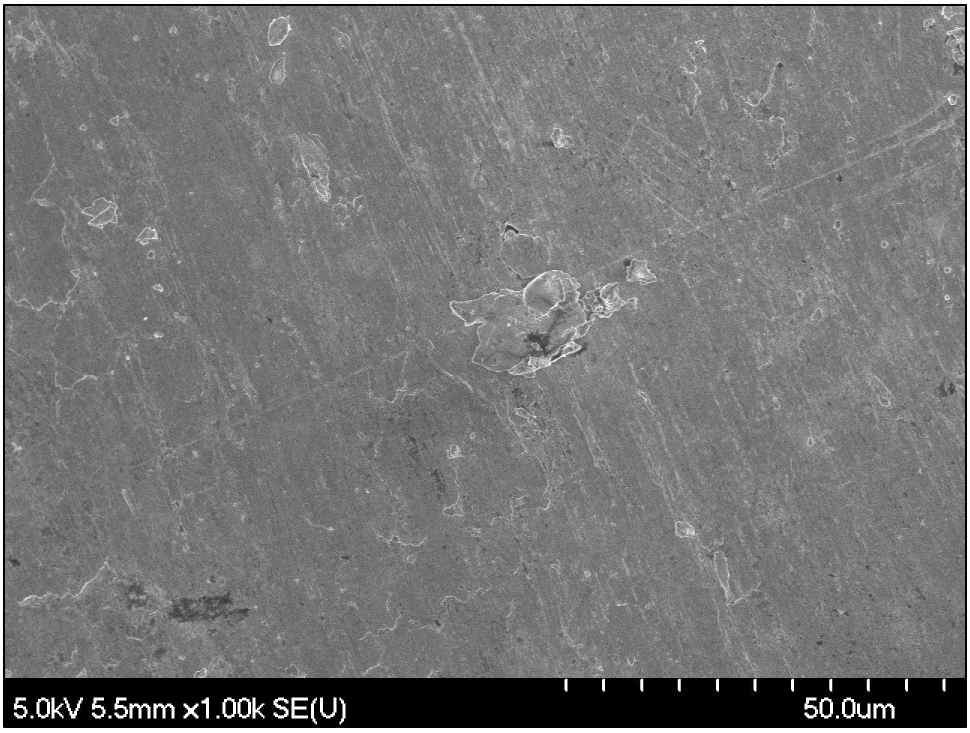

Figure A.3: Baseline copper at 1,000x magnification.

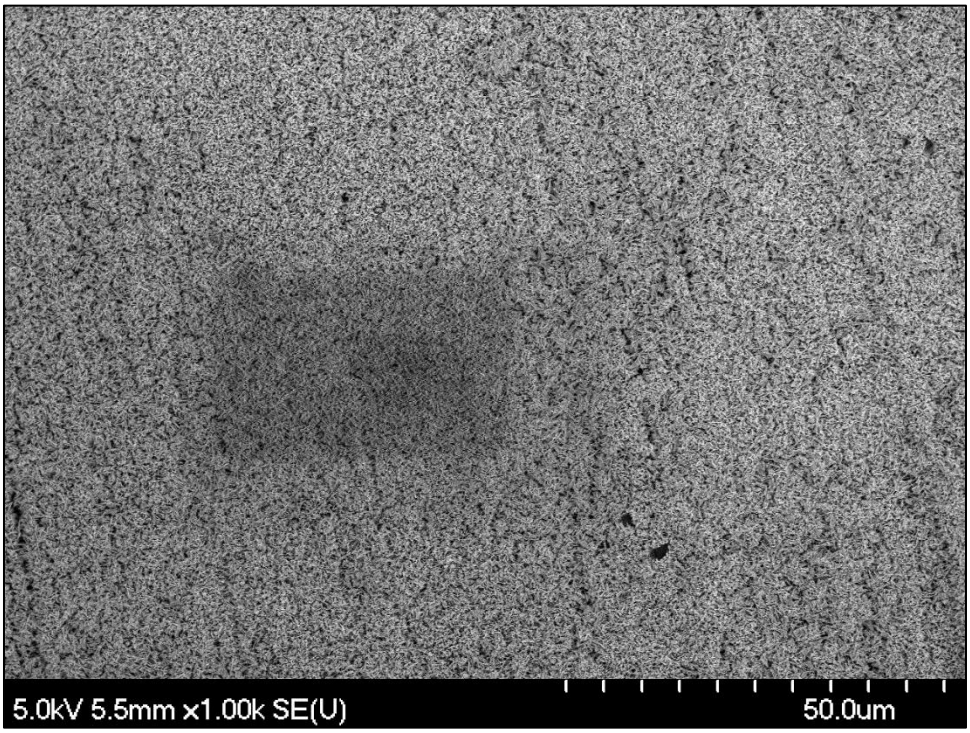

Figure A.4: Modified copper at 1,000x magnification.

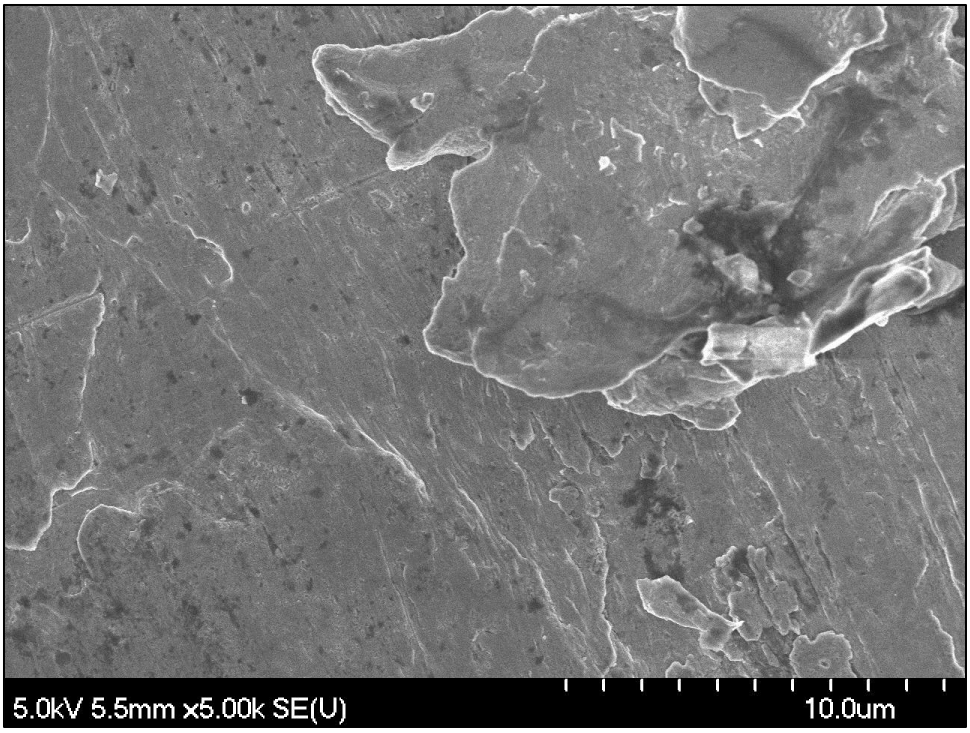

Figure A.5: Baseline copper at 5,000x magnification.

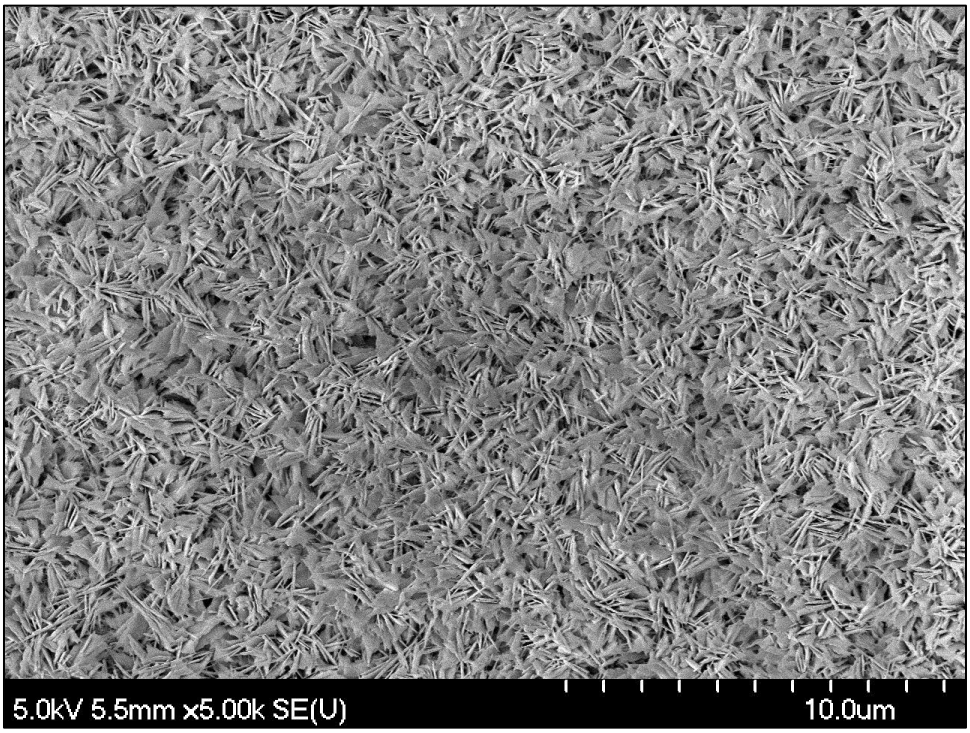

Figure A.6: Modified copper at 5,000x magnification.

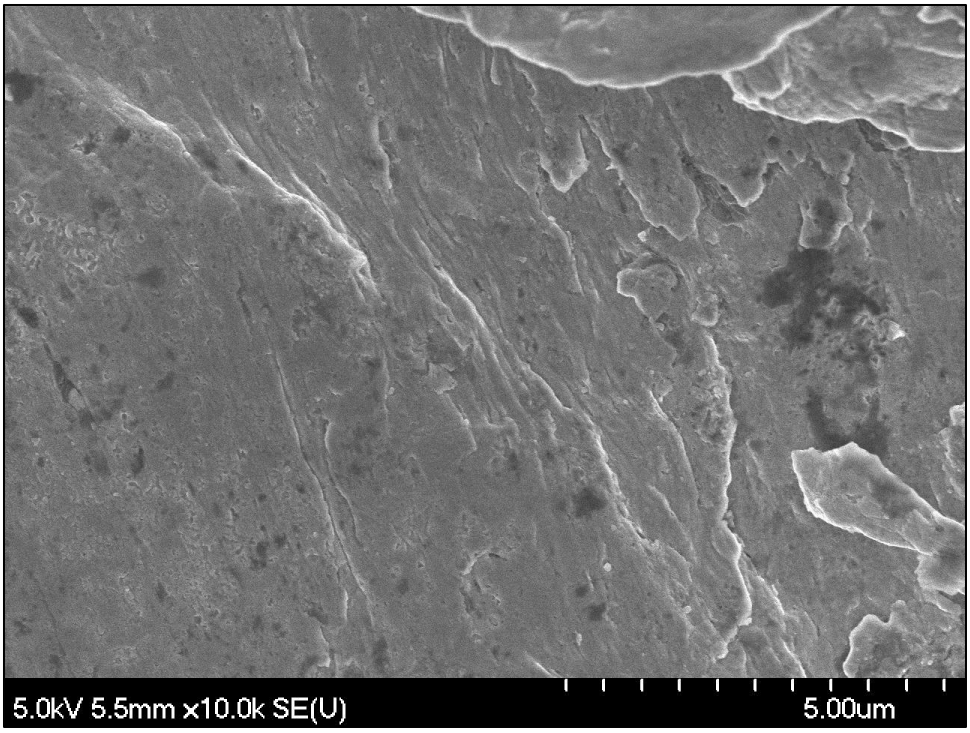

Figure A.7: Baseline copper at 10,000x magnification.

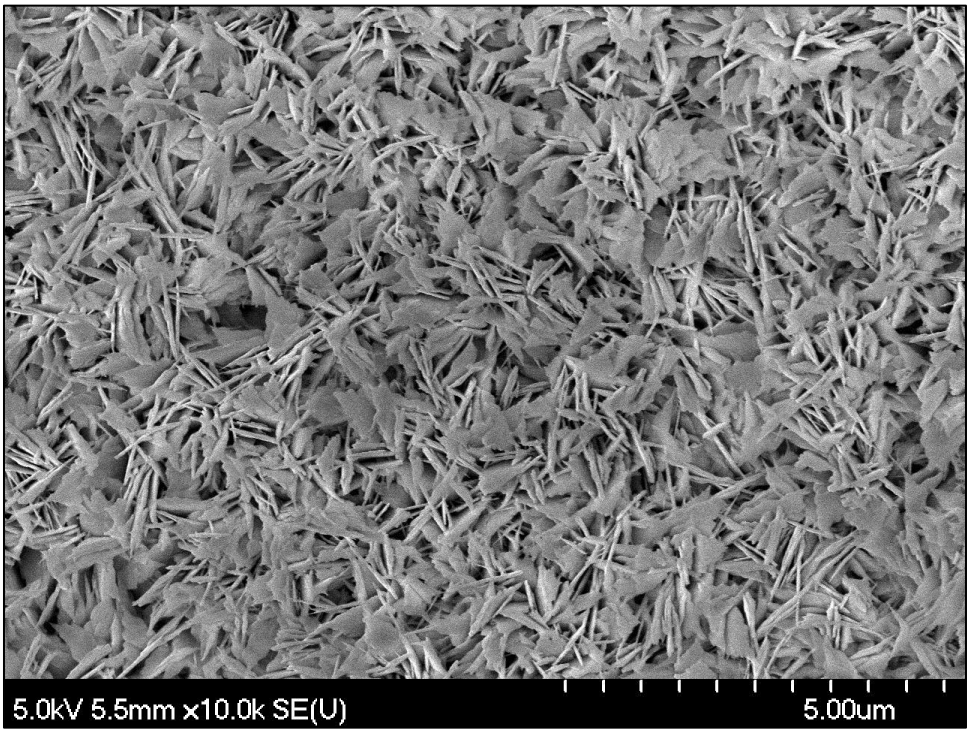

Figure A.8: Modified copper at 10,000x magnification.

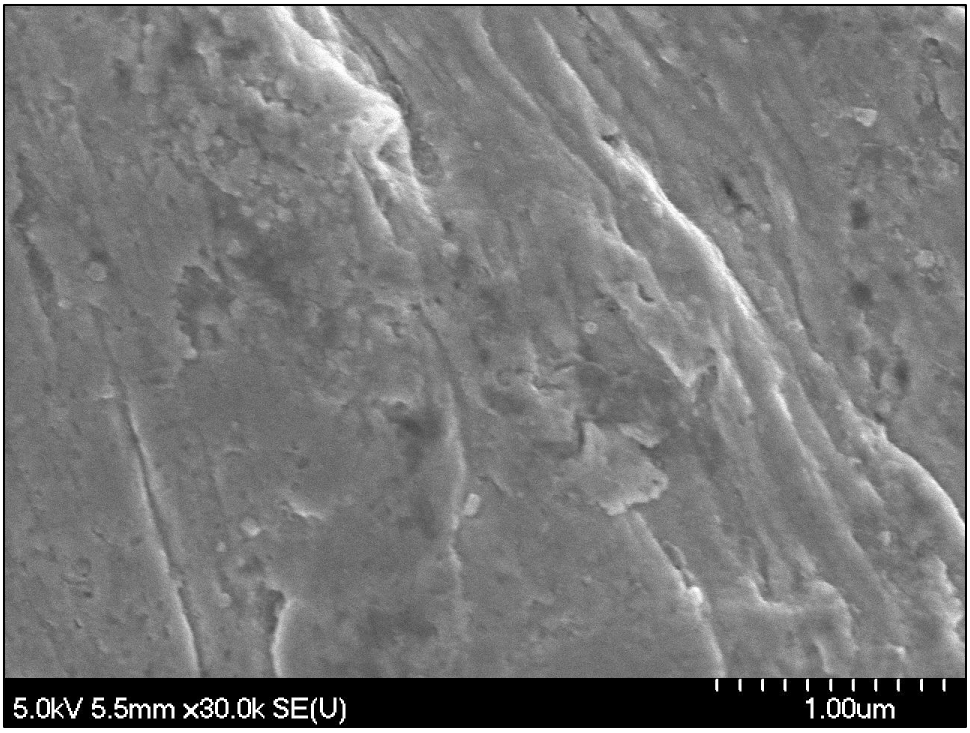

Figure A.9: Baseline copper at 30,000x magnification.

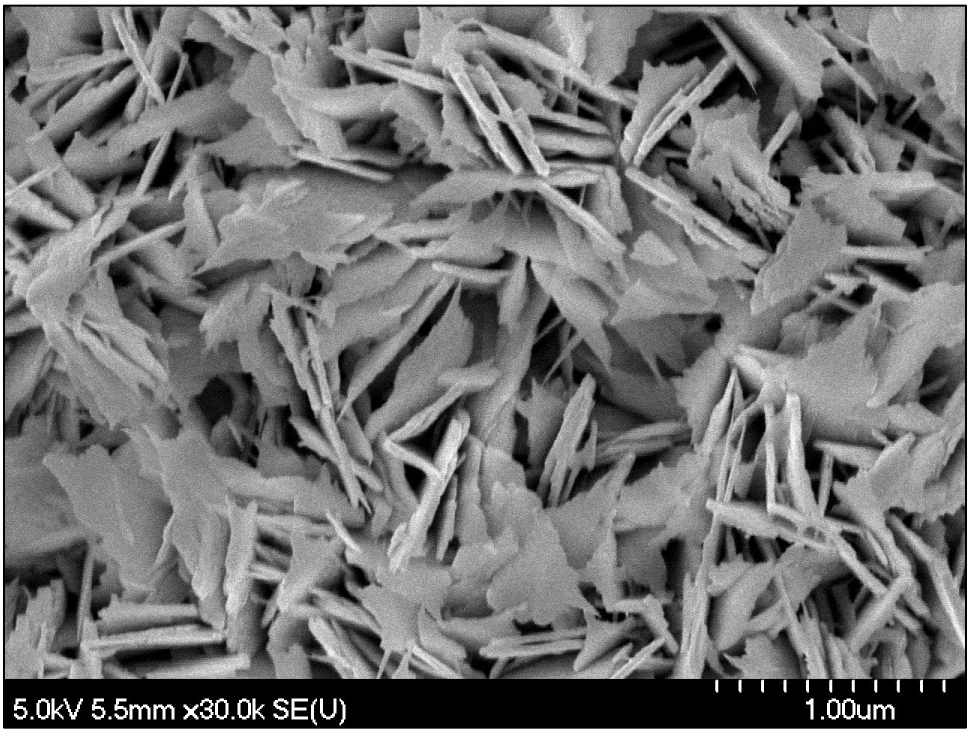

Figure A.10: Modified copper at 30,000x magnification.

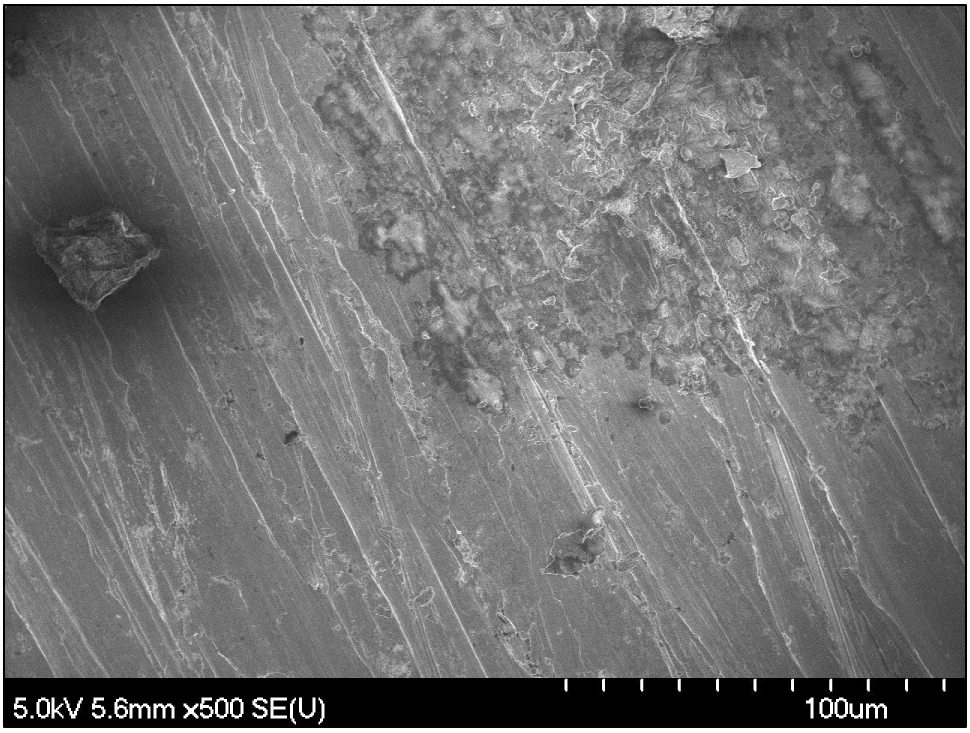

Figure A.11: Baseline brass at 500x magnification.

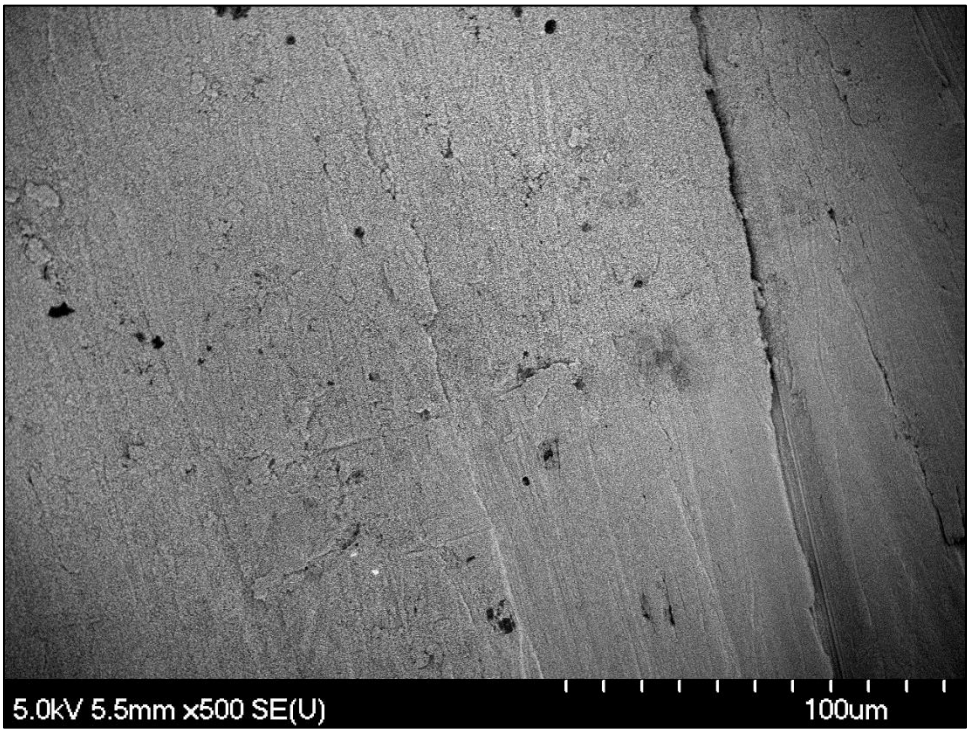

Figure A.12: Modified brass at 500x magnification.

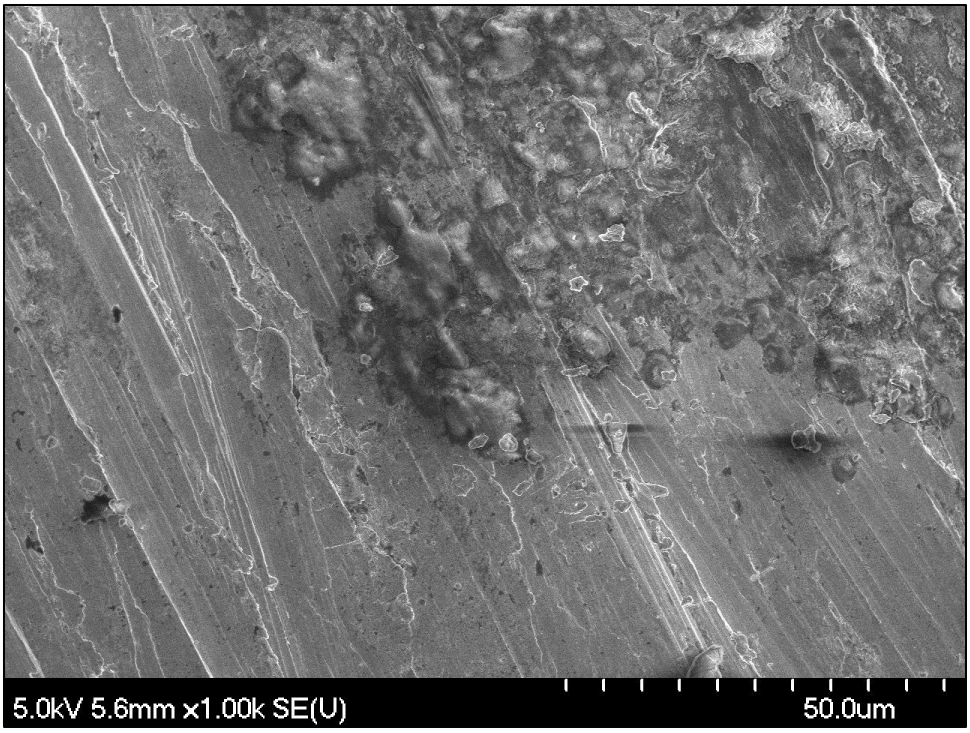

Figure A.13: Baseline brass at 1,000x magnification.

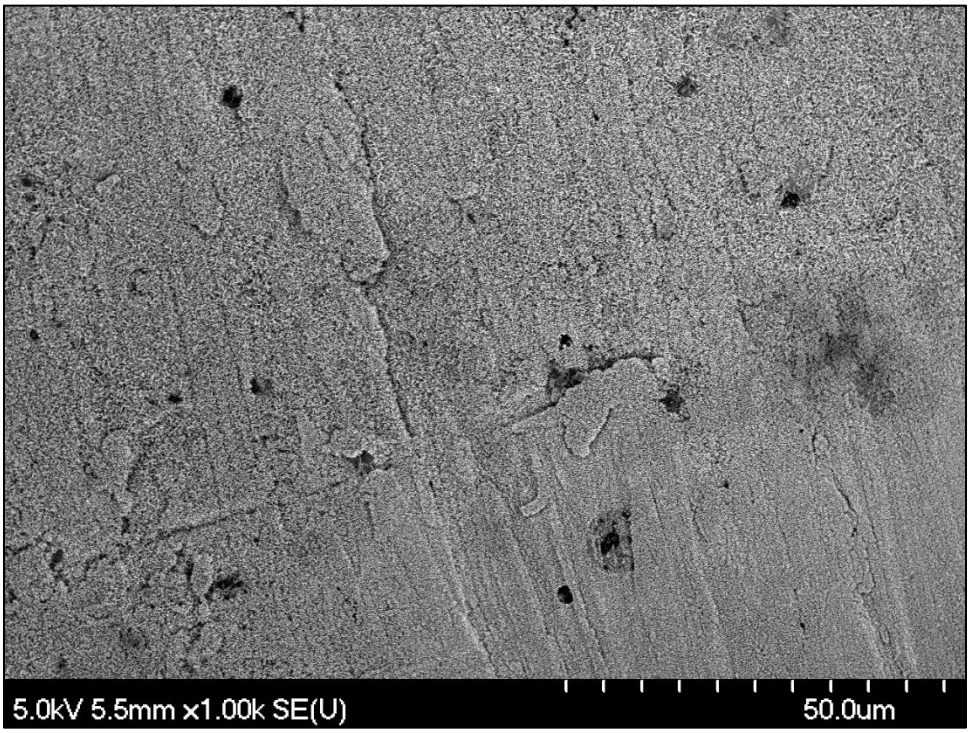

Figure A.14: Modified brass at 1,000x magnification.

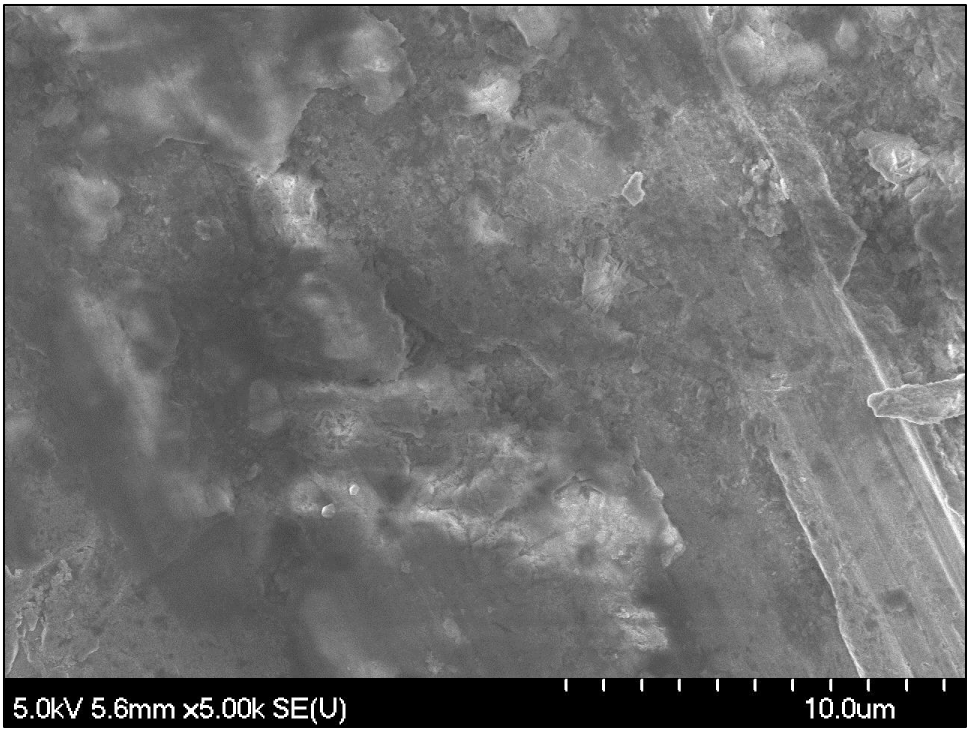

Figure A.15: Baseline brass at 5,000x magnification.

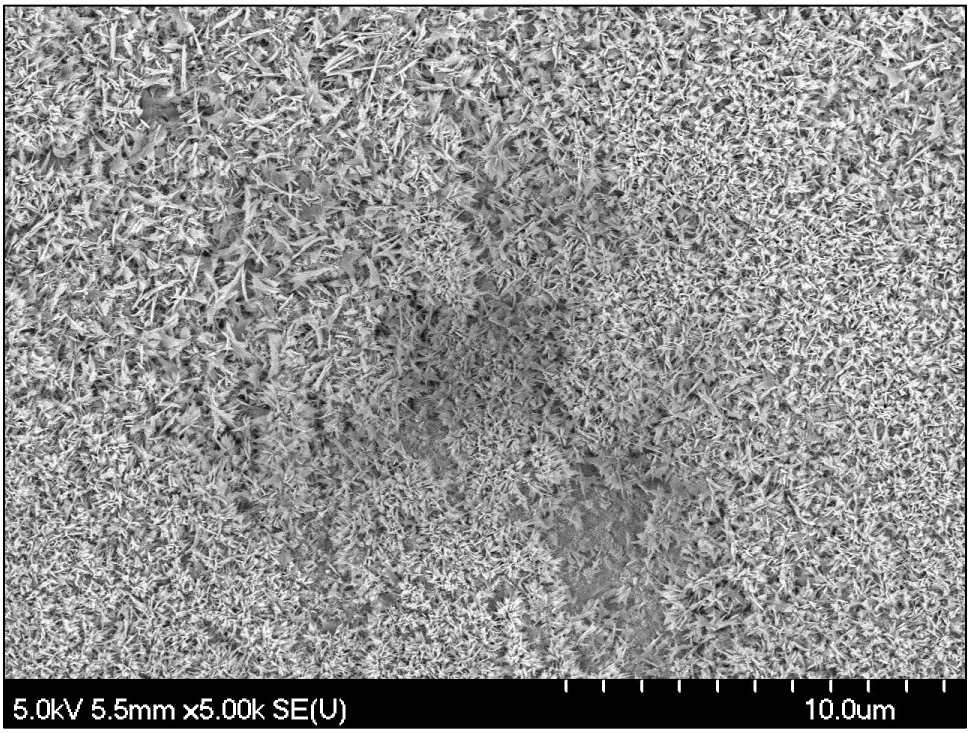

Figure A.16: Modified brass at 5,000x magnification.

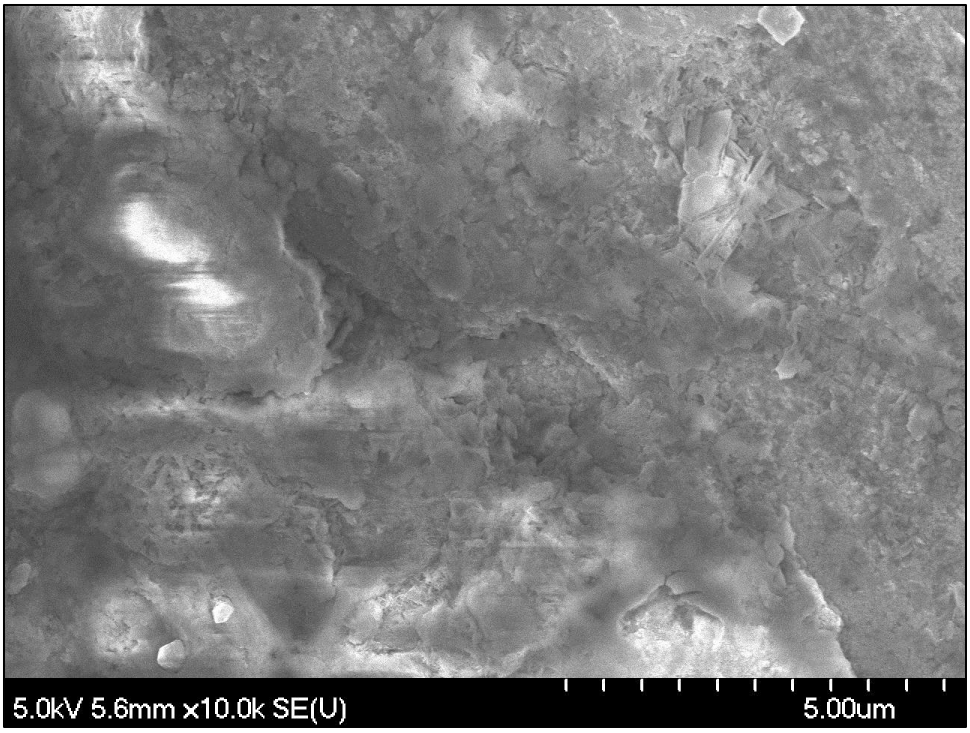

Figure A.17: Baseline brass at 10,000x magnification.

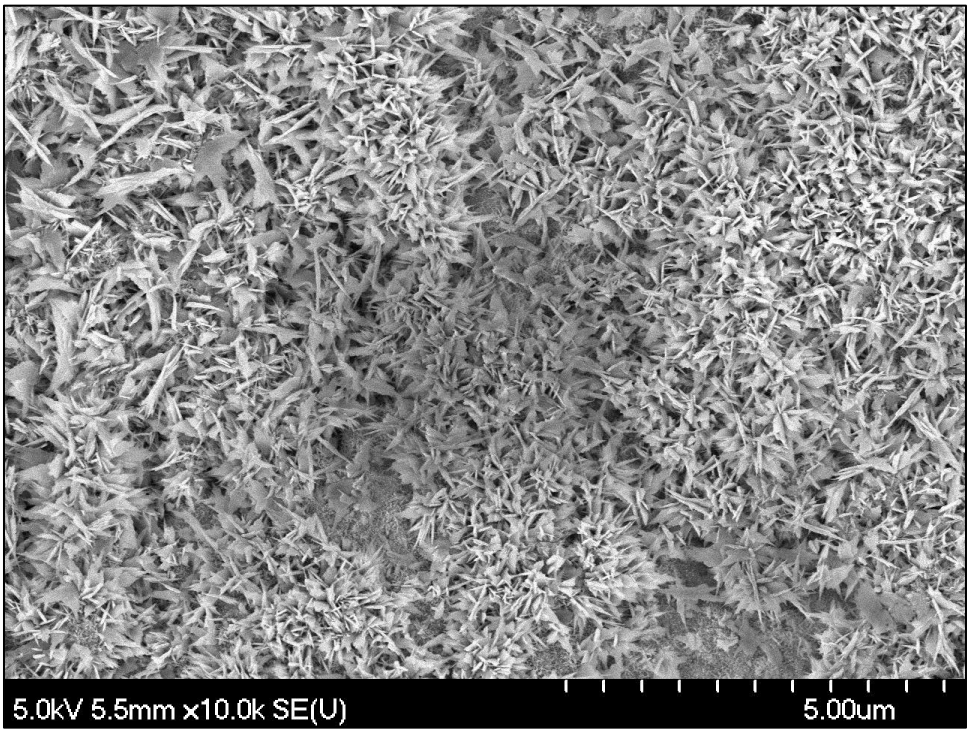

Figure A.18: Modified brass at 10,000x magnification.

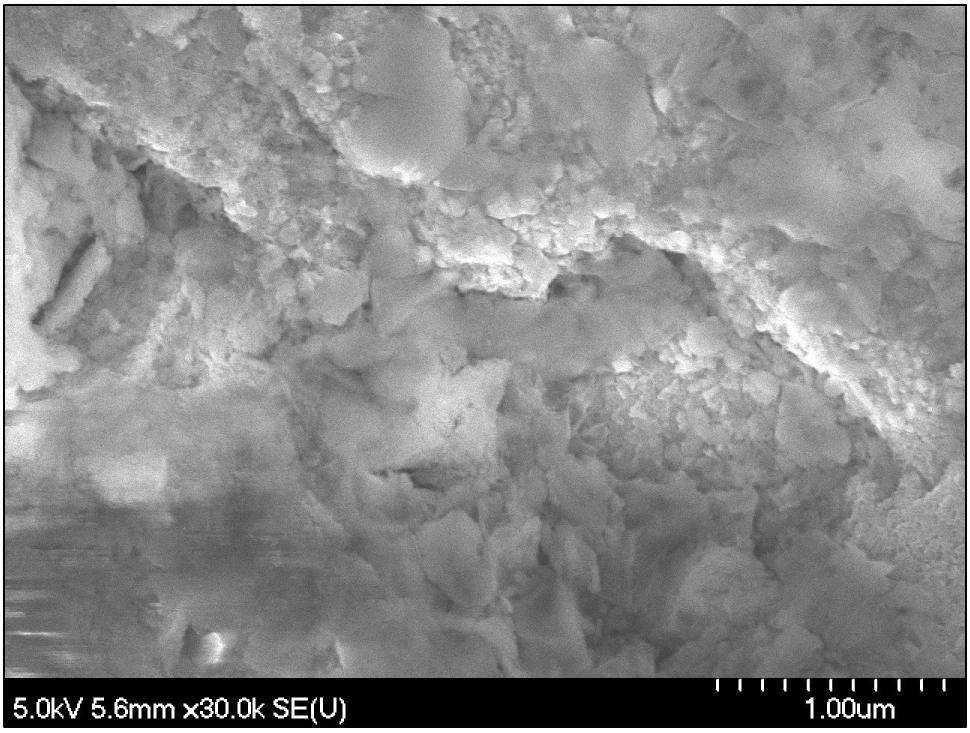

Figure A.19: Baseline brass at 30,000x magnification.

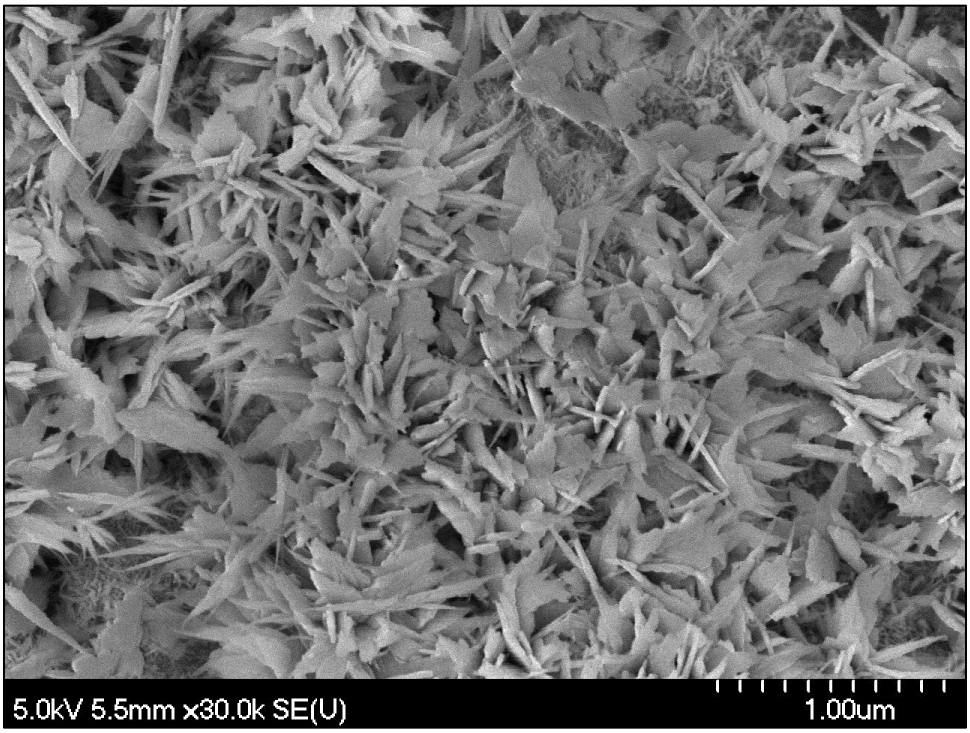

Figure A.20: Modified brass at 30,000x magnification.

APPENDIX B: CODE DEVELOPMENT DETAILS

A HP 75000 Series B data logger takes in all signals from the system. This is done with two HP E1347A 16 channel relay cards: one for all thermocouples and one for all other measurements. Then, VEE software takes the input voltage signals in 2 second increments from the system and converts them into the correct units of °C, kPa, g/s, or W as needed with the calibration data. Then, both the raw voltages and these processed signals are exported to an open Excel document that continually writes a new row of data for each data packet received every 2 seconds. The Excel file then does the rest of the work to calculate all other parameters past the initial measurements. First, it logs all voltages and measurements into separate sheets. Then, a sheet is used to calculate enthalpies, qualities, heat losses, etc. for each packet of measurements. To make some of these calculations, refrigerant properties are required. To fetch these properties, Excel references a database powered by REFPROP software that provides functions within Excel to determine refrigerant properties. Finally, a summary sheet is provided which displays in real time all measurements taken and all calculations made, along with a P-h diagram for reference during testing. This sheet (Figure 3.10), in conjunction with the feedback from the VEE software on the measurements (Figure 3.11) are then used to fine tune the set conditions for each test.

APPENDIX C: COMPONENT CALIBRATION

C.1: Thermocouple Calibration

Initially, the code development used a general, linear calibration equation for T-type thermocouples, in conjunction with a thermistor in the data logging equipment, which defined any general thermocouple temperature reading; these readings will be referred to as T_{cal}. This equation takes a voltage signal from each of the thermocouples and outputs a temperature in °C. However, this calibration introduced errors where each thermocouple reported different values while at the same temperature. In order to ensure that all of the thermocouples were not only well calibrated with low error but also well calibrated in relation to each other, all thermocouples were calibrated a second time simultaneously.

All thirteen thermocouples were removed from the test facility and grouped together with zip ties and electrical tape such that all thermocouple tips were within half an inch of each other. They were then mounted around a high precision thermometer probe. This whole assembly was then immersed into a well-controlled temperature bath. The temperature of this bath was kept constant at seven different temperatures, each for over five minutes at steady state. These temperatures ranged from 30 °C to 72 °C so that the calibration fully covers the ranges expected during testing. For each of these seven temperatures, T_{cal} for each thermocouple was averaged over the five minutes of steady state data and then re-

correlated to the average temperature reading of the high precision thermometer probe over that time. Linear curve fits were then developed for each thermocouple from these data.

Table C.1 provides all of the time averaged temperature data for all thermocouples at each of the seven calibration temperatures. Then, Table C.2 shows the resulting linear fits to transform each of the thermocouple signals based on equation (C.1) to better match reality as per the following equation.

$$T_i = m * T_{cal} + b \tag{C.1}$$

Here T_i represents each of the thirteen temperature readings.

Two further figures help to quantify how the second calibration helped to improve the accuracy. First, Figure C.1 plots ΔT_{TC} vs. T_{HAT} for all thirteen thermocouples. Here, ΔT_{TC} [°C] is the temperature difference between T_{cal} and T_{HAT}. Ideally, with perfect correlations ΔT_{TC} would be very close to 0 °C for all thermocouples, but the thermocouples are limited by their own accuracy. Figure C.2 plots $\Delta T_{TC,cal}$ vs T_{HAT}, where $\Delta T_{TC,cal}$ is the temperature difference between the recalibrated temperatures and T_{HAT}. After the thermocouples were calibrated a second time the maximum absolute value of the difference between thermocouples and high accuracy thermometer dropped from 0.35 °C in Figure D.1 to 0.12 °C in Figure C.2.

The high precision thermometer has a known error of ±0.1 °C. From Figure C.2, the thermocouples consistently read a temperature that was at most ±0.1 °C away from the high precision thermometer. This infers that the total error of the thermocouples should be ± 0.2 °C. However, it was assumed that the entire thermal bath was in 100% thermal equilibrium; considering that the bath may have slight error to it and that there may have been slight temperature variation between the thermocouples in the bath, a small safety factor will be considered and the error of all thermocouples will be assumed to be ±0.5 °C.

C.2: Pressure Transducer Calibration

C.2.1: Gage Pressure Transducer Calibration

Pressure transducers were calibrated against a FLUKE 717 500G Pressure Calibrator, as seen in Figure C.3. The system was modified for calibration by having both the FLUKE unit and a tank of nitrogen gas connected in parallel to all pressure transducers. Pressure was ranged from ~-85 kPag all the way to ~1,200 kPag; this testing range ensures that the calibration encompasses all expected working pressures during experiments. Voltage signals for P_1 and P_2 were then calibrated to the fluke gage pressure measurement over this range. Figures C.4 and C.5 show the calibration curves for P_1 and P_2, respectively.

The FLUKE unit has a known error of ±0.05 % of the units range; with a range of 3447 kPa, the FLUKE unit has ±1.75 kPa error [7]. The difference between the calibrated pressure transducer measurement and the FLUKE measurement over the range of pressure values tested, when combined with the FLUKE error, yields the error of the pressure transducer measurements—similar to the process for thermocouple calibration. Figure C.6 shows this difference over the testing range for both pressure transducers over the testing range. This shows that the relative error of the pressure transducer calibration to the FLUKE device is ± 3.25 kPa. Therefore, the total errors of P_1 and P_2 are each ±5.0 kPa. Curiously, the pressure transducers both exhibit similar linear behavior where the pressure difference (P_{cal} -P_{FLUKE}) slowly rises from negative to positive, only to jump back to negative as soon as the difference reaches near 3 kPa. This is likely due to some overcorrection factor built into the pressure transducers to prevent them from straying from the other calibrating devices.

C.2.2: Differential Pressure Transducer Calibration

Special care was taken for the differential pressure transducer calibration since the pressure drop across the cold plate is much smaller than the working pressure. At room temperature and pressure, the system was connected to an analog inclined manometer. The high side of the differential pressure transducer was connected to the system, while the low side was left unconnected so that it stayed at atmospheric pressure. Pressure was increased in the system incrementally from 0 to 5.6 inches

of water. At ambient conditions of 105 kPa atmospheric pressure and 22.5 °C, this translates to a range of 0 to ~1.3 kPa. The output voltage from the differential pressure transducer was correlated to this pressure range, and Figure C.7 shows the calibration curve for the differential pressure measurement, ΔP.

From human error, the inclined manometer could be read accurately to within 0.02 inches of water, or ±0.005 kPa. The differential pressure transducer has a guaranteed accuracy of ±0.5% of the total range of 50 inches of water, or ±0.06 kPa [8]. Therefore, after considering both unit error and calibration error, ΔP has a total error of ±0.065 kPa.

C.3: Power and Mass Flow Calibration

Q_{PH} and Q_{CP} are measured by watt transducers that communicate send a voltage signal to the data logger that corresponds to a power measurement in watts. To calibrate the signals, the two variable voltage power supplies sent a range of voltages to the cold plate heaters and the preheater. For each voltage, the voltage supplied and heater resistance was measured with a FLUKE 79 Series Multimeter as seen in Figure C.8. The power can then be calculated by the following equation from resistance and voltage.

$$Q = \frac{V^2}{R} \tag{C.2}$$

Here Q [W] is either cold plate or preheater power, V [V] is the heater voltage, and R [Ω] is the heater resistance. Figures C.9 and C.10 show the calibration curves formed from these data for the cold plate heaters and preheater, respectively.

The FLUKE Multimeter has voltage accuracy—for the 400V maximum setting used for these voltages—with error of ±4.3 V; likewise, it has resistance accuracy of ±2.3 Ω for the settings used [9]. Based on the law of propagation of uncertainty, the accuracy of the power measurements, σ_Q, can be determined by the following equation based on voltage, power, resistance, and their respective errors.

$$\sigma_Q = Q\left[\left(\frac{2\sigma_V}{V}\right)^2 + \left(\frac{\sigma_R}{R}\right)^2 - \frac{2\sigma_{V^2R}}{V^2R}\right]^{0.5} \quad \text{(C.3)}$$

Here Q is the power measurement, σ_V is the error of the voltage (4.3 V), V is the voltage measurement [V], σ_R is the error of the resistance (2.3 Ω), R is the resistance measurement [Ω], and σ_{V2R} is the covariance between voltage and resistance. From observation, σ_{V2R} = 0 since the resistance does not change over the range of voltages. Therefore, equation (C.3) can be simplified to the following equation.

$$\sigma_Q = Q\left[\left(\frac{2\sigma_V}{V}\right)^2 + \left(\frac{\sigma_R}{R}\right)^2\right]^{0.5} \quad \text{(C.4)}$$

Resistance is assumed to be constant at 58.1 Ω for the preheater and 27.2 Ω for the cold plate heaters. Manipulating equation (C.2) gives an expression for V in terms of a constant R and the heater power Q.

$$V = \sqrt{QR} \quad \text{(C.5)}$$

Therefore, after plugging in errors for resistance and voltage, the expression for V from equation (C.5), and the resistances for each heater, equations (C.6) and (C.7) derive an expression for the preheater power error and equations (C.8) and (C.9) derive an expression for the cold plate power error.

$$\sigma_{Q_{PH}} = Q_{PH}\left[\left(\frac{8.6\,V}{\sqrt{58.1\,\Omega}\sqrt{Q_{PH}}}\right)^2 + \left(\frac{2.3\,\Omega}{58.1\,\Omega}\right)^2\right]^{0.5} \tag{C.6}$$

$$\sigma_{Q_{PH}} = Q_{PH} * \left[\left(1.1283\frac{V}{\sqrt{\Omega}} * {Q_{PH}}^{-0.5}\right)^2 + 0.001567\right]^{0.5} \tag{C.7}$$

$$\sigma_{Q_{CP}} = Q_{CP}\left[\left(\frac{8.6\,V}{\sqrt{27.2\,\Omega}\sqrt{Q_{CP}}}\right)^2 + \left(\frac{2.3\,\Omega}{27.2\,\Omega}\right)^2\right]^{0.5} \tag{C.8}$$

$$\sigma_{Q_{CP}} = Q_{CP} * \left[\left(1.6490\frac{V}{\sqrt{\Omega}} * {Q_{CP}}^{-0.5}\right)^2 + 0.084559\right]^{0.5} \tag{C.9}$$

Therefore, for any given power input from either the preheater or the cold plate during testing, the error can be calculated based on equations (C.7) and (C.9).

The mass flow meter was calibrated with a HART communicator prior to being installed to the system. From this calibration, it was assumed that $\sigma_{\dot{m}} = \pm 0.05$ g/s.

C.4: Heat Loss Coefficients and Area Error

Equations (3.1) and (3.2) can be used for testing because values for UA_{PH} and UA_{CP} were found through calibration. For the preheater, the system was brought to near

vacuum so that all heater power is lost to the environment rather than to a fluid. Q_{PH} was then increased from 0 W in very small increments, allowing the temperatures to reach steady state at each point. UA_{PH} was then calculated based on the slope of plotting preheater power vs. the temperature difference. For the cold plate, a slightly different technique was used.

The system was first charged with R134a instead of being held at vacuum. Subcooled liquid was then fed to the cold plate inlet, as verified by the enthalpy determined by T_{in} and P_2. Q_{CP} was raised high enough to ensure that superheated vapor exited the cold plate outlet, as verified by the enthalpy determined by T_{out} and P_3. Then, $Q_{CP,losses}$ in equation (3.2) can be determined by the difference between Q_{CP} and the power difference between the inlet and outlet enthalpies by the following equation.

$$Q_{CP,losses} = Q_{CP} - Q_{CP^*} = Q_{CP} - * C_p * \dot{m} * (T_{out} - T_{in}) \quad \text{(C.10)}$$

Here Q_{CP^*} is the heater power as calculated by the enthalpy difference between the inlet and the outlet and C_P is the specific heat of R134a at the operating temperatures.

Area error σ_A was assumed to be small. The internal surface area was calculated based on a 3D model of the microchannels to be 33.6 cm^2. Given the typical

tolerances of traditional machining methods being ±0.1 mm, σ_A was assumed to be ±0.2 mm^2–based on applying equation (3.12) with Z = A = L^2—or ±0.002 cm^2.

C.5: Figures and Tables

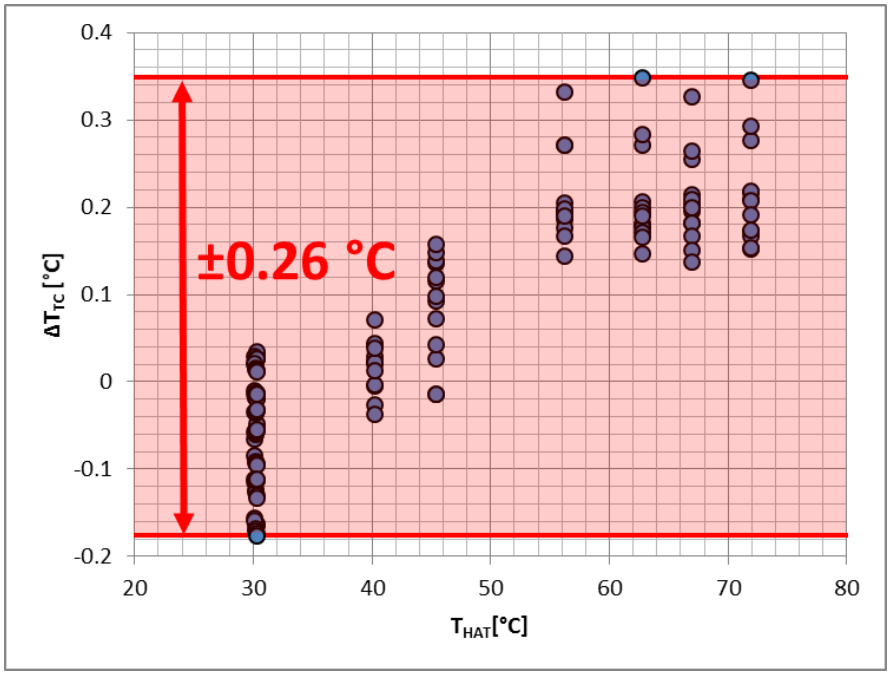

Figure C.1: Temperature difference between T_{cal} and T_{HAT}.

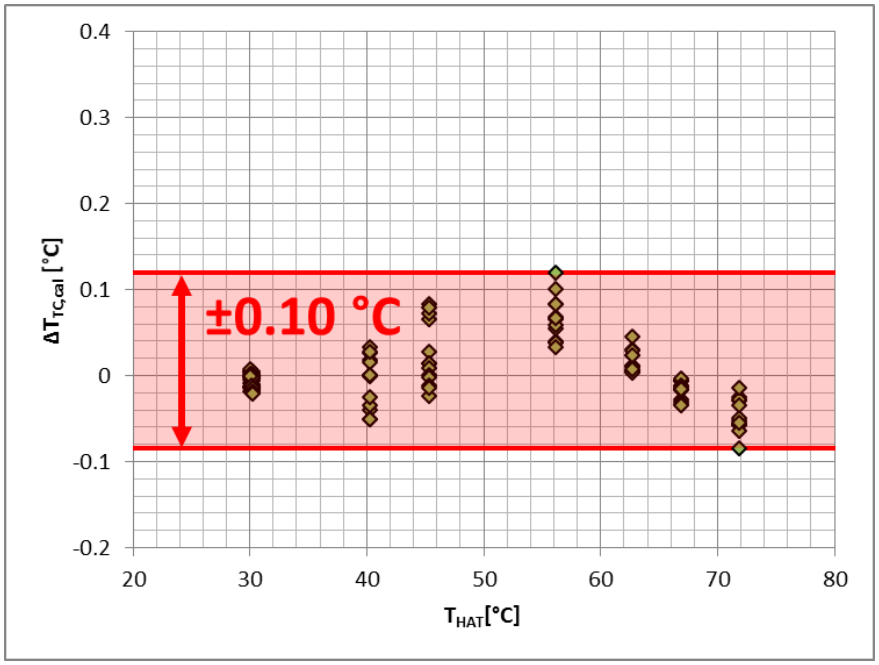

Figure C.2: Error of thermocouples after recalibration to T_{HAT}.

Figure C.3: FLUKE pressure calibration unit.

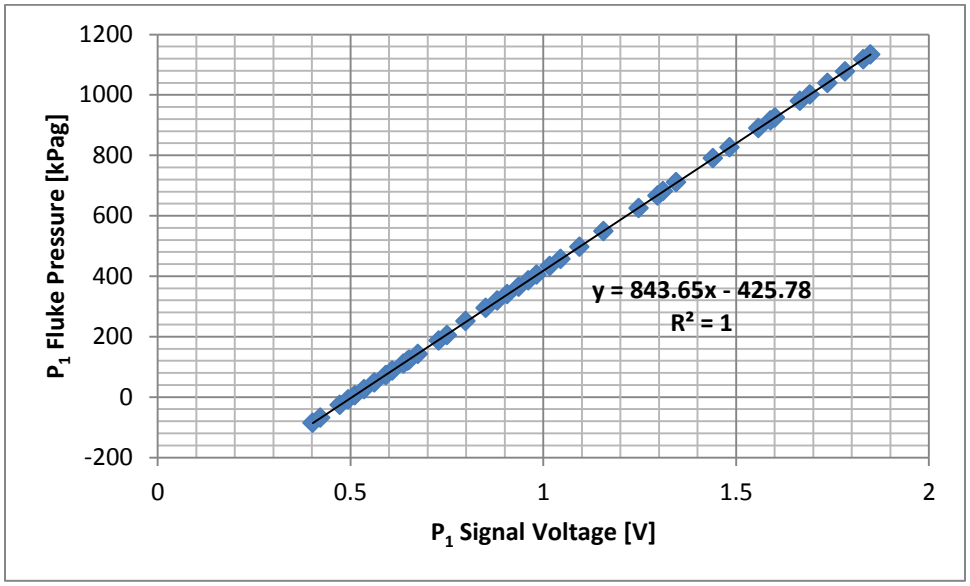

Figure C.4: P_1 calibration curve.

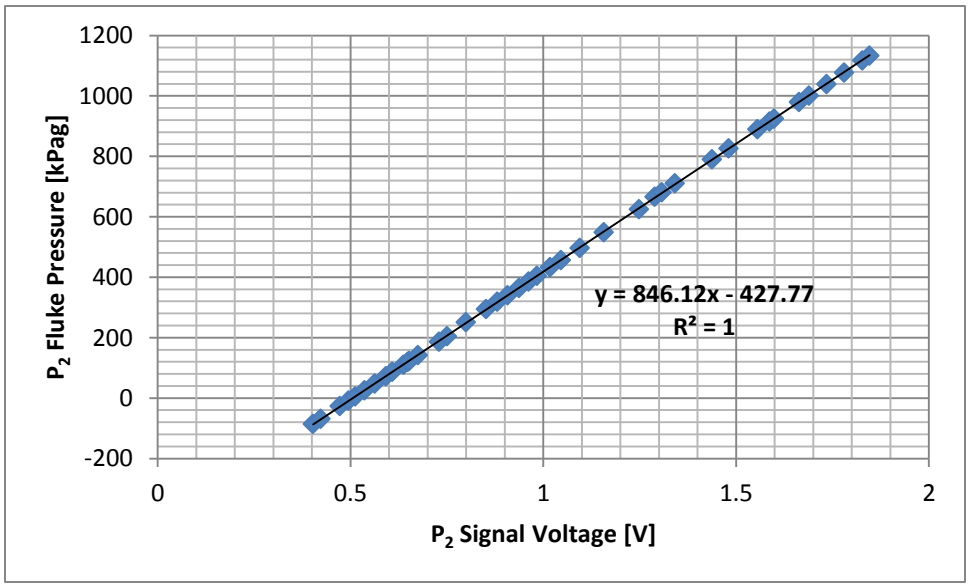

Figure C.5: P_2 calibration curve.

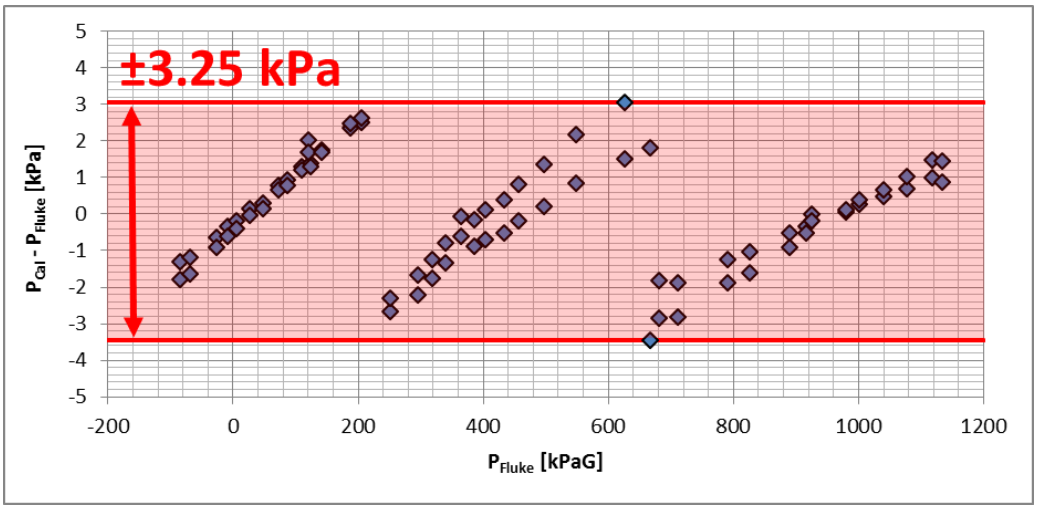

Figure C.6: Error of pressure transducers after being calibrated to P_{FLUKE}.

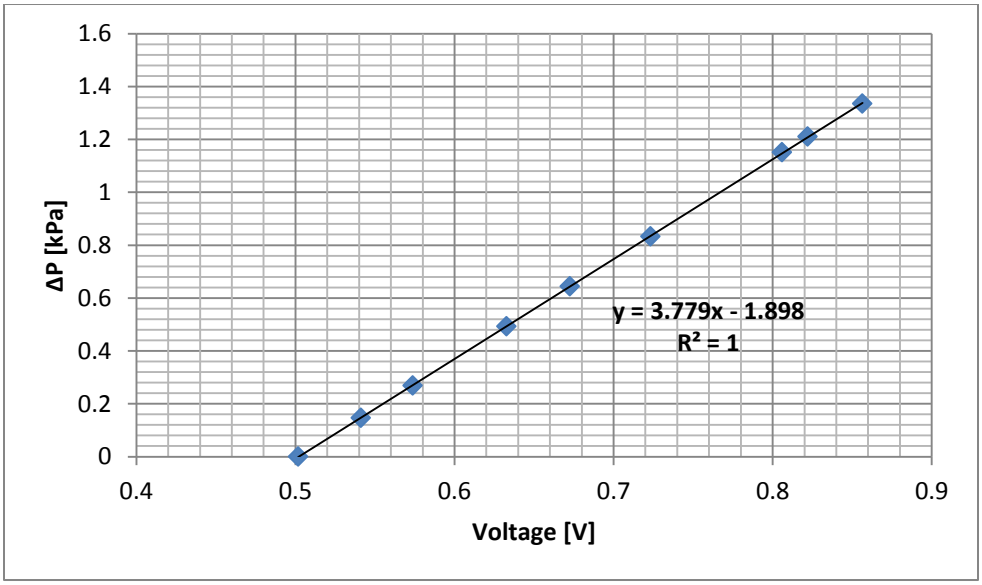

Figure C.7: Differential pressure transducer calibration curve.

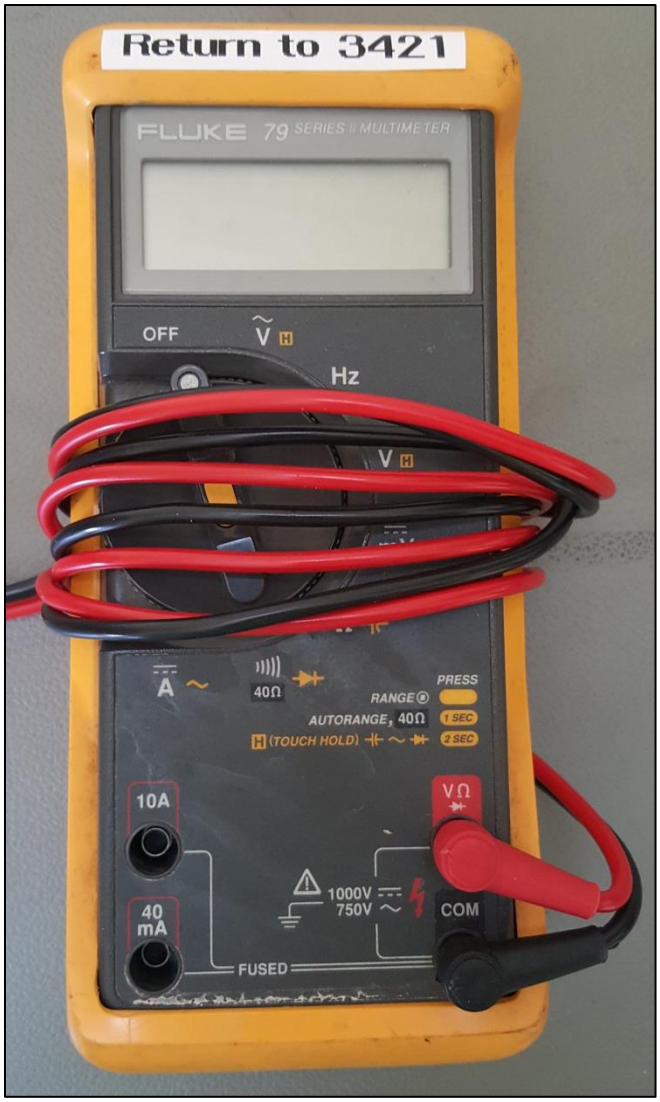

Figure C.8: FLUKE 79 Series Multimeter used for power calibration.

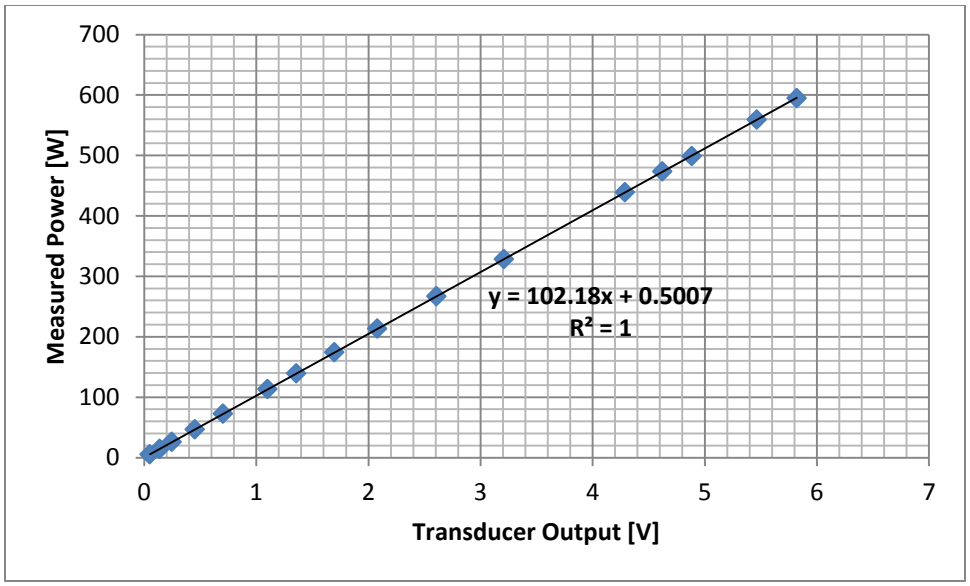

Figure C.9: Cold plate heater calibration curve.

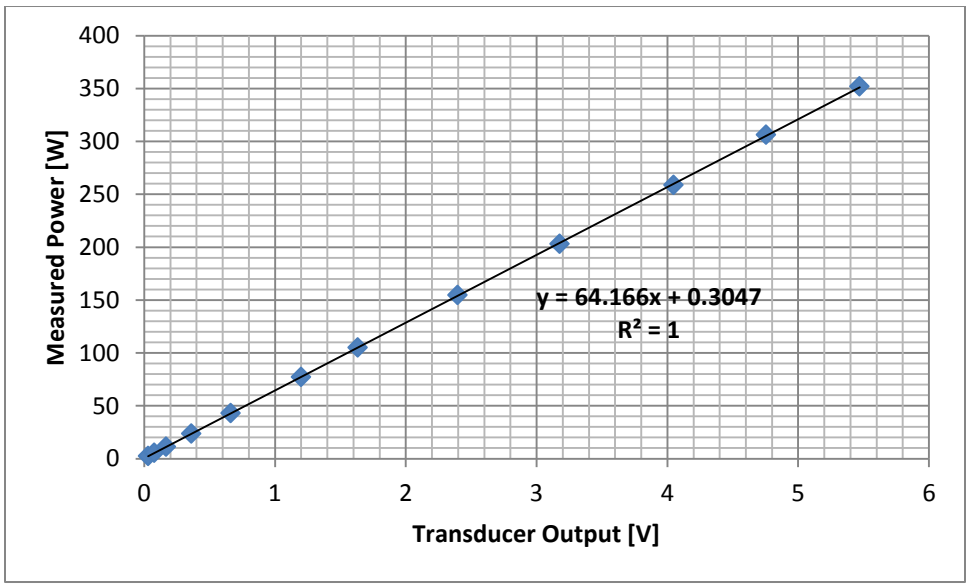

Figure C.10: Preheater calibration curve.

Table C.1: High Accuracy Thermometer Reading vs. Thermocouple Readings in a Temperature Bath							
T_{HAT} [°C]	T_{sub} [°C]	T_{in} [°C]	T_{out} [°C]	T_{water} [°C]	T_{CP1} [°C]	T_{CP2} [°C]	T_{CP3} [°C]
30.263	30.30	30.29	30.24	30.28	30.22	30.21	30.23
40.230	40.27	40.25	40.23	40.26	40.23	40.25	40.27
45.308	45.44	45.42	45.40	45.41	45.43	45.45	45.46
56.185	56.39	56.38	56.37	56.36	56.38	56.38	56.38
62.707	62.91	62.91	62.90	62.89	62.89	62.88	62.90
66.919	67.13	67.12	67.13	67.11	67.10	67.10	67.12
71.860	72.08	72.07	72.08	72.07	72.03	72.03	72.05
T_{HAT} [°C]	T_{CP4} [°C]	T_{CP5} [°C]	T_{amb} [°C]	T_{incp} [°C]	T_{inph} [°C]	T_{wout} [°C]	
30.263	30.25	30.10	30.13	30.17	30.15	30.09	
40.230	40.30	40.20	40.25	40.27	40.19	40.24	
45.308	45.47	45.29	45.34	45.38	45.30	45.35	
56.185	56.38	56.35	56.46	56.46	56.33	56.52	
62.707	62.88	62.87	62.98	62.99	62.85	63.06	
66.919	67.09	67.07	67.17	67.18	67.06	67.25	
71.860	72.01	72.03	72.14	72.15	72.01	72.21	

Table C.2: Temperature Calibration Curves for All Thermocouples (all R^2 values = 1)							
	T_{sub}	T_{in}	T_{out}	T_{win}	T_{CP1}	T_{CP2}	T_{CP3}
m [-/-]	0.9948	0.995	0.9937	0.995	0.9934	0.9936	0.9937
b [°C]	0.1273	0.1255	0.2078	0.1374	0.2445	0.2354	0.21
	T_{CP4}	T_{CP5}	T_{amb}	T_{incp}	T_{inph}	T_{wout}	
m [-/-]	0.9951	0.9911	0.9892	0.9898	0.9929	0.9861	
b [°C]	0.1436	0.4171	0.4388	0.3874	0.3226	0.5727	

APPENDIX D: ALL DATA FROM EXPERIMENTS

Table D.1: Test 1 Measurement Data

File Name	Trial #	T_{sub} [°C]	T_{in} [°C]	T_{out} [°C]	T_{CP1} [°C]	T_{CP2} [°C]	T_{CP3} [°C]	T_{CP4} [°C]	T_{CP5} [°C]	T_{CPavg} [°C]	T_{amb} [°C]	T_{win} [°C]
Tsat 24p4.xls	Base 1	20.5	23.1	23.7	32.9	31.5	30.9	32.6	31.6	31.9	27.1	19.8
Tsat 34p4.xls	Base 2	30.8	33.5	34.0	42.2	40.9	40.4	42.1	41.1	41.3	28.5	31.2
Tsat 40p2.xls	Base 3	36.1	39.2	39.7	47.4	46.1	45.6	47.2	46.2	46.5	29.6	36.9
Tsat 54p9.xls	Base 4	48.9	53.2	53.7	60.4	59.3	58.9	60.4	59.3	59.6	31.6	51.1
Tsat 25p3.xls	Mod. 1	21.9	24.0	24.6	32.3	31.7	31.2	33.0	32.5	32.1	28.1	21.2
Tsat 34p9.xls	Mod. 2	31.3	33.8	34.4	41.4	40.7	40.3	42.0	41.4	41.2	29.6	31.4
Tsat 42p9.xls	Mod. 3	39.1	42.1	42.6	48.7	48.1	47.7	49.2	48.6	48.5	30.9	39.9
Tsat 54p9.xls	Mod. 4	49.8	53.8	54.2	59.7	59.2	58.8	60.2	59.4	59.5	32.6	51.8

File Name	Trial #	T_{wout} [°C]	T_{incp} [°C]	T_{inph} [°C]	P_1 [kPa]	P_2 [kPa]	P_3 [kPa]	Q_{PH} [W]	Q_{CP} [W]	ΔP_{CP} [kPa]	$\dot{m}$ [g/s]
Tsat 24p4.xls	Base 1	22.3	28.4	23.8	649.4	648.4	647.4	76.8	425.7	1.005	3.889
Tsat 34p4.xls	Base 2	32.7	37.9	31.9	872.9	868.9	868.2	76.9	405.5	0.729	3.832
Tsat 40p2.xls	Base 3	38.4	43.2	36.4	1021.0	1016.5	1015.9	76.9	388.2	0.600	3.832
Tsat 54p9.xls	Base 4	52.5	56.4	47.2	1466.6	1461.5	1461.1	84.4	358.2	0.386	3.828
Tsat 25p3.xls	Mod. 1	23.1	28.2	24.7	668.3	667.8	666.9	73.0	424.8	0.876	3.919
Tsat 34p9.xls	Mod. 2	33.0	37.2	32.4	882.9	882.0	881.3	77.2	410.9	0.667	4.004
Tsat 42p9.xls	Mod. 3	41.3	44.8	38.9	1105.1	1103.6	1103.1	76.2	367.7	0.475	3.992
Tsat 54p9.xls	Mod. 4	53.0	55.8	47.9	1485.4	1482.4	1482.1	84.4	348.8	0.325	3.846

Table D.2: Test 1 Calculated Values								
File Name	Trial #	$Q_{PH,loss}$ [W]	$Q_{CP,loss}$ [W]	$Q_{PH,adj}$ [W]	$Q_{CP,adj}$ [W]	$T_{sat2}(P_2)$ [°C]	h_1 [kJ/kg]	h_2 [kJ/kg]
Tsat 24p4.xls	Base 1	-1.39	0.18	78.20	425.53	24.1	228.1	248.2
Tsat 34p4.xls	Base 2	0.95	1.24	75.93	404.29	34.3	242.8	262.7
Tsat 40p2.xls	Base 3	2.11	1.79	74.75	386.37	40.0	250.6	270.1
Tsat 54p9.xls	Base 4	5.11	3.27	79.31	354.89	54.2	269.9	290.6
Tsat 25p3.xls	Mod. 1	-1.34	0.01	74.29	424.80	25.1	230.2	249.1
Tsat 34p9.xls	Mod. 2	0.78	1.00	76.45	409.93	34.8	243.7	262.7
Tsat 42p9.xls	Mod. 3	2.54	1.83	73.66	365.92	43.1	255.1	273.5
Tsat 54p9.xls	Mod. 4	5.03	3.06	79.34	345.77	54.7	271.2	291.8
File Name	Trial #	h_3 [kJ/kg]	X_2 [-/-]	X_3 [-/-]	q_{CP} [kW/m^2]	g_{CP} [kg/m^{2}s]	$T_{sat,avg}$ [°C]	$h_{overall}$ [kW/m^{2}K]
Tsat 24p4.xls	Base 1	357.7	0.084	0.696	126.6	224.7	23.8	15.58
Tsat 34p4.xls	Base 2	368.2	0.087	0.712	120.3	221.5	34.0	16.37
Tsat 40p2.xls	Base 3	370.9	0.084	0.702	115.0	221.5	39.7	16.86
Tsat 54p9.xls	Base 4	383.3	0.085	0.717	105.6	221.2	53.8	18.12
Tsat 25p3.xls	Mod. 1	357.5	0.081	0.691	126.4	226.5	24.7	17.05
Tsat 34p9.xls	Mod. 2	365.1	0.083	0.692	122.0	231.4	34.4	18.15
Tsat 42p9.xls	Mod. 3	365.2	0.078	0.652	108.9	230.7	42.7	18.94
Tsat 54p9.xls	Mod. 4	381.7	0.088	0.703	102.9	222.3	54.4	20.28

Table D.3: Test 2 Measurement Data (Including Modified Tests from 6/4/15 and 6/25/15)												
File Name	Trial #	T_{sub} [°C]	T_{in} [°C]	T_{out} [°C]	T_{CP1} [°C]	T_{CP2} [°C]	T_{CP3} [°C]	T_{CP4} [°C]	T_{CP5} [°C]	T_{CPavg} [°C]	T_{amb} [°C]	T_{win} [°C]
Psat 1442 x3 75.xls	Base 1	48.3	53.1	53.5	60.6	59.4	59.1	60.8	60.1	60.0	30.7	50.1
MM 2p9.xls	Base 2	47.3	52.1	52.5	58.2	57.4	57.0	58.4	57.5	57.7	30.5	50.0
MM 3p1.xls	Base 3	49.3	53.8	54.2	60.2	59.3	59.0	60.4	59.7	59.7	30.5	51.9
MM 4p01.xls	Base 4	51.3	55.5	56.0	63.0	61.9	61.6	63.4	62.5	62.5	28.6	53.6
MM 4p37.xls	Base 5	51.5	56.0	56.4	63.8	62.6	62.2	64.3	63.2	63.2	27.8	54.0
MM 4p59.xls	Base 6	51.5	55.5	56.0	63.6	62.3	62.0	64.1	63.1	63.0	28.7	53.5
MM 4p69.xls	Base 7	51.1	55.3	55.8	63.3	62.1	61.7	63.8	62.7	62.7	27.8	53.2
MM 4p91.xls	Base 8	51.6	55.7	56.2	64.2	62.9	62.5	64.8	63.6	63.6	28.8	53.5
MM 5p41.xls	Base 9	51.7	55.8	56.3	64.8	63.4	63.0	65.5	64.2	64.2	28.9	53.4
MM 5p43.xls	Base 10	52.2	56.4	56.9	65.4	63.9	63.6	66.1	64.9	64.8	28.3	54.0
MM 5p63.xls	Base 11	51.9	56.0	56.5	65.2	63.7	63.4	65.9	64.6	64.6	29.0	53.6
MM 5p83.xls	Base 12	52.2	56.3	56.8	65.7	64.1	63.7	66.4	65.0	65.0	29.0	53.8
MM 6p25.xls	Base 13	51.9	56.1	56.6	65.9	64.3	63.9	66.7	65.2	65.2	28.9	53.4
MM 1p57.xls	Base 14	47.8	54.6	55.7	59.7	59.3	59.1	60.0	59.8	59.6	27.6	53.5
MM 2p05.xls	Base 15	49.2	55.1	55.8	60.1	59.5	59.3	60.3	60.1	59.9	27.6	53.7
MM 2p7.xls	Base 16	49.9	55.0	55.5	60.8	60.1	59.8	61.0	60.7	60.5	27.3	53.5
MM 3p24.xls	Base 17	51.6	56.7	57.1	63.3	62.4	62.1	63.6	63.2	62.9	27.6	55.0
MM 4p05.xls	Base 18	51.2	55.4	55.9	62.9	61.8	61.4	63.3	62.7	62.4	28.1	53.5
MM 2p76.xls	M5/3, 1	48.3	52.8	53.3	57.9	57.7	57.4	58.6	57.6	57.8	28.1	51.6
MM 3p53.xls	M5/3, 2	48.9	52.7	53.1	58.4	58.1	57.8	59.2	58.0	58.3	28.2	51.4
MM 2p52.xls	M5/3, 3	46.3	51.3	51.8	56.2	56.1	55.7	56.8	56.2	56.2	30.7	49.5
MM 3p32.xls	M5/3, 4	47.4	51.8	52.3	57.3	57.1	56.7	58.1	57.2	57.3	31.0	49.7

Table D.3 (cont.)

File Name	Trial #	T_{sub} [°C]	T_{in} [°C]	T_{out} [°C]	T_{CP1} [°C]	T_{CP2} [°C]	T_{CP3} [°C]	T_{CP4} [°C]	T_{CP5} [°C]	T_{CPavg} [°C]	T_{amb} [°C]	T_{win} [°C]
MM 3p33.xls	M5/3, 5	49.7	54.1	54.5	59.3	59.1	58.8	60.0	59.0	59.2	29.4	52.4
MM 3p61.xls	M5/3, 6	50.2	54.7	55.2	60.3	60.1	59.8	61.3	60.1	60.3	29.5	52.9
MM 3p69.xls	M5/3, 7	47.7	52.1	52.5	57.8	57.6	57.1	58.7	57.7	57.8	31.4	49.7
MM 4p05.xls	M5/3, 8	48.0	52.3	52.8	58.3	58.1	57.7	59.4	58.3	58.3	31.5	49.8
MM 4p25.xls	M5/3, 9	48.0	52.4	52.8	58.4	58.2	57.8	59.5	58.4	58.5	31.6	49.7
MM 4p64.xls	M5/3, 10	48.4	52.8	53.3	59.3	59.0	58.6	60.5	59.4	59.4	31.7	50.0
MM 4p88.xls	M5/3, 11	48.5	52.9	53.3	59.5	59.2	58.7	60.8	59.7	59.6	31.9	49.9
MM 5p32.xls	M5/3, 12	48.4	52.9	53.3	60.0	59.6	59.1	61.5	60.3	60.1	31.9	49.7
MM 5p47.xls	M5/3, 13	48.4	52.8	53.2	59.9	59.5	59.1	61.4	60.2	60.0	31.9	49.7
MM 5p59.xls	M5/3, 14	48.4	52.8	53.2	60.0	59.6	59.2	61.6	60.3	60.2	32.1	49.6
MM 5p77.xls	M5/3, 15	48.4	52.9	53.4	60.3	59.9	59.4	62.0	60.6	60.5	32.1	49.6
MM 5p89.xls	M5/3, 16	48.4	52.9	53.4	60.4	59.9	59.5	62.0	60.6	60.5	32.1	49.5
MM 6p01.xls	M5/3, 17	48.7	53.3	53.7	60.8	60.3	59.9	62.5	61.0	60.9	32.1	49.9
MM 6p01.xls	M5/3, 18	47.1	53.3	54.1	57.4	57.4	57.2	57.8	57.4	57.4	32.1	52.1
MM 6p01.xls	M5/3, 19	48.3	53.6	54.4	57.7	57.6	57.4	58.1	57.8	57.7	31.9	52.3
MM 6p01.xls	M5/3, 20	48.9	53.8	54.2	58.5	58.3	58.0	59.0	58.4	58.4	31.9	52.2
MM 2p41.xls	M6/4,1	47.8	52.6	53.1	57.5	57.2	56.9	57.9	57.6	57.4	31.8	51.0
MM 2p87.xls	M6/4, 2	48.0	52.4	52.8	57.8	57.4	57.0	58.2	57.8	57.6	31.9	50.7
MM 3p01.xls	M6/4, 3	48.3	52.7	53.1	58.1	57.7	57.4	58.6	58.2	58.0	32.0	50.9
MM 3p33.xls	M6/4, 4	48.7	52.9	53.3	58.6	58.2	57.8	59.1	58.7	58.5	32.2	51.0
MM 3p64.xls	M6/4, 5	48.7	52.7	53.1	58.6	58.2	57.8	59.3	58.8	58.5	32.2	50.7
MM 3p84.xls	M6/4, 6	48.9	52.9	53.3	59.0	58.5	58.0	59.6	59.2	58.9	32.3	50.9
MM 4p14.xls	M6/4, 7	49.0	52.9	53.3	59.2	58.7	58.2	60.0	59.5	59.1	32.5	50.7
MM 4p37.xls	M6/4, 8	49.7	53.6	54.1	60.1	59.6	59.1	61.0	60.4	60.0	32.7	51.5

Table D.3 (cont.)

File Name	Trial #	T_{sub} [°C]	T_{in} [°C]	T_{out} [°C]	T_{CP1} [°C]	T_{CP2} [°C]	T_{CP3} [°C]	T_{CP4} [°C]	T_{CP5} [°C]	T_{CPavg} [°C]	T_{amb} [°C]	T_{win} [°C]
MM 4p65.xls	M6/4, 9	49.2	53.0	53.4	59.7	59.2	58.7	60.7	60.1	59.7	32.7	50.7
MM 4p81.xls	M6/4, 10	49.4	53.3	53.7	60.2	59.6	59.1	61.2	60.6	60.1	32.8	50.9
MM 5p26.xls	M6/4, 11	49.2	53.0	53.4	60.4	59.7	59.2	61.5	60.8	60.3	32.8	50.5
MM 2p30.xls	M6/25, 1	46.7	51.1	51.6	55.8	55.5	55.2	56.2	56.1	55.8	31.6	49.8
MM 2p86.xls	M6/25, 2	46.9	51.0	51.4	56.3	55.9	55.5	56.8	56.5	56.2	31.4	49.4
MM 3p25.xls	M6/25, 3	47.3	51.2	51.6	56.8	56.3	55.9	57.3	57.0	56.7	31.6	49.6
MM 3p55.xls	M6/25, 4	47.9	51.5	51.9	57.4	56.9	56.5	58.0	57.7	57.3	31.6	49.9
MM 3p93.xls	M6/25, 5	47.8	51.4	51.8	57.7	57.1	56.7	58.4	58.1	57.6	31.9	49.6
MM 4p35.xls	M6/25, 6	47.9	51.5	52.0	58.2	57.6	57.1	59.1	58.8	58.2	31.9	49.5
MM 4p85.xls	M6/25, 7	48.0	51.6	52.0	58.7	58.0	57.5	59.6	59.2	58.6	31.9	49.4
MM 5p47.xls	M6/25, 8	48.2	52.0	52.4	59.4	58.6	58.1	60.4	60.0	59.3	32.0	49.5

File Name	Trial #	T_{wout} [°C]	T_{incp} [°C]	T_{inph} [°C]	P_1 [kPa]	P_2 [kPa]	P_3 [kPa]	Q_{PH} [W]	Q_{CP} [W]	ΔP_{CP} [kPa]	$\dot{m}$ [g/s]
Psat 1442 x3 75.xls	Base 1	52.3	56.4	46.9	1458.0	1453.8	1453.3	107.21	394.29	0.472	4.145
MM 2p9.xls	Base 2	51.2	55.0	46.0	1421.9	1416.9	1416.6	73.78	280.25	0.239	2.879
MM 3p1.xls	Base 3	52.9	56.8	47.6	1483.9	1479.0	1478.8	81.86	304.29	0.279	3.152
MM 4p01.xls	Base 4	54.9	58.8	48.4	1550.9	1549.2	1548.7	98.02	384.77	0.425	4.016
MM 4p37.xls	Base 5	55.2	59.3	48.1	1567.9	1563.7	1563.2	96.29	420.92	0.502	4.372
MM 4p59.xls	Base 6	54.9	59.0	48.4	1550.7	1548.6	1548.1	108.33	433.68	0.550	4.592
MM 4p69.xls	Base 7	54.6	58.7	47.9	1541.9	1537.6	1537.1	108.49	436.46	0.568	4.709
MM 4p91.xls	Base 8	55.1	59.3	48.5	1558.8	1556.6	1556.0	120.09	462.88	0.638	4.912
MM 5p41.xls	Base 9	55.1	59.6	48.5	1562.2	1559.7	1558.9	129.04	509.3	0.784	5.427
MM 5p43.xls	Base 10	55.6	60.2	48.8	1585.3	1581.4	1580.6	131.06	514.8	0.770	5.435
MM 5p63.xls	Base 11	55.3	59.8	48.7	1571.0	1568.0	1567.2	137.35	526.6	0.850	5.640

Table D.3 (cont.)

File Name	Trial #	T_{wout} [°C]	T_{incp} [°C]	T_{inph} [°C]	P_1 [kPa]	P_2 [kPa]	P_3 [kPa]	Q_{PH} [W]	Q_{CP} [W]	ΔP_{CP} [kPa]	$\dot{m}$ [g/s]
MM 5p83.xls	Base 12	55.5	60.1	48.8	1580.8	1577.4	1576.5	139.36	546.5	0.910	5.836
MM 6p25.xls	Base 13	55.3	60.0	48.7	1574.9	1571.7	1570.6	151.51	577.8	1.030	6.277
MM 1p57.xls	Base 14	54.6	57.8	47.5	1536.6	1533.3	1533.2	44.67	156.5	0.052	1.575
MM 2p05.xls	Base 15	54.3	57.8	48.1	1531.3	1529.0	1529.0	59.93	194.8	0.096	2.053
MM 2p7.xls	Base 16	54.3	57.8	47.7	1529.5	1525.3	1525.1	70.37	251.97	0.167	2.700
MM 3p24.xls	Base 17	55.9	59.8	49.0	1592.2	1588.1	1587.8	89.60	314.07	0.269	3.247
MM 4p05.xls	Base 18	54.7	58.6	48.5	1545.2	1543.8	1543.4	93.70	383.20	0.420	4.051
MM 2p76.xls	M5/3, 1	52.7	55.1	46.1	1446.5	1442.0	1441.8	73.96	270.60	0.149	2.761
MM 3p53.xls	M5/3, 2	52.6	55.0	46.0	1445.5	1441.2	1440.9	87.04	340.34	0.282	3.535
MM 2p52.xls	M5/3, 3	50.6	53.5	45.5	1396.9	1392.0	1391.9	69.95	251.77	0.111	2.513
MM 3p32.xls	M5/3, 4	51.1	54.0	46.0	1416.0	1411.0	1410.7	81.82	319.16	0.235	3.314
MM 3p33.xls	M5/3, 5	53.5	56.2	47.6	1498.0	1493.2	1493.0	82.14	313.23	0.231	3.337
MM 3p61.xls	M5/3, 6	54.2	56.9	47.7	1520.8	1516.3	1516.0	88.58	359.33	0.291	3.609
MM 3p69.xls	M5/3, 7	51.2	54.3	46.2	1424.6	1420.0	1419.7	89.36	355.60	0.315	3.688
MM 4p05.xls	M5/3, 8	51.5	54.6	46.3	1434.1	1429.7	1429.3	99.83	389.40	0.392	4.051
MM 4p25.xls	M5/3, 9	51.5	54.7	46.4	1436.2	1431.9	1431.5	103.63	404.0	0.446	4.234
MM 4p64.xls	M5/3, 10	51.9	55.2	46.7	1452.3	1448.2	1447.7	113.73	449.3	0.549	4.640
MM 4p88.xls	M5/3, 11	51.9	55.3	46.8	1453.7	1450.0	1449.4	119.95	469.3	0.609	4.887
MM 5p32.xls	M5/3, 12	52.0	55.5	46.7	1454.4	1450.9	1450.2	129.27	519.0	0.750	5.343
MM 5p47.xls	M5/3, 13	51.9	55.4	46.7	1452.1	1449.1	1448.3	133.29	523.9	0.787	5.484
MM 5p59.xls	M5/3, 14	52.0	55.4	46.7	1452.1	1449.9	1449.1	132.44	541.0	0.832	5.591
MM 5p77.xls	M5/3, 15	52.0	55.6	46.8	1456.8	1454.0	1453.1	138.82	558.9	0.901	5.798
MM 5p89.xls	M5/3, 16	52.1	55.6	46.8	1457.0	1454.4	1453.5	144.63	563.55	0.936	5.876

Table D.3 (cont.)

File Name	Trial #	T_{wout} [°C]	T_{incp} [°C]	T_{inph} [°C]	P_1 [kPa]	P_2 [kPa]	P_3 [kPa]	Q_{PH} [W]	Q_{CP} [W]	ΔP_{CP} [kPa]	$\dot{m}$ [g/s]
MM 6p01.xls	M5/3, 17	52.4	55.9	47.0	1469.1	1466.7	1465.7	145.54	574.91	0.973	6.005
MM 6p01.xls	M5/3, 18	52.6	55.4	47.2	1465.9	1462.0	1462.0	43.48	147.58	-0.012	1.508
MM 6p01.xls	M5/3, 19	52.9	55.6	47.5	1480.4	1474.9	1474.9	48.94	175.52	0.006	1.796
MM 6p01.xls	M5/3, 20	53.0	55.7	47.6	1484.1	1479.2	1479.1	62.46	233.56	0.077	2.377
MM 2p41.xls	M6/4,1	51.8	54.6	46.9	1441.0	1436.1	1436.0	64.49	235.10	0.104	2.417
MM 2p87.xls	M6/4, 2	51.7	54.4	46.7	1434.0	1429.1	1428.9	70.86	276.49	0.184	2.870
MM 3p01.xls	M6/4, 3	51.9	54.6	46.9	1443.1	1438.3	1438.1	72.40	292.25	0.200	3.013
MM 3p33.xls	M6/4, 4	52.2	54.9	47.1	1452.2	1447.7	1447.5	81.81	320.65	0.256	3.327
MM 3p64.xls	M6/4, 5	52.0	54.8	47.0	1444.9	1440.5	1440.2	88.50	347.58	0.320	3.637
MM 3p84.xls	M6/4, 6	52.2	55.0	47.1	1451.5	1447.2	1446.8	89.93	366.64	0.351	3.851
MM 4p14.xls	M6/4, 7	52.2	55.0	47.1	1452.7	1449.0	1448.5	99.35	394.57	0.443	4.137
MM 4p37.xls	M6/4, 8	53.0	55.8	47.6	1480.9	1477.4	1477.0	99.00	417.53	0.463	4.360
MM 4p65.xls	M6/4, 9	52.4	55.3	47.2	1457.8	1454.4	1453.9	106.95	443.48	0.549	4.641
MM 4p81.xls	M6/4, 10	52.6	55.6	47.3	1467.6	1464.4	1463.8	116.43	465.11	0.630	4.812
MM 5p26.xls	M6/4, 11	52.4	55.5	47.1	1458.7	1455.7	1454.9	118.62	510.28	0.757	5.264
MM 2p30.xls	M6/25, 1	50.6	53.1	45.9	1387.1	1382.2	1382.1	59.28	228.38	0.102	2.299
MM 2p86.xls	M6/25, 2	50.4	53.0	45.7	1383.5	1378.6	1378.4	68.24	279.87	0.189	2.861
MM 3p25.xls	M6/25, 3	50.7	53.3	46.0	1391.1	1386.2	1385.9	77.65	311.77	0.264	3.246
MM 3p55.xls	M6/25, 4	51.1	53.7	46.2	1404.3	1399.6	1399.3	84.09	343.83	0.333	3.548
MM 3p93.xls	M6/25, 5	51.0	53.7	46.2	1400.2	1395.7	1395.3	89.79	381.92	0.414	3.930
MM 4p35.xls	M6/25, 6	51.0	53.9	46.3	1405.2	1400.9	1400.4	99.74	428.21	0.512	4.346
MM 4p85.xls	M6/25, 7	51.0	54.1	46.3	1408.4	1404.2	1403.6	112.29	467.70	0.637	4.856
MM 5p47.xls	M6/25, 8	51.3	54.5	46.5	1420.0	1416.0	1415.2	127.57	513.74	0.802	5.473

Table D.4: Test 2 Calculated Values (Including Modified Tests from 6/4/15 and 6/25/15)								
File Name	Trial #	$Q_{PH,loss}$ [W]	$Q_{CP,loss}$ [W]	$Q_{PH,adj}$ [W]	$Q_{CP,adj}$ [W]	$T_{sat2}(P_2)$ [°C]	h_1 [kJ/kg]	h_2 [kJ/kg]
Psat 1442 x3 75.xls	Base 1	5.22	3.38	101.99	390.91	54.0	268.8	293.5
MM 2p9.xls	Base 2	5.03	3.22	68.75	277.03	52.9	267.4	291.3
MM 3p1.xls	Base 3	5.52	3.46	76.35	300.83	54.7	270.5	294.7
MM 4p01.xls	Base 4	6.49	3.98	91.53	380.79	56.6	273.5	296.3
MM 4p37.xls	Base 5	6.81	4.14	89.48	416.78	57.0	273.9	294.4
MM 4p59.xls	Base 6	6.50	3.99	101.83	429.69	56.5	273.8	296.0
MM 4p69.xls	Base 7	6.65	4.06	101.84	432.40	56.3	273.3	294.9
MM 4p91.xls	Base 8	6.53	4.02	113.56	458.86	56.8	274.1	297.2
MM 5p41.xls	Base 9	6.52	4.04	122.51	505.30	56.8	274.2	296.8
MM 5p43.xls	Base 10	6.81	4.19	124.26	510.59	57.4	274.9	297.8
MM 5p63.xls	Base 11	6.56	4.06	130.80	522.50	57.1	274.5	297.7
MM 5p83.xls	Base 12	6.62	4.09	132.74	542.42	57.3	274.9	297.6
MM 6p25.xls	Base 13	6.59	4.10	144.91	573.75	57.2	274.6	297.7
MM 1p57.xls	Base 14	6.20	3.98	38.47	152.49	56.1	268.1	292.5
MM 2p05.xls	Base 15	6.44	3.98	53.48	190.87	56.0	270.3	296.3
MM 2p7.xls	Base 16	6.59	4.02	63.77	247.94	55.9	271.4	295.0
MM 3p24.xls	Base 17	6.97	4.24	82.63	309.83	57.6	274.1	299.5
MM 4p05.xls	Base 18	6.59	4.01	87.10	379.19	56.4	273.3	294.8
MM 2p76.xls	M5/3, 1	5.90	3.56	68.06	267.04	53.6	269.0	293.6
MM 3p53.xls	M5/3, 2	5.93	3.54	81.12	336.80	53.6	269.8	292.8
MM 2p52.xls	M5/3, 3	4.74	3.00	65.21	248.77	52.2	265.8	291.8
MM 3p32.xls	M5/3, 4	4.88	3.04	76.94	316.13	52.7	267.5	290.7

Table D.4 (cont.)

File Name	Trial #	$Q_{PH,loss}$ [W]	$Q_{CP,loss}$ [W]	$Q_{PH,adj}$ [W]	$Q_{CP,adj}$ [W]	$T_{sat2}(P_2)$ [°C]	h_1 [kJ/kg]	h_2 [kJ/kg]
MM 3p33.xls	M5/3, 5	5.89	3.52	76.25	309.71	55.0	271.1	293.9
MM 3p61.xls	M5/3, 6	6.02	3.61	82.56	355.72	55.7	271.8	294.7
MM 3p69.xls	M5/3, 7	4.85	3.02	84.50	352.58	53.0	268.0	290.9
MM 4p05.xls	M5/3, 8	4.89	3.05	94.94	386.36	53.3	268.4	291.8
MM 4p25.xls	M5/3, 9	4.89	3.04	98.74	400.95	53.3	268.5	291.8
MM 4p64.xls	M5/3, 10	4.97	3.10	108.76	446.16	53.8	269.1	292.6
MM 4p88.xls	M5/3, 11	4.93	3.09	115.03	466.20	53.8	269.2	292.7
MM 5p32.xls	M5/3, 12	4.90	3.10	124.37	515.91	53.9	269.1	292.4
MM 5p47.xls	M5/3, 13	4.89	3.09	128.40	520.86	53.8	269.1	292.5
MM 5p59.xls	M5/3, 14	4.84	3.07	127.60	537.96	53.8	269.1	291.9
MM 5p77.xls	M5/3, 15	4.87	3.10	133.95	555.78	54.0	269.1	292.2
MM 5p89.xls	M5/3, 16	4.87	3.10	139.76	560.46	54.0	269.1	292.9
MM 6p01.xls	M5/3, 17	4.95	3.14	140.59	571.77	54.3	269.6	293.0
MM 6p01.xls	M5/3, 18	4.75	3.08	38.73	144.50	54.2	267.1	292.8
MM 6p01.xls	M5/3, 19	4.99	3.12	43.94	172.40	54.5	268.9	293.3
MM 6p01.xls	M5/3, 20	5.10	3.14	57.36	230.42	54.7	269.9	294.0
MM 2p41.xls	M6/4,1	4.83	2.99	59.66	232.11	53.5	268.2	292.9
MM 2p87.xls	M6/4, 2	4.80	2.96	66.06	273.53	53.3	268.4	291.5
MM 3p01.xls	M6/4, 3	4.85	2.98	67.55	289.28	53.5	269.0	291.4
MM 3p33.xls	M6/4, 4	4.89	2.99	76.92	317.65	53.8	269.6	292.7
MM 3p64.xls	M6/4, 5	4.84	2.97	83.66	344.61	53.6	269.5	292.5
MM 3p84.xls	M6/4, 6	4.86	2.98	85.06	363.66	53.8	269.8	291.9
MM 4p14.xls	M6/4, 7	4.84	2.97	94.51	391.60	53.8	270.0	292.8
MM 4p37.xls	M6/4, 8	4.97	3.04	94.03	414.49	54.6	271.0	292.6

Table D.4 (cont.)

File Name	Trial #	$Q_{PH,loss}$ [W]	$Q_{CP,loss}$ [W]	$Q_{PH,adj}$ [W]	$Q_{CP,adj}$ [W]	$T_{sat2}(P_2)$ [°C]	h_1 [kJ/kg]	h_2 [kJ/kg]
MM 4p65.xls	M6/4, 9	4.83	2.97	102.12	440.50	54.0	270.3	292.3
MM 4p81.xls	M6/4, 10	4.87	3.01	111.56	462.10	54.2	270.6	293.7
MM 5p26.xls	M6/4, 11	4.79	2.98	113.83	507.29	54.0	270.3	291.9
MM 2p30.xls	M6/25, 1	4.53	2.83	54.75	225.55	51.9	266.5	290.3
MM 2p86.xls	M6/25, 2	4.59	2.85	63.65	277.02	51.8	266.8	289.0
MM 3p25.xls	M6/25, 3	4.64	2.86	73.01	308.91	52.0	267.4	289.9
MM 3p55.xls	M6/25, 4	4.73	2.90	79.36	340.93	52.4	268.2	290.6
MM 3p93.xls	M6/25, 5	4.63	2.86	85.16	379.06	52.3	268.1	289.8
MM 4p35.xls	M6/25, 6	4.66	2.90	95.08	425.32	52.4	268.3	290.2
MM 4p85.xls	M6/25, 7	4.70	2.92	107.59	464.78	52.5	268.4	290.6
MM 5p47.xls	M6/25, 8	4.75	2.97	122.81	510.77	52.9	268.8	291.2
File Name	Trial #	h_3 [kJ/kg]	X_2 [-/-]	X_3 [-/-]	q_{CP} [kW/m^2]	g_{CP} [kg/m^{2}s]	$T_{sat,avg}$ [°C]	$h_{overall}$ [kW/m^{2}K]
Psat 1442 x3 75.xls	Base 1	387.8	0.106	0.748	116.3	239.5	53.6	18.21
MM 2p9.xls	Base 2	387.5	0.102	0.751	82.4	166.4	52.6	16.14
MM 3p1.xls	Base 3	390.1	0.108	0.761	89.5	182.1	54.3	16.67
MM 4p01.xls	Base 4	391.1	0.100	0.760	113.3	232.1	56.2	17.89
MM 4p37.xls	Base 5	389.7	0.082	0.748	124.0	252.7	56.6	18.68
MM 4p59.xls	Base 6	389.6	0.098	0.749	127.9	265.4	56.1	18.55
MM 4p69.xls	Base 7	386.7	0.093	0.730	128.7	272.1	55.9	18.83
MM 4p91.xls	Base 8	390.6	0.104	0.756	136.6	283.9	56.4	18.85
MM 5p41.xls	Base 9	389.9	0.100	0.750	150.4	313.6	56.4	19.46
MM 5p43.xls	Base 10	391.7	0.101	0.760	152.0	314.1	57.0	19.68
MM 5p63.xls	Base 11	390.4	0.104	0.752	155.5	325.9	56.7	19.68

Table D.4 (cont.)

File Name	Trial #	h_3 [kJ/kg]	X_2 [-/-]	X_3 [-/-]	q_{CP} [kW/m^2]	g_{CP} [kg/m^{2}s]	$T_{sat,avg}$ [°C]	$h_{overall}$ [kW/m^{2}K]
MM 5p83.xls	Base 12	390.6	0.101	0.753	161.4	337.2	56.9	19.99
MM 6p25.xls	Base 13	389.1	0.103	0.743	170.7	362.7	56.8	20.32
MM 1p57.xls	Base 14	389.3	0.078	0.749	45.4	91.0	55.6	11.52
MM 2p05.xls	Base 15	389.3	0.106	0.749	56.8	118.7	55.7	13.69
MM 2p7.xls	Base 16	386.8	0.097	0.733	73.8	156.0	55.6	15.07
MM 3p24.xls	Base 17	395.0	0.112	0.782	92.2	187.6	57.2	16.30
MM 4p05.xls	Base 18	388.4	0.091	0.742	112.8	234.1	56.0	17.67
MM 2p76.xls	M5/3, 1	390.3	0.111	0.767	79.5	159.6	53.3	17.62
MM 3p53.xls	M5/3, 2	388.0	0.105	0.751	100.2	204.3	53.3	19.79
MM 2p52.xls	M5/3, 3	390.8	0.112	0.776	74.0	145.2	51.9	17.14
MM 3p32.xls	M5/3, 4	386.1	0.100	0.742	94.1	191.5	52.4	19.20
MM 3p33.xls	M5/3, 5	386.7	0.099	0.736	92.2	192.9	54.7	20.24
MM 3p61.xls	M5/3, 6	393.3	0.098	0.778	105.9	208.6	55.3	21.12
MM 3p69.xls	M5/3, 7	386.5	0.098	0.744	104.9	213.1	52.6	20.43
MM 4p05.xls	M5/3, 8	387.2	0.102	0.747	115.0	234.1	52.9	21.16
MM 4p25.xls	M5/3, 9	386.5	0.101	0.742	119.3	244.7	53.0	21.59
MM 4p64.xls	M5/3, 10	388.7	0.102	0.755	132.8	268.1	53.4	22.28
MM 4p88.xls	M5/3, 11	388.1	0.102	0.751	138.7	282.4	53.5	22.62
MM 5p32.xls	M5/3, 12	388.9	0.100	0.756	153.5	308.8	53.5	23.23
MM 5p47.xls	M5/3, 13	387.5	0.101	0.747	155.0	316.9	53.4	23.50
MM 5p59.xls	M5/3, 14	388.1	0.097	0.751	160.1	323.0	53.4	23.79
MM 5p77.xls	M5/3, 15	388.1	0.098	0.750	165.4	335.0	53.5	23.94
MM 5p89.xls	M5/3, 16	388.3	0.102	0.751	166.8	339.6	53.6	24.07
MM 6p01.xls	M5/3, 17	388.2	0.100	0.750	170.2	347.0	53.9	24.30

Table D.4 (cont.)

File Name	Trial #	h_3 [kJ/kg]	X_2 [-/-]	X_3 [-/-]	q_{CP} [kW/m^2]	g_{CP} [kg/m^{2}s]	$T_{sat,avg}$ [°C]	$h_{overall}$ [kW/m^{2}K]
MM 6p01.xls	M5/3, 18	388.6	0.099	0.753	43.0	87.1	53.9	12.35
MM 6p01.xls	M5/3, 19	389.4	0.100	0.756	51.3	103.8	54.3	14.94
MM 6p01.xls	M5/3, 20	391.0	0.103	0.767	68.6	137.3	54.3	16.78
MM 2p41.xls	M6/4,1	388.9	0.108	0.758	69.1	139.7	53.2	16.16
MM 2p87.xls	M6/4, 2	386.8	0.100	0.744	81.4	165.9	52.9	17.34
MM 3p01.xls	M6/4, 3	387.4	0.097	0.748	86.1	174.1	53.2	17.91
MM 3p33.xls	M6/4, 4	388.2	0.103	0.752	94.5	192.2	53.5	18.83
MM 3p64.xls	M6/4, 5	387.3	0.104	0.746	102.6	210.2	53.2	19.40
MM 3p84.xls	M6/4, 6	386.3	0.098	0.739	108.2	222.6	53.4	19.93
MM 4p14.xls	M6/4, 7	387.5	0.103	0.747	116.5	239.1	53.5	20.65
MM 4p37.xls	M6/4, 8	387.7	0.094	0.745	123.4	251.9	54.2	21.23
MM 4p65.xls	M6/4, 9	387.2	0.098	0.744	131.1	268.2	53.6	21.56
MM 4p81.xls	M6/4, 10	389.8	0.105	0.760	137.5	278.1	53.9	21.97
MM 5p26.xls	M6/4, 11	388.3	0.095	0.751	151.0	304.2	53.6	22.48
MM 2p30.xls	M6/25, 1	388.4	0.105	0.761	67.1	132.8	51.6	16.21
MM 2p86.xls	M6/25, 2	385.8	0.097	0.744	82.4	165.4	51.5	17.53
MM 3p25.xls	M6/25, 3	385.1	0.101	0.738	91.9	187.6	51.7	18.48
MM 3p55.xls	M6/25, 4	386.7	0.102	0.748	101.5	205.1	52.1	19.31
MM 3p93.xls	M6/25, 5	386.3	0.098	0.745	112.8	227.1	51.9	20.03
MM 4p35.xls	M6/25, 6	388.1	0.099	0.757	126.6	251.2	52.1	20.83
MM 4p85.xls	M6/25, 7	386.3	0.101	0.744	138.3	280.7	52.2	21.60
MM 5p47.xls	M6/25, 8	384.5	0.102	0.731	152.0	316.3	52.5	22.41

Table D.5: Test 5 Measurement Data												
File Name	Trial #	T_{sub} [°C]	T_{in} [°C]	T_{out} [°C]	T_{CP1} [°C]	T_{CP2} [°C]	T_{CP3} [°C]	T_{CP4} [°C]	T_{CP5} [°C]	T_{CPavg} [°C]	T_{amb} [°C]	T_{win} [°C]
X_2 p105.xls	Base 1	51.7	54.9	55.1	57.5	57.2	57.1	57.4	57.2	57.3	27.6	53.6
X_2 p125.xls	Base 2	51.6	55.0	55.1	57.5	57.2	57.0	57.3	57.3	57.3	27.4	53.6
X_2 p152.xls	Base 3	51.6	55.0	55.2	57.5	57.3	57.1	57.4	57.3	57.3	27.4	53.5
X_2 p177.xls	Base 4	51.5	55.1	55.2	57.6	57.3	57.2	57.5	57.4	57.4	27.8	53.5
X_2 p195.xls	Base 5	51.5	55.0	55.1	57.5	57.3	57.1	57.4	57.3	57.3	27.7	53.4
X_2 p228.xls	Base 6	51.3	55.0	55.1	57.4	57.2	57.0	57.3	57.2	57.2	27.8	53.2
X_2 p274.xls	Base 7	51.3	55.0	55.0	57.4	57.2	57.0	57.4	57.2	57.3	27.8	53.1
X_2 p290.xls	Base 8	51.5	55.3	55.4	57.8	57.5	57.4	57.7	57.6	57.6	27.8	53.4
X_2 p343.xls	Base 9	51.4	55.4	55.4	57.8	57.6	57.4	57.7	57.6	57.6	27.8	53.3
X_2 p358.xls	Base 10	51.7	55.7	55.8	58.1	57.9	57.7	58.1	57.9	58.0	27.8	53.6
X_2 p381.xls	Base 11	51.2	55.2	55.3	57.7	57.4	57.3	57.6	57.5	57.5	27.8	53.1
X_2 p416.xls	Base 12	51.2	55.3	55.4	57.7	57.5	57.4	57.7	57.6	57.6	27.8	53.1
X_2 p062.xls	Mod. 1	49.4	52.3	52.5	54.8	54.7	54.5	54.8	54.7	54.7	29.4	51.1
X_2 p079.xls	Mod. 2	50.0	53.0	53.2	55.5	55.4	55.2	55.4	55.3	55.4	29.6	51.7
X_2 p085.xls	Mod. 3	50.2	53.2	53.4	55.8	55.6	55.4	55.7	55.6	55.6	29.7	52.0
X_2 p094.xls	Mod. 4	49.7	52.8	52.9	55.3	55.1	54.9	55.2	55.1	55.1	29.6	51.4
X_2 p128.xls	Mod. 5	50.2	53.4	53.6	55.9	55.8	55.6	55.8	55.7	55.8	29.7	52.0
X_2 p143.xls	Mod. 6	49.7	53.0	53.1	55.4	55.3	55.1	55.4	55.3	55.3	29.7	51.4
X_2 p179.xls	Mod. 7	50.1	53.5	53.6	55.9	55.8	55.6	55.8	55.7	55.8	29.9	51.8
X_2 p229.xls	Mod. 8	50.4	53.9	53.9	56.2	56.1	55.9	56.2	56.1	56.1	29.9	52.1
X_2 p274.xls	Mod. 9	50.2	53.8	53.9	56.2	56.1	55.9	56.1	56.0	56.1	29.9	51.9
X_2 p328.xls	Mod. 10	51.8	55.6	55.7	58.0	57.9	57.7	57.9	57.8	57.9	30.1	53.7

Table D.5 (cont.)

File Name	Trial #	T_{sub} [°C]	T_{in} [°C]	T_{out} [°C]	T_{CP1} [°C]	T_{CP2} [°C]	T_{CP3} [°C]	T_{CP4} [°C]	T_{CP5} [°C]	T_{CPavg} [°C]	T_{amb} [°C]	T_{win} [°C]
X_2 p372.xls	Mod. 11	51.8	55.7	55.7	58.0	57.9	57.7	58.0	57.9	57.9	30.2	53.6
X_2 p424.xls	Mod. 12	51.9	55.8	55.9	58.2	58.1	57.9	58.2	58.1	58.1	30.1	53.7

File Name	Trial #	T_{wout} [°C]	T_{incp} [°C]	T_{inph} [°C]	P_1 [kPa]	P_2 [kPa]	P_3 [kPa]	Q_{PH} [W]	Q_{CP} [W]	ΔP_{CP} [kPa]	$\dot{m}$ [g/s]
X_2 p105.xls	Base 1	54.0	55.6	48.2	1524.5	1523.3	1523.1	115.92	75.84	0.203	5.005
X_2 p125.xls	Base 2	54.0	55.7	48.4	1524.2	1523.0	1522.8	129.47	75.65	0.202	4.960
X_2 p152.xls	Base 3	54.0	55.8	48.5	1525.6	1524.5	1524.3	150.76	76.24	0.211	4.948
X_2 p177.xls	Base 4	54.0	55.8	48.6	1526.6	1525.8	1525.6	168.86	76.21	0.240	4.961
X_2 p195.xls	Base 5	54.0	55.7	48.6	1523.9	1523.2	1522.9	180.26	76.66	0.240	4.933
X_2 p228.xls	Base 6	53.8	55.7	48.6	1520.3	1518.9	1518.6	205.78	76.54	0.249	4.962
X_2 p274.xls	Base 7	53.8	55.8	48.7	1519.2	1518.4	1518.0	240.61	76.79	0.312	4.992
X_2 p290.xls	Base 8	54.1	56.0	48.9	1531.8	1530.5	1530.2	251.76	76.39	0.317	4.976
X_2 p343.xls	Base 9	54.1	56.2	48.9	1532.2	1531.4	1531.0	290.19	76.9	0.382	4.981
X_2 p358.xls	Base 10	54.4	56.5	49.1	1544.7	1543.7	1543.3	301.06	76.5	0.375	4.980
X_2 p381.xls	Base 11	54.0	56.1	48.8	1526.6	1525.7	1525.4	318.71	76.7	0.380	4.991
X_2 p416.xls	Base 12	54.0	56.2	48.9	1529.0	1528.2	1527.7	346.39	76.6	0.421	5.021
X_2 p062.xls	Mod. 1	51.5	53.0	46.1	1431.2	1427.3	1427.1	82.58	75.97	0.162	5.040
X_2 p079.xls	Mod. 2	52.2	53.6	46.5	1454.7	1451.0	1450.9	93.48	75.98	0.149	4.981
X_2 p085.xls	Mod. 3	52.4	53.9	46.7	1463.6	1460.0	1459.9	99.01	75.67	0.139	5.002
X_2 p094.xls	Mod. 4	51.9	53.4	46.5	1446.0	1442.6	1442.4	106.65	75.88	0.164	5.009
X_2 p128.xls	Mod. 5	52.5	54.0	47.1	1468.3	1465.1	1464.9	132.16	75.56	0.190	5.011
X_2 p143.xls	Mod. 6	52.0	53.5	46.8	1451.0	1448.0	1447.8	145.36	75.67	0.189	5.036
X_2 p179.xls	Mod. 7	52.4	54.0	47.2	1467.7	1465.0	1464.8	172.19	76.04	0.210	5.054
X_2 p229.xls	Mod. 8	52.8	54.4	47.6	1479.4	1476.4	1476.2	209.64	76.14	0.226	5.071

Table D.5 (cont.)

File Name	Trial #	T_{wout} [°C]	T_{incp} [°C]	T_{inph} [°C]	P_1 [kPa]	P_2 [kPa]	P_3 [kPa]	Q_{PH} [W]	Q_{CP} [W]	ΔP_{CP} [kPa]	$\dot{m}$ [g/s]
X_2 p274.xls	Mod. 9	52.7	54.3	47.6	1476.9	1474.1	1473.9	239.45	76.1	0.269	5.084
X_2 p328.xls	Mod. 10	54.5	56.2	48.9	1543.1	1540.7	1540.4	278.58	76.0	0.295	5.001
X_2 p372.xls	Mod. 11	54.5	56.2	49.1	1543.8	1541.4	1541.1	310.81	76.0	0.333	5.024
X_2 p424.xls	Mod. 12	54.7	56.5	49.2	1549.7	1547.5	1547.1	349.63	76.3	0.391	5.017

Table D.6: Test 3 Calculated Values								
File Name	Trial #	$Q_{PH,loss}$ [W]	$Q_{CP,loss}$ [W]	$Q_{PH,adj}$ [W]	$Q_{CP,adj}$ [W]	$T_{sat2}(P_2)$ [°C]	h_1 [kJ/kg]	h_2 [kJ/kg]
X_2 p105.xls	Base 1	6.75	3.70	109.17	72.15	55.9	274.2	296.0
X_2 p125.xls	Base 2	6.80	3.73	122.67	71.92	55.9	274.1	298.8
X_2 p152.xls	Base 3	6.80	3.74	143.96	72.49	55.9	274.0	303.1
X_2 p177.xls	Base 4	6.70	3.69	162.16	72.52	55.9	274.0	306.6
X_2 p195.xls	Base 5	6.71	3.70	173.55	72.97	55.9	273.9	309.0
X_2 p228.xls	Base 6	6.67	3.67	199.11	72.86	55.7	273.6	313.8
X_2 p274.xls	Base 7	6.64	3.68	233.97	73.10	55.7	273.5	320.4
X_2 p290.xls	Base 8	6.73	3.72	245.03	72.67	56.1	273.9	323.1
X_2 p343.xls	Base 9	6.72	3.74	283.48	73.14	56.1	273.8	330.7
X_2 p358.xls	Base 10	6.79	3.78	294.26	72.76	56.4	274.2	333.2
X_2 p381.xls	Base 11	6.67	3.73	312.04	72.97	55.9	273.5	336.0
X_2 p416.xls	Base 12	6.68	3.73	339.71	72.83	56.0	273.5	341.1
X_2 p062.xls	Mod. 1	5.62	3.10	76.96	72.87	53.2	270.6	285.9
X_2 p079.xls	Mod. 2	5.73	3.16	87.75	72.82	53.9	271.5	289.1
X_2 p085.xls	Mod. 3	5.78	3.19	93.22	72.48	54.1	271.8	290.5
X_2 p094.xls	Mod. 4	5.67	3.13	100.98	72.75	53.6	271.1	291.3
X_2 p128.xls	Mod. 5	5.80	3.20	126.37	72.36	54.3	271.9	297.1
X_2 p143.xls	Mod. 6	5.68	3.14	139.67	72.53	53.8	271.2	298.9
X_2 p179.xls	Mod. 7	5.76	3.18	166.43	72.86	54.3	271.7	304.7
X_2 p229.xls	Mod. 8	5.83	3.23	203.81	72.91	54.6	272.1	312.3
X_2 p274.xls	Mod. 9	5.79	3.22	233.66	72.93	54.5	271.9	317.9
X_2 p328.xls	Mod. 10	6.18	3.43	272.40	72.59	56.3	274.3	328.8

Table D.6 (cont.)

File Name	Trial #	$Q_{PH,loss}$ [W]	$Q_{CP,loss}$ [W]	$Q_{PH,adj}$ [W]	$Q_{CP,adj}$ [W]	$T_{sat2}(P_2)$ [°C]	h_1 [kJ/kg]	h_2 [kJ/kg]
X_2 p372.xls	Mod. 11	6.17	3.43	304.64	72.56	56.4	274.3	334.9
X_2 p424.xls	Mod. 12	6.23	3.48	343.39	72.81	56.5	274.5	342.9
File Name	Trial #	h_3 [kJ/kg]	X_2 [-/-]	X_3 [-/-]	q_{CP} [kW/m^2]	g_{CP} [kg/m^{2}s]	$T_{sat,avg}$ [°C]	$h_{overall}$ [kW/m^{2}K]
X_2 p105.xls	Base 1	310.4	0.105	0.204	21.5	289.2	55.4	11.77
X_2 p125.xls	Base 2	313.3	0.124	0.225	21.4	286.7	55.4	11.75
X_2 p152.xls	Base 3	317.8	0.154	0.255	21.6	285.9	55.5	11.74
X_2 p177.xls	Base 4	321.3	0.178	0.279	21.6	286.7	55.5	11.78
X_2 p195.xls	Base 5	323.8	0.195	0.297	21.7	285.0	55.5	11.80
X_2 p228.xls	Base 6	328.4	0.229	0.330	21.7	286.8	55.4	11.76
X_2 p274.xls	Base 7	335.0	0.275	0.376	21.8	288.5	55.4	11.54
X_2 p290.xls	Base 8	337.7	0.291	0.392	21.6	287.6	55.7	11.56
X_2 p343.xls	Base 9	345.4	0.343	0.445	21.8	287.8	55.7	11.55
X_2 p358.xls	Base 10	347.9	0.358	0.460	21.7	287.8	56.1	11.51
X_2 p381.xls	Base 11	350.6	0.381	0.482	21.7	288.4	55.6	11.37
X_2 p416.xls	Base 12	355.6	0.416	0.517	21.7	290.2	55.7	11.33
X_2 p062.xls	Mod. 1	300.4	0.063	0.161	21.7	291.2	52.8	11.41
X_2 p079.xls	Mod. 2	303.7	0.078	0.177	21.7	287.9	53.5	11.49
X_2 p085.xls	Mod. 3	305.0	0.084	0.183	21.6	289.1	53.7	11.44
X_2 p094.xls	Mod. 4	305.8	0.095	0.193	21.7	289.4	53.2	11.47
X_2 p128.xls	Mod. 5	311.6	0.128	0.227	21.5	289.6	53.9	11.55
X_2 p143.xls	Mod. 6	313.3	0.145	0.243	21.6	291.0	53.4	11.56
X_2 p179.xls	Mod. 7	319.1	0.180	0.278	21.7	292.1	53.9	11.66
X_2 p229.xls	Mod. 8	326.7	0.229	0.327	21.7	293.1	54.2	11.62

Table D.6 (cont.)

File Name	Trial #	h_3 [kJ/kg]	X_2 [-/-]	X_3 [-/-]	q_{CP} [kW/m^2]	g_{CP} [kg/m^{2}s]	$T_{sat,avg}$ [°C]	$h_{overall}$ [kW/m^{2}K]
X_2 p274.xls	Mod. 9	332.2	0.268	0.366	21.7	293.8	54.2	11.63
X_2 p328.xls	Mod. 10	343.3	0.328	0.429	21.6	289.0	56.0	11.64
X_2 p372.xls	Mod. 11	349.4	0.370	0.471	21.6	290.4	56.0	11.45
X_2 p424.xls	Mod. 12	357.4	0.424	0.525	21.7	289.9	56.2	11.35